



FACULTY OF SCIENCE AND TECHNOLOGY

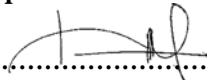
MASTER THESIS

Study programme / specialisation:
Engineering Structures and Materials /
Mechanical System

The spring semester, 2022

Author:
Izwan Bin Ahmad

Open / Confidential


.....
(signature author)

Course coordinator: AP Knut Erik Teigen Giljarhus

Supervisor(s): Prof. Muk Chen Ong
Anja Schnepf

Thesis title: Optimisation of Suspended Inter-array Power Cable
Configurations for Floating Offshore Wind Turbines

Credits (ECTS): 30

Keywords:

Suspended cable, inter-array cable, power
cable, floating offshore wind turbine,
OC3-Hywind, OrcaFlex

Pages: 106

+ appendix: 6

Stavanger, 08.07.2022
date/year

ABSTRACT

Floating offshore wind turbines (FOWTs) have been demonstrated to be highly promising for effectively harnessing energy from offshore wind in deeper water areas where installing bottom-fixed offshore wind turbines is not feasible. However, overcoming technological obstacles to commercialise floating offshore wind farms in deep water is still a work in progress, with inter-array cable designs being one of the most crucial areas to develop. Therefore, this study presents a novel configuration of suspended inter-array power cables using subsea buoys between two OC3-Hywind FOWTs supporting a 5MW turbine. In this configuration, the inter-array cable is kept afloat between the seabed and the sea surface by distributing several buoys along the cable. Each buoy is fitted with a bend stiffener on both ends. An optimisation methodology for this novel configuration is proposed, and the dynamic response of this configuration accounting for the effect of marine growth in 320 m range of water depth is investigated. The study of dynamic responses considers the impact on cable effective tension, minimum bend radius, and horizontal excursion. Configurations with copper cable and aluminium cable are investigated. Two differently sized buoys are used. Extreme environmental conditions of the Norwegian Sea and the rated operating environment based on the OC3-Hywind report are employed. The suspended inter-array power cable concept is proven to be feasible using the proposed buoy setup and optimisation methodology. The smaller buoys yield the most optimal designs for both cable types compared to the bigger buoys. Configurations using aluminium cables result in the lowest effective tension, but copper cables can withstand higher effective tension with a significantly larger safety margin to the minimum breaking load than the aluminium cable configuration. Copper cable configurations also result in a lower horizontal excursion than the aluminium cable configuration. The largest minimum bend radius occurs when the buoys are closely spaced.

ACKNOWLEDGMENTS

First and foremost, I would like to extend my utmost gratitude to my primary supervisor, Professor Muk Chen Ong, for his sincere guidance, encouragement, and insight. He propelled me to new heights and inspired me to excel in my study and career. He provided me with all the necessary tools to complete my thesis.

I would also like to thank my co-supervisor, Anja Schnepf, for her immense guidance and assistance in guiding me to build the global model in the OrcaFlex software. Her input on the standard practice in the industry is truly valuable, making my project more impactful.

Last but not least, I would like to thank my beloved wife, Nur Afiqah, who has always been supportive and resourceful with her input on the data science perspective of my studies. Without her by my side, this thesis will not be possible.

TABLE OF CONTENTS

ABSTRACT	ii
ACKNOWLEDGMENTS	iii
TABLE OF CONTENTS	iv
LIST OF FIGURES	vii
LIST OF TABLES	xi
1 INTRODUCTION	1
1.1 Background and Motivation.....	1
1.2 Problem Definition and Objectives.....	3
1.3 Structure of the Thesis.....	5
2 THEORY	6
2.1 Floating Offshore Wind Turbine Model.....	6
2.1.1 History of the Hywind concept.....	7
2.1.2 Description of the Spar Platform.....	9
2.1.3 Wind Turbine Mathematical Principles.....	10
2.1.4 Power Curve.....	14
2.1.5 Spacing Between Wind Turbines.....	15
2.2 Modelling in OrcaFlex.....	21
2.2.1 Coordinate Systems.....	21
2.2.2 Directions Conventions.....	22
2.2.3 Object Connections.....	22
2.2.4 Static Analysis.....	23
2.2.5 Dynamic Analysis.....	23
2.2.6 Hydrodynamic Loads.....	25
2.2.7 Lines.....	26
2.2.8 Turbines.....	28
2.2.9 Vessels.....	28
2.2.10 Constraints.....	28
2.2.11 6D buoys.....	29
2.3 Power Cables.....	30
2.3.1 Dynamic Power Cables.....	30

2.3.2	General Design.....	31
2.3.3	Conductor Materials.....	32
2.3.4	Dynamic Cable Configurations.....	33
2.3.5	Ancillary Equipment for Cables.....	36
2.4	Environmental Conditions	38
2.4.1	Current.....	38
2.4.2	Waves	40
2.4.3	Wind	44
2.5	Marine Growth	45
2.5.1	Increased Diameter and Weight	45
2.5.2	Change in Drag Coefficient	47
3	METHODOLOGY AND NUMERICAL SETUP.....	49
3.1	Environmental Conditions	49
3.1.1	Wind	51
3.1.2	Current.....	52
3.1.3	Waves	53
3.1.4	Load Implementation in Analysis	54
3.2	Modelling of the OC3-Hywind FOWT in OrcaFlex	55
3.2.1	Mooring Chains.....	57
3.2.2	Mooring Yaw Spring Stiffness	58
3.2.3	Spar	59
3.2.4	Nacelle.....	61
3.2.5	Turbine	61
3.3	Suspended Inter-Array Power Cable Configuration.....	63
3.3.1	Distance Between Wind Turbines in a Wind Farm	63
3.3.2	Dynamic Power Cable.....	64
3.3.3	Cable Ancillaries	65
3.3.4	Sensitivity Analysis.....	67
3.4	Effect of Marine Growth	68
3.5	Case Study Procedure	70
3.5.1	Case Study Variables.....	71
3.5.2	Acceptance Criteria.....	72

3.5.3	Dynamic Simulation Evaluation and Optimisation Method	73
4	RESULTS AND DISCUSSION	74
4.1	Steady-State Analysis	74
4.2	Dynamic Analysis	83
4.2.1	Preliminary Dynamic Analysis	83
4.2.2	Full Dynamic Analysis	88
5	CONCLUSIONS	98
6	RECOMMENDATIONS FOR FUTURE WORKS	101
	REFERENCES	102
	Appendix A	1
	Appendix B	1

LIST OF FIGURES

Figure 1.1: Offshore wind turbine structure (taken from [5]).	1
Figure 1.2: Area location of Utsira Nord and Sørilige Nordsjø II (taken from [6]).	2
Figure 1.3: Cable configuration. From left, (a) Free hanging catenary; (b) Lazy wave; (c) Fully suspended.	3
Figure 2.1: Illustrations of OC3-Hywind (reproduced from [10,11]).	6
Figure 2.2: Hywind Demo (left), and Hywind Scotland (right) (reproduced from [19]).	8
Figure 2.3: The spar-buoy floater of the OC3-Hywind FOWT.	9
Figure 2.4: Flow conditions and the extraction of mechanical energy from a free-stream airflow (taken from [22]).	11
Figure 2.5: Power coefficient vs flow velocity ratio before and after the turbine (taken from [22]).	12
Figure 2.6: Sectional view of an airfoil (taken from [23]).	12
Figure 2.7: Drag, lift, and resultant force on airfoil (taken from [23]).	13
Figure 2.8: NREL 5 MW Wind Turbine Power Curve for OC3-Hywind (reproduced from [11]).	14
Figure 2.9: The development of the wake shading area behind the rotor of a wind turbine (taken from [23]).	16
Figure 2.10: Jensen wake model control volume (taken from [31]).	17
Figure 2.11: Coordinate systems in OrcaFlex (taken from [37]).	21
Figure 2.12: Direction relative to the axes in OrcaFlex (reproduced from [37]).	22
Figure 2.13: Simulation Stages and Time in Dynamic Analysis (taken from [37]).	24
Figure 2.14: OrcaFlex line object (taken from [37]).	26
Figure 2.15: A typical analytic catenary solution for a two-dimensional grid (taken from [37]).	27
Figure 2.16: Subsea power cables for different applications (taken from [8]).	30
Figure 2.17: Typical cross-section of dynamic subsea cable (taken from [44]).	31
Figure 2.18: Inter-array laz wave cable configuration for Hywind Scotland (taken from [50]).	34
Figure 2.19: Effect of buoyancy distribution (red line) on the shape of a lazy wave dynamic cable (taken from [8]).	34
Figure 2.20: The buoy setup for a fully suspended configuration proposed by Schnepf et al. [9].	35

Figure 2.21: An exemplary bend stiffener (taken from [55]).	36
Figure 2.22: Buoy (left), and buoyancy module (right) (taken from [56]).	37
Figure 2.23: Horizontal submerged cross-section of a vertical cylinder (taken from [59]).	42
Figure 2.24: Wake amplification factor for smooth ($C_{DS}=0.65$ - solid line) and rough ($C_{DS}=1.05$ dotted line) (taken from [57]).	48
Figure 3.1: Location of the Hywind Tampen offshore wind farm in the Norwegian Sea (taken from [49]).	50
Figure 3.2: Wind Spectrum of the rated LC.	51
Figure 3.3: Wind spectrum of the extreme LC.	51
Figure 3.4: Current profile in extreme LC and rated LC.	52
Figure 3.5: Wave frequency spectrum for the rated LC.	53
Figure 3.6: Wave frequency spectrum for the extreme LC.	53
Figure 3.7: Plan view of the turbine mooring lines orientation and load angles.	54
Figure 3.8: Geometry of the OC3-Hywind FOWT (taken from [71]).	56
Figure 3.9: Delta connection (left) and location of “yaw_constraint” and “fixed_constraint” (right, red arrow) for mooring chains represented as an analytic catenary system.	58
Figure 3.10: “fixed_constraint” (left) and “yaw_constraint” (right) in the simulation software.	58
Figure 3.11: Variation in diameter at the tapered section (left) and the reference depth on the spar (right).	59
Figure 3.12: Added axial mass coefficient (left) and the location of the “damping_platform” object (right).	60
Figure 3.13: Properties of “damping_platform” (left) and the assigned additional linear damping (right).	60
Figure 3.14: Nacelle center of mass (CM).	61
Figure 3.15: Wing type and blade pitch controller.	62
Figure 3.16: Example of a suspended inter-array cable configuration.	63
Figure 3.17: Buoy B1 (left) and buoy B2 (right) with attached bend stiffeners.	65
Figure 3.18: Bend stiffener dimension details (m).	66
Figure 3.19: Stress-strain relationship of the bend stiffener.	66
Figure 3.20: Overview of the flow diagram in the analysis process.	70
Figure 3.21: Case naming convention.	71

Figure 4.1: Maximum effective tensions for aluminium cable configurations using 3 buoys of type B1 (left) and copper cable configurations with 5 buoy of type B1 (right) at 90° load angle in the SOL state.	78
Figure 4.2: MBR for aluminium cable configurations using 3 buoys of type B1 (left) and copper cable configurations with 5 buoys of type B1 (right) at 90° load angle in the SOL state.	78
Figure 4.3: Maximum horizontal excursions for aluminium cable configurations using 3 buoys of type B1 (left) and copper cable configurations with 5 buoys of type B1 (right) at 90° load angle in the SOL state.	78
Figure 4.4: Maximum effective tension for aluminium cable configurations using 4 buoys of type B2 (left) and copper cable configurations with 9 buoys of type B2 (right) at 90° load angle in the SOL state.	79
Figure 4.5: MBR for aluminium cable configurations using 4 buoys of type B2 (left) and copper cable configurations with 9 buoys of type B2 (right) at 90° load angle in the SOL state.	79
Figure 4.6: Maximum horizontal excursion for aluminium cable configurations using 4 buoys of type B2 (left) and copper cable configurations with 9 buoys of type B2 (right) at 90° load angle in the SOL state.	79
Figure 4.7: Horizontal excursion profile with varying spacings in steady-state under 90° load angle and viewed from the transverse direction for B2-CU-CL1200m-9B.	80
Figure 4.8: Horizontal excursion profile viewed from 0° for B2-CU-CL1200m-9B with varying spacings.	81
Figure 4.9: Location of highest effective tension for B1-AL-CL1200m-3B-S320m (left) and B1-AL-CL1400m-3B-S320m (right) at 90° load angle in the steady-state analysis.	82
Figure 4.10: Fitness Factor, Normalised MBL and Normalized MBR for aluminium cable configurations using buoy B1.	84
Figure 4.11: Fitness Factor, Normalised MBL and Normalized MBR for copper cable configurations using buoy B1.	85
Figure 4.12: Fitness Factor, Normalised MBL and Normalized MBR for aluminium cable configurations using buoy B2.	86
Figure 4.13: Fitness Factor, Normalised MBL and Normalized MBR for copper cable configurations using buoy B2.	87
Figure 4.14: Maximum effective tension profiles for configuration A in the rated LC.	90

Figure 4.15: Maximum effective tension profiles for configuration A in the extreme LC.	91
Figure 4.16: Maximum effective tension profiles for configuration B in the rated LC.....	91
Figure 4.17: Maximum effective tension profiles for configuration B in the extreme LC.....	92
Figure 4.18: Maximum effective tension profiles for configuration C in the rated LC.....	92
Figure 4.19: Maximum effective tension profiles for configuration C in the rated LC.....	93
Figure 4.20: Cable shapes of the selected configurations from each category viewed from the transverse direction (0° angle) in steady-state.....	96
Figure 4.21: Horizontal excursion profile in rated LC and extreme LC from 0° load angle measured in the positive direction of the global x-axis.....	96

LIST OF TABLES

Table 2.1: Comparison of copper and aluminium conductor material properties.....	32
Table 2.2: Thickness and density of marine growth and biofouling.....	46
Table 3.1: Summary of the environmental loading conditions.....	50
Table 3.2: Summary of the load directions.....	54
Table 3.3: Floating platform structural properties [10].....	55
Table 3.5: Mooring system properties [10].....	57
Table 3.4: Floating platform hydrodynamic properties [10].....	60
Table 3.6: Properties of NREL 5-MW baseline wind turbine [11].....	62
Table 3.7: Properties of the copper cable and the aluminium cable.....	64
Table 3.8: Properties of buoys without cable insertion.....	65
Table 3.9: Depth range and calculation parameters for marine growth effect.....	68
Table 3.10: EOL properties of the aluminium cable.....	69
Table 3.11: EOL properties of the copper cable.....	69
Table 3.12: Cable configuration variables tested for buoy B1.....	71
Table 3.13: Cable configuration variables tested for buoy B2.....	71
Table 3.14: Acceptance criteria for steady-state and dynamic analysis of the cable configuration.	72
Table 4.1: Steady-state analysis summary for aluminium cable configurations with buoy B1.	75
Table 4.2: Steady-state analysis summary for aluminium cable configurations with buoy B2.	75
Table 4.3: Steady-state analysis summary for copper cable configurations with buoy B1.....	76
Table 4.4: Steady-state analysis summary for copper cable on buoy B2.....	76
Table 4.5: Preliminary dynamic analysis results.....	84
Table 4.6: Best cable configuration cases selected with the Fitness Factor.....	88
Table 4.7: Cable effective tensions obtained from dynamic analysis.....	89
Table 4.8: MBRs for all configurations obtained from dynamic analysis.....	94
Table 4.9: Comparison of maximum horizontal excursion in all configurations.....	95

1 INTRODUCTION

This chapter provides the thesis's context on offshore wind technologies, the motivation for this thesis, objectives, and outline of the work.

1.1 Background and Motivation

To abide by the 2015 Paris Climate Accords of the United Nations Framework Convention on Climate Change [1], the race to develop more profitable and robust renewable energy solutions has become more crucial than ever, particularly in the wind energy sector. This is due to the zero greenhouse gas emissions and ease of maintenance of a wind farm power plant [2]. The abundance of sites, higher wind energy producibility, and potentially lesser environmental impact than other renewable energy solutions make offshore wind power generation attractive [3]. As shown in Figure 1.1, offshore wind turbine structures can generally be classified into bottom-fixed and floating. Bottom-fixed offshore wind turbines are more developed and standardised at the time of writing, but the applications are limited to shallow water depths. Since the installation of bottom-fixed offshore wind turbines is not practical, FOWTs have been demonstrated to be more feasible for effectively capturing and harnessing offshore wind energy in deeper water areas where better wind resources are available [4].

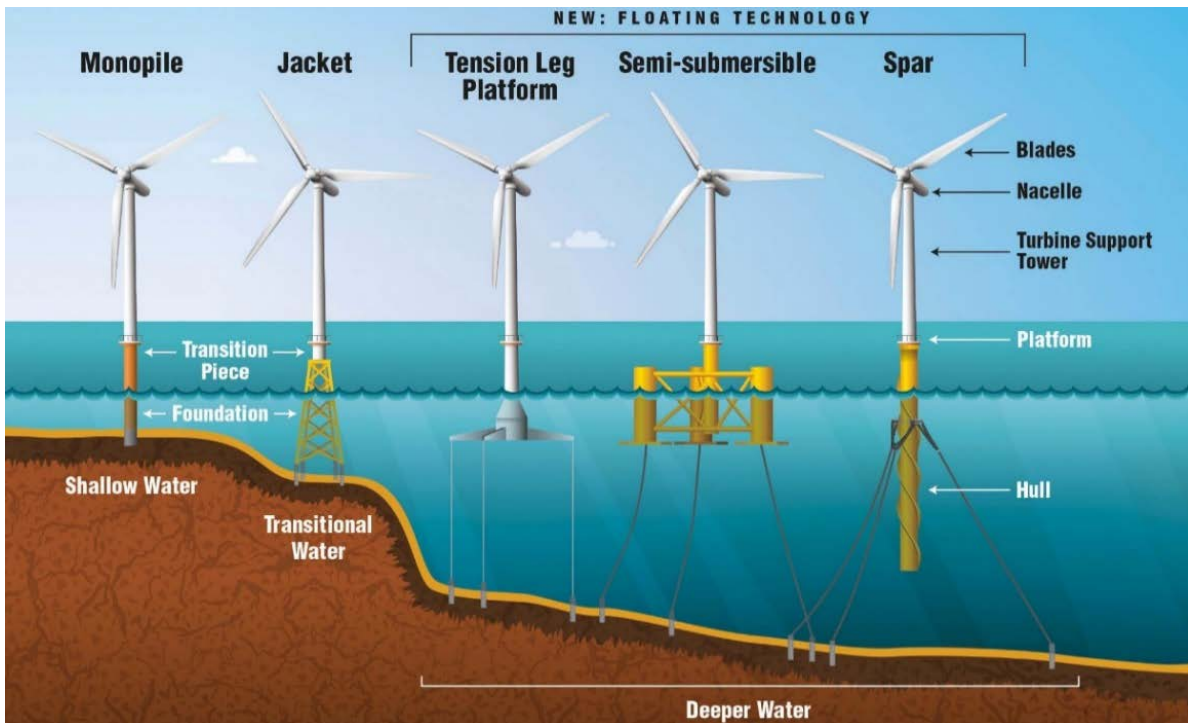


Figure 1.1: *Offshore wind turbine structure (taken from [5]).*

In 2020, The Norwegian Ministry of Petroleum and Energy has decided to reserve two areas for offshore wind power, "Utsira Nord" and "Sørlige Nordsjø II" [6]. These areas are depicted in Figure 1.2. Utsira Nord is an area covering 1010 km² with an average water depth of 267 m. It is located to the west of Haugesund in Norway and is suited for floating wind power with an expected capacity between 500 MW and 1500 MW. That is approximately 16 to 50 times the capacity of the Hywind Scotland wind farm, which was already a success in a first-of-its-kind operation due to its high ratio of actual energy output versus maximum possible output [4]. Therefore, overcoming the technological obstacles to commercialise floating offshore wind farms in deeper water is proven to be an important feat.



Figure 1.2: Area location of Utsira Nord and Sørlige Nordsjø II (taken from [6]).

1.2 Problem Definition and Objectives

An offshore wind farm consists of several turbines connected via power cables to form a feeder to the hub. Then the electricity is exported to consumers by a single export cable. Inter-array cabling is the term used to describe the cable connection between turbines in a single feeder. Wind farms based on FOWTs are currently less economical than fixed-bottom wind turbines, and inter-array power cable configuration is one of the main contributing factors. Inter-array cabling accounts for roughly 30% of the capital expenses for offshore wind projects [7]. Two common concepts of inter-array power cable configurations are the free-hanging catenary and the lazy wave configuration [8], as shown in Figure 1.3 (a) and Figure 1.3 (b). The catenary and the lazy wave configurations become less practical in deeper water depths. A long cable requirement for an installation in deep water causes a loss of electricity due to long transmission distances. A long cable also causes an increase in cable effective tensions due to the unsupported hanging cable weight. The novel design of the suspended inter-array power cable configuration in Figure 1.3 (c) is expected to have less dependency on water depth and shorter transmission distance. However, this configuration has no contact with the seabed and is expected to cause a high horizontal excursion of the cable in response to loading from currents. Additionally, the cable is expected to experience extreme bending at the point of suspension. Therefore, the design of the fully suspended inter-array power cable configurations must be investigated and optimised by considering the impact on cable effective tension, minimum bend radius, and horizontal excursion.

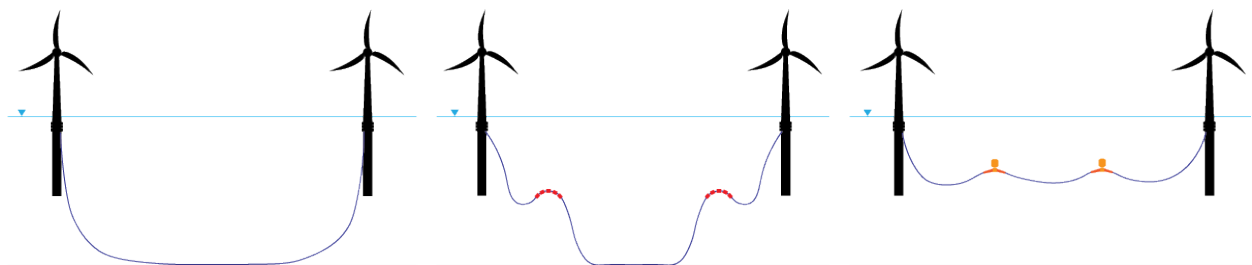


Figure 1.3: Cable configuration. From left, (a) Free hanging catenary; (b) Lazy wave; (c) Fully suspended.

On the other hand, marine growth is an indispensable factor for dynamic inter-array power cable configurations. Marine growth is created by plants and animal colonies growing on the cable surface. It is a typical term for surface colonisation on marine structures, such as corals, hydroids, bivalves, molluscs, seaweed, and anemones. It is strongly reliant on geographical zones. When marine growth is present, the added weight and effective diameter of the cable impact the configuration behaviour. Vortex shedding on the cable when the marine growth are present may

also result in a greater hydrodynamic action and increased hydrodynamic additional mass compared to the cable without the marine growth. Therefore, the effect of marine growth presence on the inter-array power cable configurations in a dynamic application must be investigated.

The choice of the conductor core material determines the dynamic response of the cable due to the difference in weight, stiffness, and cross-sectional area for electrical conductivity. Two commonly used cable conductor core materials are copper and aluminium. For the same voltage rating, the copper cable conductor core tends to have a smaller cross-sectional area than the aluminium counterpart. This is due to its high conductivity compared to the conductivity of an aluminium conductor. The difference in cross-sectional area of the conductor core also leads to the difference in submerged weight to diameter ratio and overall cable diameter. Copper cables also have a higher weight per unit length than aluminium cables. The difference in weight between these two conductor core materials may affect the effective tension in the resulting cable configuration. Therefore, the pros and cons of each cable type for the application of dynamic fully suspended inter-array power cable configurations must be investigated.

In order to reduce the tension at the hang-off point (HOP) and decouple the motion between the FOWT and the cable section laying on the seabed, the lazy wave configuration uses multiple buoyancy modules as the floater between the HOP and the touchdown point. To achieve the same goal in a fully suspended inter-array power cable configuration, Schnepf et al. [9] investigated the feasibility of a much bigger buoy as the cable floater instead of the smaller buoyancy module. According to Schnepf, larger tensions are observed in the configuration with the buoyancy modules compared to the configuration with the buoys. However, there is still insufficient study varying the buoy size for a fully suspended inter-array power cable configuration.

In conclusion, this study proposes an optimisation methodology and investigates the dynamic response of a fully suspended inter-array power cable configuration in a novel buoy setup. The dynamic response of the cable will be studied by considering the effect of marine growth and its impact on effective tension, minimum bend radius (MBR), and the horizontal excursion of the cable. In addition, the suitability of a copper cable or an aluminium cable, and the choice of buoy sizing for this suspended cable configuration are studied. The feasibility of the suspended inter-array power cable concept will be determined.

1.3 Structure of the Thesis

The content of the thesis is organised as follows:

- **CHAPTER 1 - INTRODUCTION:**

This chapter discusses the thesis's context and author's motivation, as well as the scope, objectives, and outline of the work.

- **CHAPTER 2 - THEORY:**

This chapter elaborates on the thesis's fundamental theory on the wind turbine used, the power cable, the environmental conditions, and the marine growth.

- **CHAPTER 3 - METHODOLOGY AND NUMERICAL SETUP:**

In this chapter, the research methodology is described. The environmental loading conditions are explained, followed by the modelling of the wind turbine and the cable configuration setup. Then, the effect of marine growth on the cable properties is then described, and the case study procedure is explained.

- **CHAPTER 4 - RESULTS AND DISCUSSION:**

The results of the steady-state analysis are discussed in this section, followed by explanations of the dynamic analysis results.

- **Chapter 5 – RESULTS AND DISCUSSION:**

This chapter contains a summary of the thesis. The major conclusions and the feasibility of the proposed suspended cable concepts are discussed in this section.

- **Chapter 6 - RECOMMENDATIONS FOR FUTURE WORKS:**

Recommendations for future studies related to this thesis are presented in the closing chapter.

2 THEORY

Fundamental knowledge of the system is essential to comprehend the challenge and the process of analysing the dynamic response of fully suspended inter-array power cables in wind farms. This chapter discusses wind turbine theory in general, modelling in OrcaFlex, as well as FOWTs and subsea power cable connections. Additionally, this chapter provides the historical context of the Hywind wind turbine concept and other pertinent theories.

2.1 Floating Offshore Wind Turbine Model

Numerous floating platform concepts are available such as spar buoys, tension leg platforms (TLPs), barges, and hybrid concepts. For this study, the focus will be on a spar-buoy type FOWT concept named “Hywind” developed by Equinor (formerly known as Statoil). It is an innovation that incorporates well-known floating spar technologies from the offshore and wind energy industries. The hywind concept is shown in Figure 2.1. Hywind is a floating wind turbine concept based on a single floating cylindrical spar buoy platform anchored to the seabed by three mooring chains. The spar substructure is ballasted, allowing the entire structure to float vertically. Onboard control software actively monitors the wind turbine's performance and regulates the pitch of the blades to dampen the tower's motion and maximise energy production. This FOWT supporting the 5 MW baseline turbine has been modelled and studied by Jonkman et al. [10,11] of the National Renewable Energy Laboratory (NREL) in the Offshore Code Comparison Collaboration (OC3). The wind turbine model is called OC3-Hywind in this study.

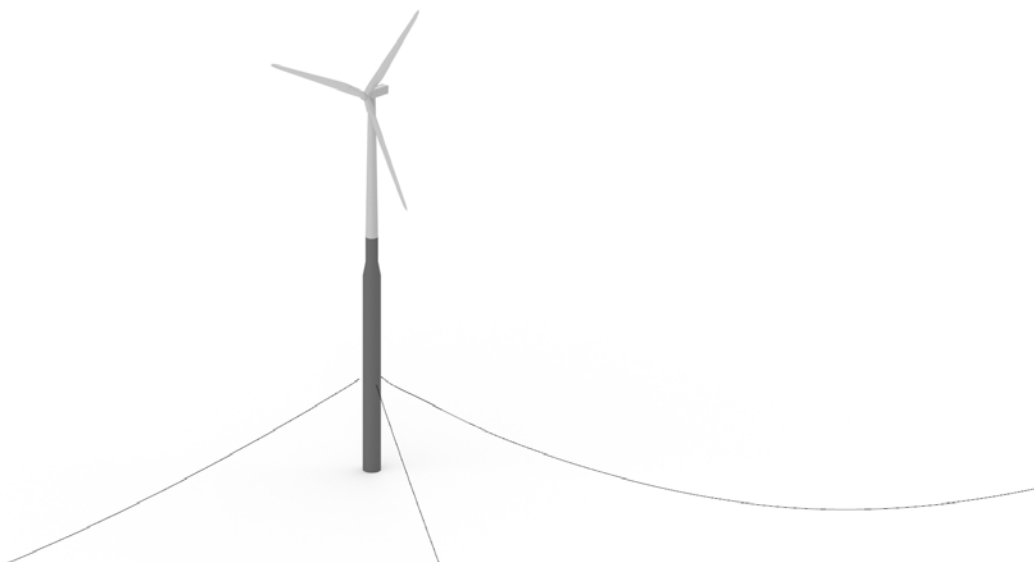


Figure 2.1: Illustrations of OC3-Hywind (reproduced from [10,11]).

2.1.1 History of the Hywind concept

The Hywind patent-protected concept [12] was initially developed in 2001 at Norsk Hydro by Dagfinn Sveen. When Equinor acquired Norsk Hydro's oil sector in 2008, Hywind was transferred to Equinor [13]. The first pilot wind turbine of the Hywind concept called Hywind Demo was installed and put into operation 10 km southwest of Karmøy in Norway in June 2009 by Equinor [14]. The single-turbine with a power of 2.3 MW was installed to test the use of ballast-stabilised floating foundations and anchored to the seabed with mooring chains. It became the world's first floating wind turbine in the megawatt class [15] and has been extensively studied since its commencement. Ten years later in 2019, Unitech Offshore took over the ownership of Hywind Demo. The turbine was made available for research and technology development as a part of the Sustainable Energy Katapult. It was then renamed to Unitech Zephyros [16]. The turbine is also used as a part of the infrastructure at the METCentre test site. One of the studies was done by Skaare et al. [17] to evaluate the behaviour comparing calculations performed by several simulation software. Skaare found that the statistical differences between simulated and measured wind turbine parameters are relatively large, but the uncertainties of the results are within acceptable limits.

After 8 years of testing a full-scale Hywind prototype offshore Karmøy in Norway, Hywind Demo has proven to function well in all wave and wind conditions. The successful demonstration project paved the way for the world's first commercial floating wind farm, which is Hywind Scotland. Equinor, in collaboration with Masdar of Abu Dhabi, opened the Hywind Scotland Pilot Park in October 2017 off the coast of Aberdeenshire in Scotland, with a capacity of 30 MW [18]. Hywind Scotland consists of five 6 MW wind turbines anchored to the seabed in water depths of up to 120 m. Figure 2.2 shows the side-by-side comparison of Hywind Demo and Hywind Scotland. Hywind Scotland has achieved the highest average capacity factor of any UK wind farm since its operation began [4]. This ratio of actual energy output versus maximum possible output has averaged 57.1% at Hywind Scotland compared to around 40% for other offshore wind projects around the country, which are all fixed-bottom wind turbines.



Figure 2.2: *Hywind Demo (left), and Hywind Scotland (right) (reproduced from [19]).*

Following the success of Hywind Scotland, Equinor is expected to start the operation of a new wind farm, Hywind Tampen, in 2022. Hywind Tampen will consist of 11 FOWTs in a farm configuration with a total capacity of 88 MW. It is intended to provide electricity for the Snorre and Gullfaks offshore field operations in the Norwegian Sea [20]. It will be the world's first floating wind farm to power offshore oil and gas platforms. It is located approximately 140 km off the Norwegian coast at water depths between 260 m and 300 m. With proven reliability and success, more future wind park projects will be expected to utilize Hywind FOWT in the Norway offshore wind industry. Therefore, the OC3-Hywind floating offshore wind turbine based on Hywind is a great FOWT model to be used for the present study.

2.1.2 Description of the Spar Platform

A spar-buoy type platform is a ballasted cylindrical monohull substructure with a centre of gravity (COG) substantially lower than its centre of buoyancy. The spar-buoy type, also known as a deep-draft floater, relies on its COG far below its centre of buoyancy to gain static stability. The monohull substructure is made up of three sections. Above the sea water level (SWL), the top section of the spar-buoy platform attaches to the tower foundation. The top section is a cylinder with the same diameter as the tower base. The bottom section connects the spar to the mooring chains, and the middle section is a linearly tapering cone connecting the top and bottom sections of different sizes. Figure 2.3 (left) shows the OC3-Hywind floater sections, and Figure 2.3 (right) shows the spar buoy object in the simulation software.

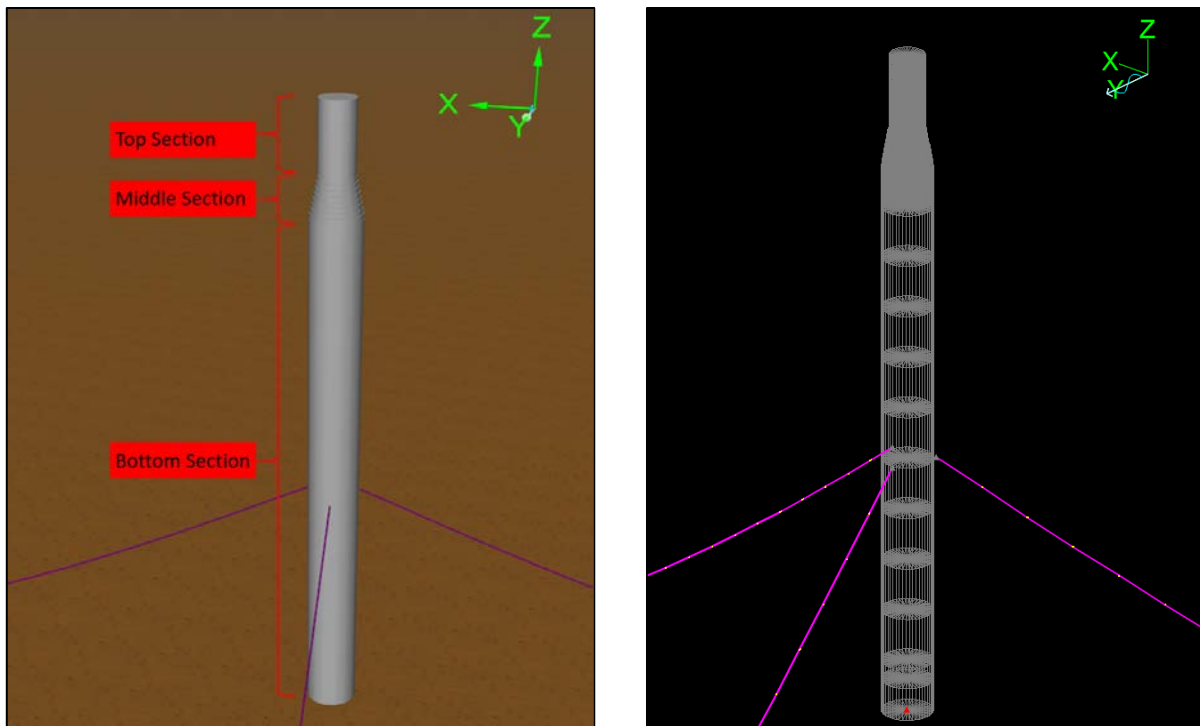


Figure 2.3: *The spar-buoy floater of the OC3-Hywind FOWT.*

2.1.3 Wind Turbine Mathematical Principles

The general concept of every wind turbine is to convert kinetic energy from the wind into mechanical energy. The mechanical energy will then be used to generate electrical energy by rotation of the rotor shaft of a generator. According to Hau [21], Albert Betz was the first person to implement one-dimensional momentum theory of a disk-shaped rotating wind energy converter in windmills. Using this theory, Betz found the maximum limit of energy that can be extracted from the wind. The theory contains simplifications such as assumed frictionless flow. It has been demonstrated to be somewhat useful in the early stages of calculation for practical engineering. The following theory in this section was originally developed by Betz and later reproduced by Hau [21].

Albert Betz Momentum Theory

Kinetic energy is given by:

$$E = \frac{1}{2}mv^2 \quad (Nm) \quad (2.1)$$

Where v is the airflow velocity (m/s) with a mass of m (kg) for a wind converter. The volumetric flow rate, \dot{V} is:

$$\dot{V} = vA \quad (m^3/s) \quad (2.2)$$

Where A is the area (m^2). The flowrate of mass \dot{m} is expressed as:

$$\dot{m} = \rho_{air}vA \quad (kg/s) \quad (2.3)$$

Where the density of air is ρ_{air} (kg/m^3). The amount of energy, P (Watts) that passes through the cross-section area per unit time is:

$$P = \frac{1}{2}\rho_{air}v^3A \quad (W) \quad (2.4)$$

The kinetic energy in the airflow reduces when converted to mechanical energy. When the velocity is reduced, the cross-sectional area is expanded. This is shown in Figure 2.4. Here, V_1 and A_1 refer to the flow velocity and area before the energy extraction, and V_2 and A_2 refer to the flow velocity and area after the extraction.

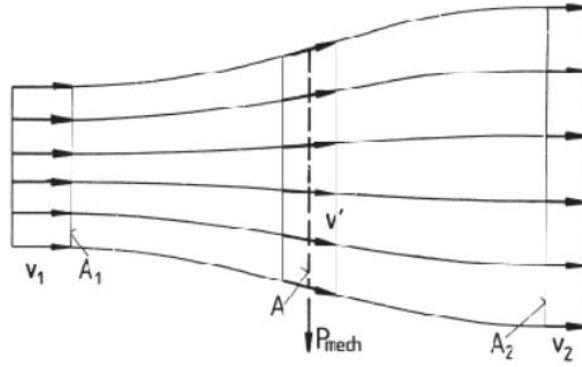


Figure 2.4: Flow conditions and the extraction of mechanical energy from a free-stream airflow (taken from [22]).

The energy extraction occurs as a result of the difference in power before and after the extraction:

$$P = \frac{1}{2} \rho_{air} v_1^3 A_1 - \frac{1}{2} \rho_{air} v_2^3 A_2 = \frac{1}{2} \rho_{air} (v_1^3 A_1 - v_2^3 A_2) \quad (W) \quad (2.5)$$

According to Equation (2.5), the highest energy extraction is achieved if $v_2 = 0$. However, this does not make physical sense because it implies that $v_1 = 0$ as well, indicating that there is no energy extraction. Betz derived a theory of the optimal relationship between the flow velocity before and after extraction, $\frac{v_1}{v_2}$, using conservation of momentum equation. c_p was introduced to have a reference for the power output, where the power output, P , is compared to the power of a free-flowing flow without extraction, P_0 .

$$c_p = \frac{P}{P_0} \quad (2.6)$$

According to Figure 2.5, the maximum power to be obtained is at c_p around 0.6, precisely at:

$$c_p = \frac{16}{27} = 0.593 \quad (2.7)$$

This is frequently referred to as the Betz factor, expressing the maximum theoretical efficiency.

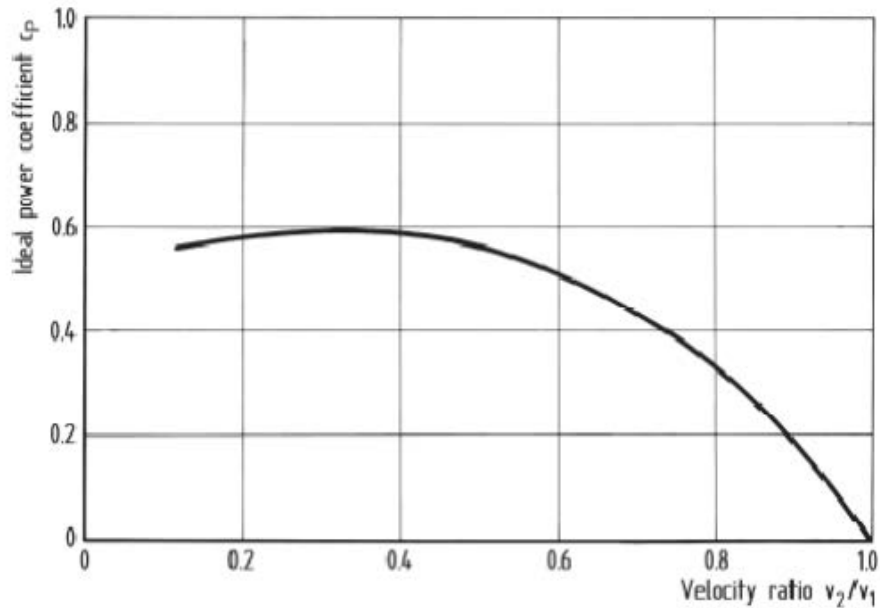


Figure 2.5: Power coefficient vs flow velocity ratio before and after the turbine (taken from [22]).

Airfoil Theory

The blades are one of the most important components in a wind turbine system. They are foil-shaped and responsible for transferring kinetic energy from the wind to the rotor's mechanical energy. Wind turbine foils were originally derived from aviation foils [23]. Nowadays, there is a whole industry dedicated to wind turbine foil optimisation and design. Figure 2.6 depicts a basic representation of the fundamental elements of a conventional airfoil.

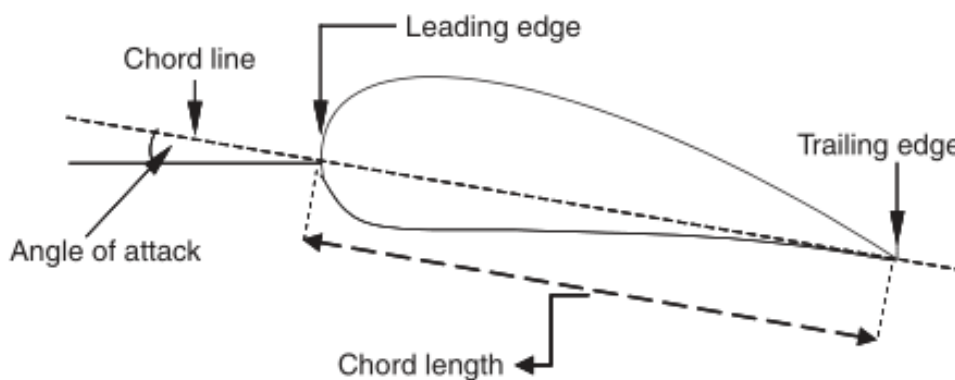


Figure 2.6: Sectional view of an airfoil (taken from [23]).

The foil undergoes a separation of streamlines above and below it when placed in a flowing stream. Due to the curvature, the streamlines above the foil have a longer path to travel than the streamlines

below the foil. As a result, the flow velocity on the upper side will increase in order to meet the particles in the streamlines on the bottom of the foil at the trailing edge. According to Bernoulli's principle, an increase in velocity must be balanced by a decrease in pressure. A pressure difference between the upper and bottom sides of the foil is created by reduced pressure due to velocity increase, resulting in a lift force directed upwards. A drag force is also exerted to the foil at the same time. Both lift and drag force produced the net resultant force on the air foil, as seen in Figure 2.7.

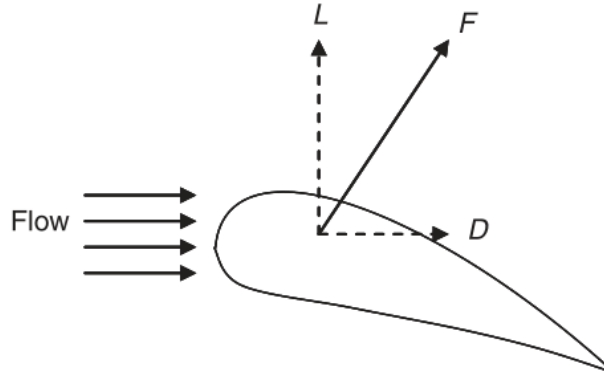


Figure 2.7: Drag, lift, and resultant force on airfoil (taken from [23]).

The drag, D , and lift, L , force can be expressed as:

$$D = C_D \frac{1}{2} \rho_{air} v^2 A \quad (N) \quad (2.8)$$

$$L = C_L \frac{1}{2} \rho_{air} v^2 A \quad (N) \quad (2.9)$$

Where C_L and C_D are lift coefficient and drag coefficient respectively. The angle of attack influences the lift and drag forces. In the case of wind turbine airfoils, drag is merely a parasitic component of the lift force. As a result, with a given flow, it is better to position the blades at an angle that maximises the C_L/C_D ratio. The rotation of the foil causes the tangential velocity of a wind turbine. The velocity that a point experiences is the product of its velocity and its tangential velocity. The lift is always perpendicular to the drag, and the drag force is parallel with the resulting velocity.

2.1.4 Power Curve

The power curve of a wind turbine is divided into four operating stages, each of which has a different method of turbine control. The division is based on the incoming wind speed; cut-in wind speed, rated wind speed, and cut-out wind speed. Cut-in wind speed is the lowest wind speed at which the turbine begins to generate electricity. Rated wind speed is the wind speed at which the turbine's maximum power rating is calculated. Cut-out wind speed refers to the wind speed that, if surpassed, will cause the turbine to shut down since the high wind speed may damage the turbine. Figure 2.8 shows the wind turbine power curve for the 5 MW turbine from OC3-Hywind. Region 1 is a region with wind speed that is less than cut-in wind speed where no power is produced. In this region, the wind speed is insufficient to create electricity. The area between cut-in and rated wind speed is known as Region 2. To capture a maximum lift from wind speed in this range, the pitch angle is adjusted at a specific angle. The area between the rated and cut-out wind speeds is referred to as Region 3. Since the wind speed in this region is higher than the rated wind speed, the generator torque is kept constant to maintain consistent production and reduce the rotor load by varying the pitch angle. When the wind speed is too high and surpasses the cut-out wind speed, the wind speed is classified as Region 4. If the turbine operates beyond the cut-out wind speed, it will be exposed to excessive loading. Therefore, the turbine is set to park or in feathered mode to reduce rotor load and avoid damage.

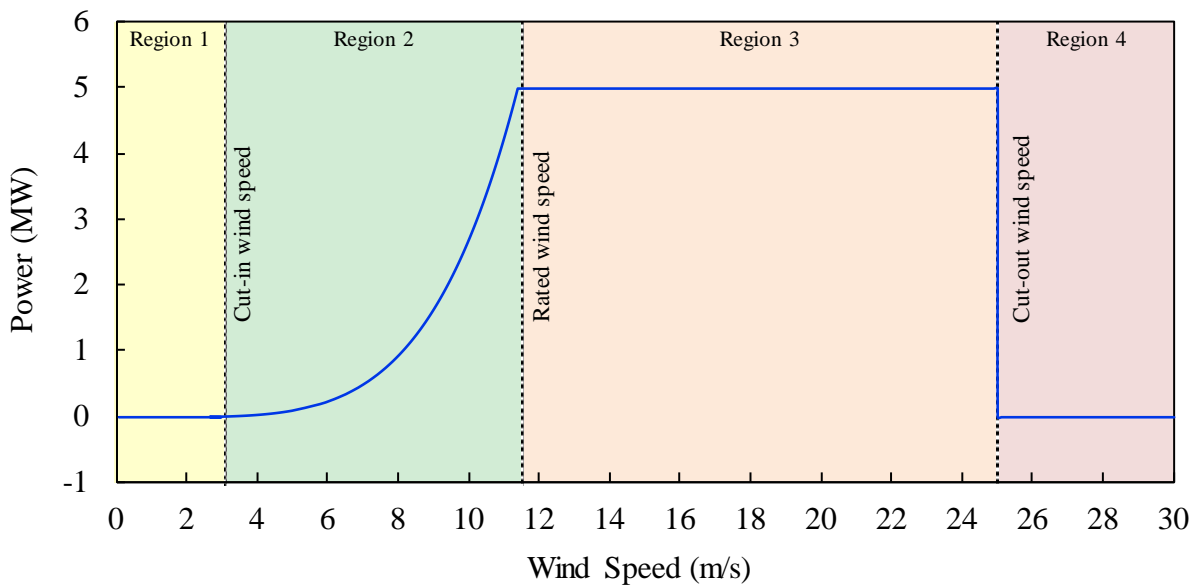


Figure 2.8: NREL 5 MW Wind Turbine Power Curve for OC3-Hywind (reproduced from [11]).

2.1.5 Spacing Between Wind Turbines

When designing a wind farm, it is desirable to have a wind farm as compact as possible and simultaneously able to maximise the power output generated from the wind. The term compact in this context refers to the wind turbines being close together. A compact wind farm can be achieved by reducing the turbine spacing. Thus reducing the cable length, which also lowers the power loss by transmission. However, these two goals contradict one another as the closely positioned floating wind turbines will increase the possibility of mooring chains clashing and wake effects.

Generally, mooring lines and power cables should not cross one another in plan view. Therefore, the radius and orientation of the mooring lines have to be considered when deciding the wind turbine spacing. During operation, the power cables and mooring chains are expected to move and respond to the environmental load and movement of the connected FOWT. In the case of cables or mooring chains breakage, it is crucial to ensure that the broken structure will not cause further damage to other structures as it falls to the seabed. Therefore, the mooring chains of the FOWT, the mooring chains of the neighbouring FOWT, and the inter-array cables between the two FOWTs must not intersect in planar view.

Wake is one of the most important considerations when designing a wind farm. The wake effect caused by the upstream wind turbine will reduce the power output and increase the loading on the downstream wind turbines. This is due to the reduced wind speed and turbulences in the wind behind the upstream wind turbine. To optimise the power production of a wind farm by reducing the wake-induced power losses, it is suggested that the turbines should be spaced between 5 to 9 rotor diameters (D) in the prevailing wind direction and between $3D$ to $5D$ in the perpendicular direction to the prevailing wind [24]. Downwind spacing of more than $7D$ with cross-wind spacing of at least $4D$ is required to limit downstream inter-turbine wake-induced power loss to less than 20% [25,26]. In the wake, there are two major physical phenomena of interest: (1) a momentum (or velocity) deficit, which reduces downstream turbine power output, and (2) an increased level of turbulence, which creates unsteady loading on downstream turbines. Figure 2.9 illustrates the development of the shading area and the recovery of the wind kinetic energy behind the upstream turbine.

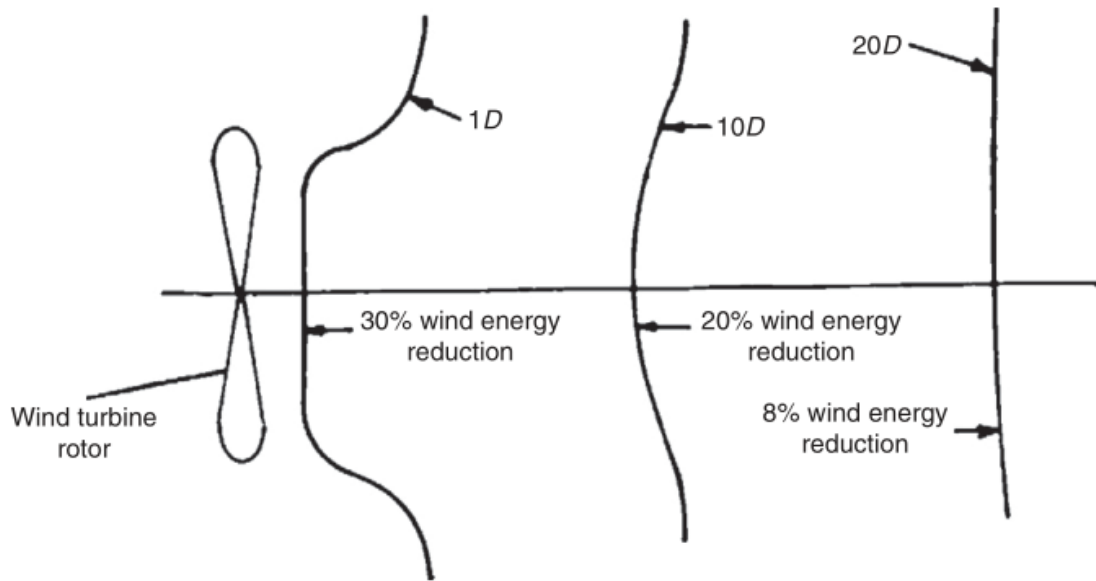


Figure 2.9: *The development of the wake shading area behind the rotor of a wind turbine (taken from [23]).*

Near and far wakes are two zones within the wake that are evaluated for wake-induced power losses and blade loadings. The near wake begins immediately after the turbine and extends from $2D$ to $4D$ [27,28]. The rotor geometry strongly influences the flow in this region, resulting in the formation of blade tip vortices. There are also steep pressure, axial velocity, and wake expansion gradients in this region. Reduced wind speeds and increased turbulence intensities are the only effects of the rotor shape in the far wake. Furthermore, in the far wake, turbulence is the dominant physical feature [29]. In addition to rotor-induced turbulence, large-scale or atmospheric turbulence affects the region further downstream. The turbulence mixing accelerates the wake recovery in terms of turbulence intensity and velocity deficit. The velocity deficit approaches a Gaussian profile in the far wake, which is axisymmetric and self-similar [30]. Although it considerably increases the unsteady loading on the downstream turbine, the meandering of the wake may aid in the recovery of the velocity deficit. All of these factors influence the development of wind turbine wake models in distinct ways. The Jensen, Larsen, and Fuga wake models are among the numerous that produce good results for offshore implementations [31].

Jensen Wake Model

For its simplicity, practicality, and robustness, the Jensen wake model is one of the most popular models in engineering applications. The description of Jensen wake model is based on the research by Jensen [32] and Katic et al. [33].

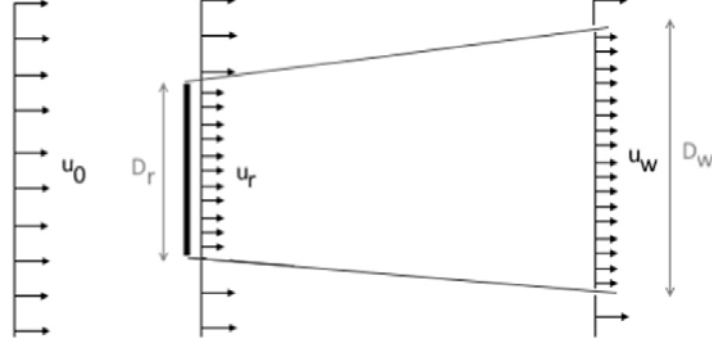


Figure 2.10: Jensen wake model control volume (taken from [31]).

Using the control volume shown in Figure 2.10, where $D = D_r$ is the rotor diameter, and assuming a top-hat inflow profile, the mass balance between the downstream flow and the rotor plane produces:

$$\left(\frac{D_r}{2}\right)^2 u_r + \left[\left(\frac{D_w}{2}\right)^2 - \left(\frac{D_r}{2}\right)^2\right] u_0 = \left(\frac{D_w}{2}\right)^2 u_w \quad (2.10)$$

The wake is also assumed to be expanded linearly as a function of the downstream distance x at a rate α , $D = D_r + 2\alpha x$ and $\frac{u_r}{u_0} = 1 - 2a$ using the axial induction factor, the fractional decrease in wind speed, $a = \frac{u_0 - u_r}{u_0}$. Putting it into Equation (2.10), the normalised velocity can be found as:

$$\frac{u_w}{u_0} = 1 - \frac{2a}{\left(1 + \frac{2\alpha x}{D_r}\right)^2} \quad (2.11)$$

Assuming ideal axisymmetric flow with no turbulence, no rotation, and a conic shape wake profile, the axial induction factor a can also be written as:

$$a = \frac{1 - \sqrt{1 - C_T}}{2} \quad (2.12)$$

Larsen Wake Model

Larsen [34] has introduced a simple wake calculation procedure which was implemented in the commercial software windPRO [35]. The axisymmetric form of the RANS equations with the thin shear layer approximation is used in the model. The pressure term appearing in the parabolic equations was neglected, and the turbulence closure, ν_T , was represented using Prandtl's mixing length theory as:

$$\nu_T = l^2 \sqrt{S_{ij}} \quad (2.13)$$

Where,

$$\begin{aligned} l &= \text{Mixing length} \\ S_{ij} &= \text{Strain rate tensor} \end{aligned}$$

The problem is assumed to be axisymmetric, steady, and self-similar along the perpendicular direction to the flow. Larsen considered the solution of the RANS equations using first and second-order approximations. In the first-order approximation, the expression to be solved together with continuity equation is simplified as:

$$U_\infty \frac{\partial u_x}{\partial x} = \frac{1}{r} \frac{\partial}{\partial r} \left[l^2 r \left(\frac{\partial u_x}{\partial r} \right)^2 \right] \quad (2.14)$$

Where,

$$\begin{aligned} u_x &= \text{Wake perturbation of the inflow along the axial direction} \\ r &= \text{Radial direction} \\ x &= \text{Axis of symmetry.} \end{aligned}$$

To solve Equation (2.14), two boundary conditions are defined:

1. $u_x = 0$ on the wake boundary, and
2. $U_\infty \gg u_x$ is obtained by solving the momentum balance with the assumption of higher inflow velocity than the axial wake perturbations.

Using those conditions, the wake radius (r_w), axial (u_x) and radial (u_r) wake perturbations are found as:

$$r_w(x, r) = \left(\frac{35}{2\pi}\right)^{0.2} (3c_1^2)^{0.2} (C_T Ax)^{\frac{1}{3}} \quad (2.15)$$

$$u_x(x, r) = -\frac{U_\infty}{9} (C_T Ax^{-2})^{\frac{1}{3}} \left[r^{1.5} (3c_1^2 C_T Ax)^{-0.5} - \left(\frac{35}{2\pi}\right)^{0.3} (3c_1^2)^{-0.2} \right]^2 \quad (2.16)$$

$$u_r(x, r) = -\frac{U_\infty}{3} (C_T A)^{\frac{1}{3}} x^{-\frac{5}{3}} r \left[r^{1.5} (3c_1^2 C_T Ax)^{-0.5} - \left(\frac{35}{2\pi}\right)^{0.3} (3c_1^2)^{-0.2} \right]^2 \quad (2.17)$$

Where

C_T = Thrust coefficient

A = Rotor swept area

c_1 = Constant that is defined empirically according to [34]

According to Larsen, the second-order system uses the full form of the RANS equations, which are negligible for most engineering applications.

Fuga Wake Model

Fuga is a convenient engineering tool based on the linearised RANS equations. It uses a look-up tables system to construct the velocity field behind a turbine, and it uses linear summation to consider multiple wake cases. Due to its simplicity in wake modelling, Fuga is one of the most robust computational fluid dynamics (CFD) based models established for wake effects calculations. The Cartesian form of the RANS equations is used with a simple closure, where the eddy viscosity is equal to that usually used within the atmospheric surface layer.

$$v_T = \kappa u_* z \quad (2.18)$$

Since the equations are not parabolized, there is no need to induce the artificial rotor velocity where the atmospheric inflow is modelled using the logarithmic wind profile counting the stability effects. The drag force term is modelled using an actuator disk model with a layered control volume as:

$$\bar{f}_i = f_x = -\frac{1}{2} C_T U_{free}^2 \delta(x - x_h) \Theta[R^2 - (y - y_h)^2 - (z - z_h)^2] \quad (2.19)$$

where δ is the Dirac delta function and Θ is a step function, which equals 0 for negative and 1 for positive arguments. Due to the instabilities related to the existence of a step function, the drag calculations are smeared out.

The simplified RANS equations are linearised using Taylor expansion and only the terms with order zero and one are considered. The zeroth order equations correspond to the case without any perturbations to the flow, meaning that there are no turbines. The drag force of order one, f_x^1 , is defined by inserting the first-order equations to a Chapeau function. The resulting equations are further simplified using Fourier transformation in which two mixed spectral variables are defined along x and y directions. A new numerical scheme is applied to overcome the difficulties of solving a linearised model for flows over small values of z_0 which is applicable for offshore locations with low roughness lengths where the wakes are more noticeable. Further elaboration of the scheme is done by Ott et al. [36], together with the validation of the model for certain test cases.

2.2 Modelling in OrcaFlex

There are numerous software available for the simulation and analysis of marine structures. Examples are OrcaFlex, Simo-Riflex, FAST, and DeepLines™. The whole model construction and simulation in this study is conducted using OrcaFlex. It is capable of modelling a wide range of marine systems, such as wind turbines, ships, risers, moorings, pipeline installations, and many other installations for which static, quasi-static, and dynamic analysis is needed. This section will describe the working principle and theories of OrcaFlex that are used in the model construction for the present study.

2.2.1 Coordinate Systems

OrcaFlex uses one global coordinate system GXYZ, where G is the global origin and GX, GY and GZ are the global axes directions. In addition, there are a number of local coordinate systems, generally one for each object in the model. Generally, Lxyz to is used to denote a local coordinate system. Another coordinate system that is utilised for Line End orientation is denoted by Exyz. All the coordinate systems are right-handed, as shown in the following Figure 2.11. This figure shows the global axes and a vessel, V, with its own local vessel axes Vxyz. Positive rotations are clockwise when looking in the direction of the axis of rotation.

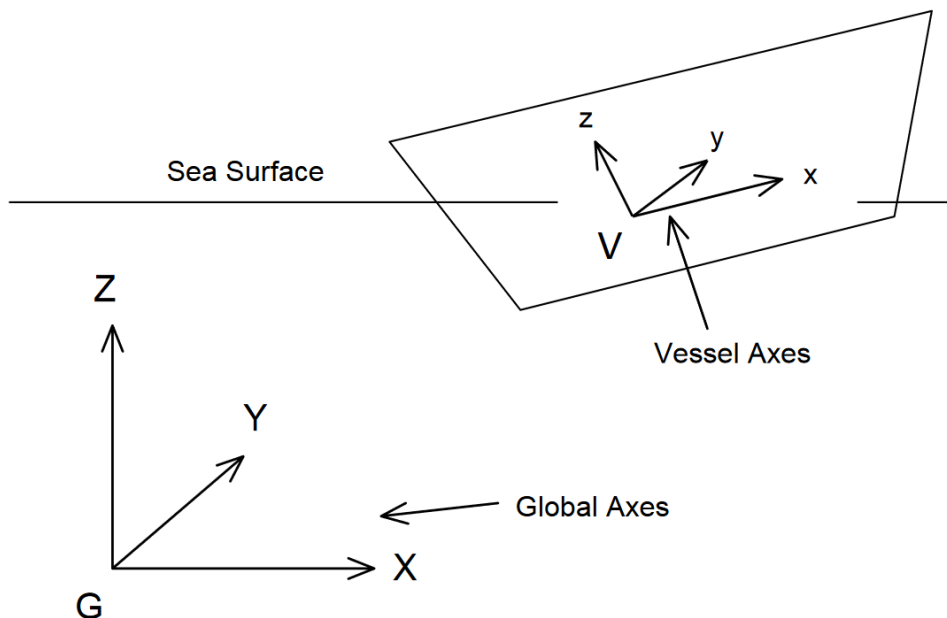


Figure 2.11: *Coordinate systems in OrcaFlex (taken from [37]).*

2.2.2 Directions Conventions

Directions and headings are specified in OrcaFlex by inputting the azimuth angle of the direction, in degrees, measured positive from the x-axis towards the y-axis, as shown in Figure 2.12. Directions for environmental loads such as waves, current, and wind are defined by giving the direction in which the load is progressing, relative to global axes.

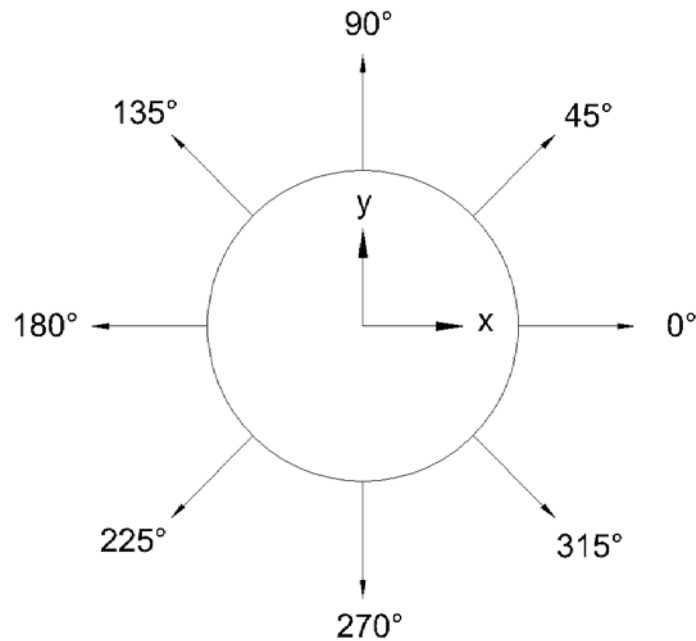


Figure 2.12: *Direction relative to the axes in OrcaFlex (reproduced from [37])*

2.2.3 Object Connections

Most objects in the OrcaFlex model can generally be “fixed”, “anchored”, “free” or “connected” to some other model object as a “child”. The model object to which a child is connected to is called the “parent”. By convention, the child is described as being connected to the parent, not inversely. Each child object has one or more points at which it can be connected to a parent. Connections to most parent objects are made with respect to the local axes of the parent object. Once a connection has been made, the child connection point will be treated as if it were rigidly attached to the chosen point on the parent object.

Fixed and anchored objects remain the same relative to the global axes at all times. Free objects can move independently of other objects in response to wave loads, connected lines, or objects. The motions of a child object are controlled by its parent whereas the loads that act on the child

also influence the motion of the parent. For connection to another object, the connection coordinates are normally specified relative to the local axes of the parent. However, not all of the connection options are available for all model objects:

- Vessels, 3D buoys, and 6D buoys each have a single connection that can be free, fixed, anchored, or connected to a parent object.
- Shapes, constraints, turbines, and turbine tower ends each have a single connection that can be fixed, anchored, or connected to a parent object, but not free.
- Lines can be connected at each end and can also have connections at mid-line nodes. All of these can be fixed, anchored, or connected to a parent. End connections can also be free. However, a child line can be connected to another parent line, but not to itself.

2.2.4 Static Analysis

Static analysis is used to find the static equilibrium of the system before running the dynamic analysis. For an analysis where no external load is applied, it is called static analysis. If a steady external load is applied, it will be called steady-state analysis instead of static analysis. This static analysis computes the system balance under applied loads using an iterative process. This static analysis only considers self weight of the structural model, buoyancy, and hydrodynamic drag from currents and wind. Once the equilibrium has been calculated, the configuration of the line model can be computed.

2.2.5 Dynamic Analysis

The dynamic analysis is a time-based simulation for the motions of the model over a certain period starting from the initial position acquired by the static analysis. The dynamic analysis is carried out to determine the motion responses of the model due to the combination between wave loads, wind, currents, and other design parameters. A number of consecutive stages in the dynamic analysis represent the period of simulation, as shown in Figure 2.13. There is a build-up stage prior to the main simulation when the vessel and wave motions ramp up to its full magnitude from zero. This stage provides a smooth start and reduces the simulation time that is generated from static to full dynamic motion.

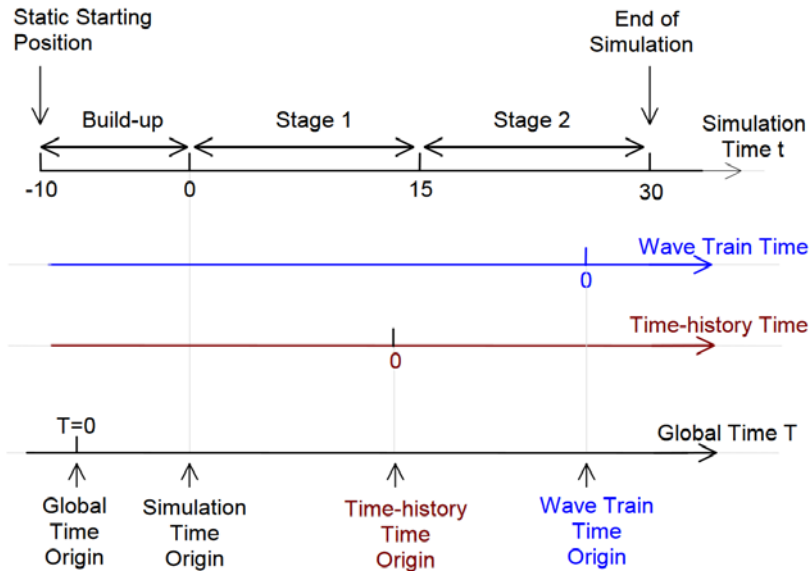


Figure 2.13: *Simulation Stages and Time in Dynamic Analysis (taken from [37])*

OrcaFlex implements Explicit and Implicit dynamic integration schemes to solve the equation of motion, as shown in Equation (2.20). Both schemes recompute the system geometry at every time step and so the simulation takes full account of all geometric non-linearities, including the spatial variation of both wave loads and contact loads. The explicit scheme is forward Euler with a constant time step. At the start of the time simulation, the initial positions, and orientations of all objects in the model, including all nodes in all lines, are known from the static analysis. The forces and moments acting on each free body and node are then calculated. For implicit integration, OrcaFlex uses the Generalised- α integration scheme as described by Chung and Hulbert [38]. The forces, moments, and damping, are calculated in the same way as for the explicit scheme. Then the system equation of motion is solved at the end of the time step.

$$M(p, a) + C(p, v) + K(p) = F(p, v, t) \quad (2.20)$$

Where,

- $M(p, a)$ = System inertia load
- $C(p, v)$ = System damping load
- $K(p)$ = System stiffness load
- $F(p, v, t)$ = External load
- p = Position
- v = Velocity
- a = Acceleration
- t = Time of simulation

2.2.6 Hydrodynamic Loads

Morison's equation was originally formulated for calculating the wave loads on fixed vertical cylinders. There are two force components; one related to the inertia force caused by water particle acceleration, and one related to the drag force caused by water particle velocity. For moving objects, the same principle is applied. However, the force equation is modified to take account of the movement of the body. OrcaFlex calculates hydrodynamic loads on lines, 3D buoys and 6D buoys using an extended form of Morison's Equation. The extended form of Morison's equation used in OrcaFlex is:

$$F_w = (\Delta a_w + C_a \Delta a_r) + \frac{1}{2} \rho V_r |V_r| C_D A \quad (2.21)$$

Where,

- F_w = Wave force
- Δ = Mass of fluid displaced by the body
- a_w = Fluid acceleration relative to the earth
- C_a = Added mass coefficient for the body
- a_r = Fluid acceleration relative to the body
- ρ = Density of water
- V_r = Fluid velocity relative to the body
- C_D = Drag coefficient for the body
- A = Drag area

2.2.7 Lines

For a line object, OrcaFlex can represent the line as a “finite element” or “analytic catenary”. The finite element representation of a line is shown in Figure 2.14. The line is segregated into a series of line segments (or discretisation length) which are then modelled by straight massless model segments with a node at each end. The model segments only model the torsional and axial properties of the line. Other properties such as mass, weight, and buoyancy, are all lumped to the nodes as indicated by the arrows in Figure 2.14. Nodes and segments are numbered starting from 1 in sequence from End A of the line to End B. Segment, n , joins nodes n and $(n+1)$. To compute the tension of a segment, OrcaFlex calculates the distance, rate of change of the distance between the nodes at the ends of the segment, and also the segment axial direction. Segment axial direction is the unit vector in the direction joining the two nodes.

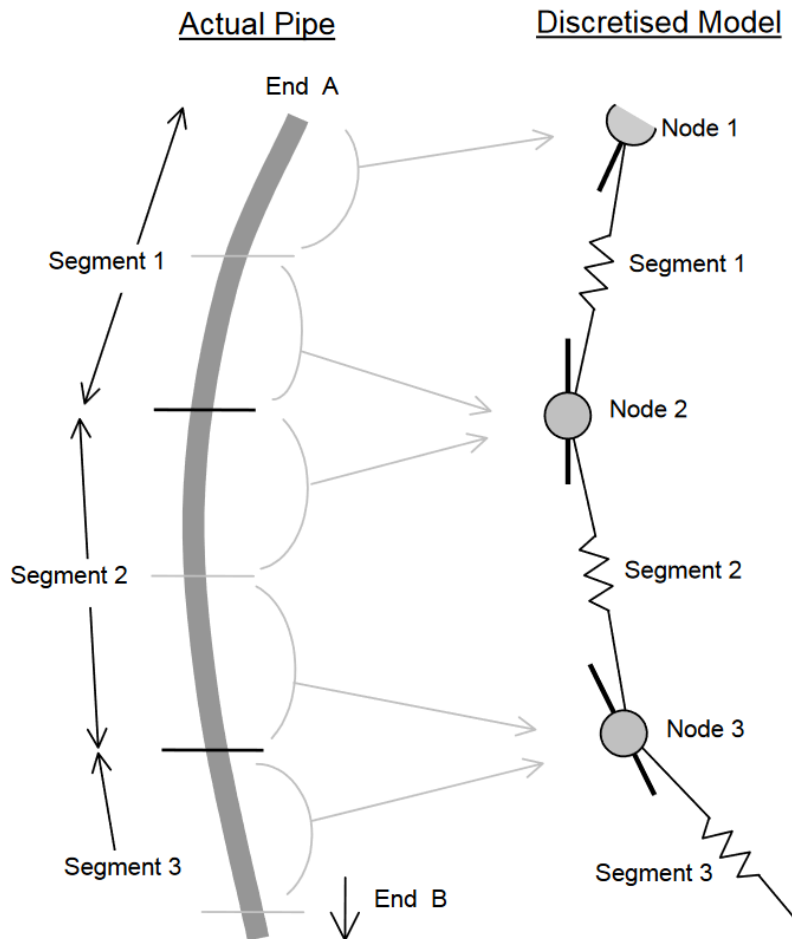


Figure 2.14: OrcaFlex line object (taken from [37]).

The analytic catenary representation is primarily intended to ease quasi-dynamic mooring analysis in OrcaFlex, in which the mooring line loads are computed from analytic catenary equations. These equations consider the line as a single continuous object, meaning that no discretisation into constituent nodes is required. The analytic catenary representation does not account for dynamic effects. Thus, for a given set of input parameters, the equations purely predict a static configuration of the line. This may be a practical approximation in cases where the inertia and bend stiffness of the mooring lines can be ignored, and where damping can instead be represented by another vessel. The bottom end of the line is referred to as the anchor and the top end as the fairlead.

At the start of the statics calculation, OrcaFlex will calculate a lookup table of analytic catenary solutions for each line that uses this representation. Each solution in the series corresponds to a particular horizontal and vertical separation between the anchor and the fairlead. The anchor is kept fixed, so each solution is determined fully by the position of the top end of the line. These top-end positions collectively form a two-dimensional solution grid of points in the vertical plane containing the anchor and the fairlead. During a simulation, the top-end of each line may move through its solution grid with the moving object to which it is connected to, as the example shown in Figure 2.15. The force that the top end applies to this object is calculated by interpolation in this grid, based on the instantaneous position of the fairlead.

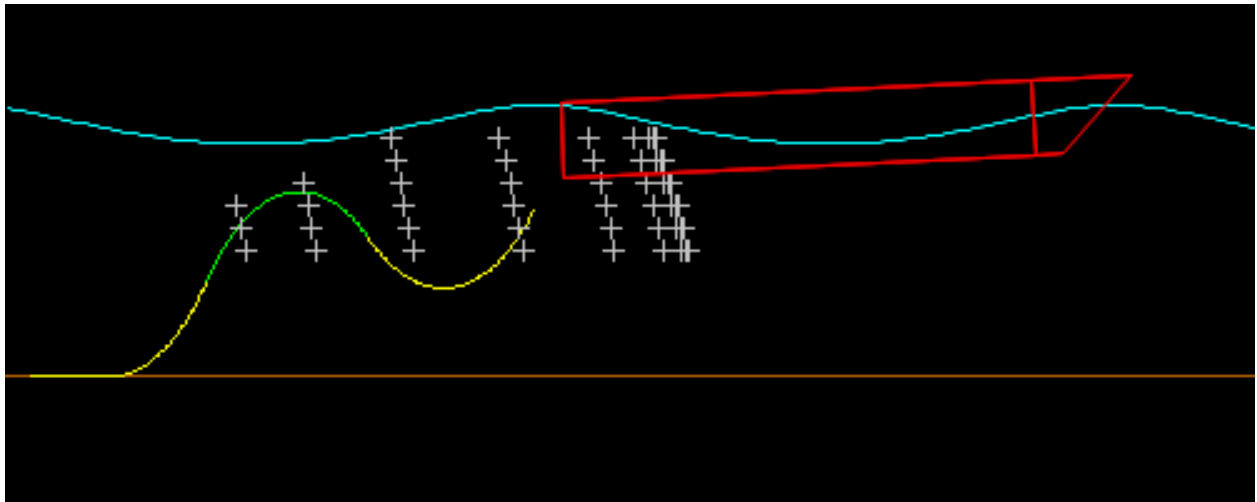


Figure 2.15: A typical analytic catenary solution for a two-dimensional grid (taken from [37]).

2.2.8 Turbines

Turbines are used to model horizontal axis wind turbines. The OrcaFlex turbine object is made up of dedicated models for the generator, gearbox, hub and blades. Blade pitch and generator torque control are implemented through the use of an external functions. Blades can be represented as rigid objects, or allowed to be flexible to capture aeroelastic coupling effects. The blade structural model is similar to that for lines.

Aerodynamic loading is calculated in OrcaFlex using a blade element momentum (BEM) method adapted from AeroDyn [39]. Initially, a quasi-steady BEM model or equilibrium wake is assumed, in which the induction factors for each blade segment are recalculated at every time step as a function of the instantaneous relative flow conditions.

2.2.9 Vessels

Vessels in OrcaFlex present a boundary condition of the model. Vessel motion can be defined by very simple data sources, such as time histories, prescribed or harmonic motion, or may even be externally calculated. OrcaFlex vessels are primarily intended to model rigid bodies that are large enough for wave diffraction to be significant, such as ships, floating platforms, barges, TLPs or semi-subs. To represent a floating body, the OrcaFlex vessel requires a lot of data to define its properties. The case-specific data, such as its position and how its motion should be calculated, are given on the vessel data type form.

2.2.10 Constraints

Constraint objects provide an enhanced and versatile means of connecting objects. They can fix individual degrees of freedom (DOFs), introduce individual DOFs, or impose displacements on individual DOFs. A constraint includes two coordinate systems, or frames of reference: the in-frame and the out-frame. The in-frame is rigidly coupled to a parent object and thus translates and rotates with the parent. Children of the constraint are rigidly coupled to the out-frame and so translate and rotate with the out-frame. The out-frame can translate and rotate independently in all six DOFs relative to the in-frame.

2.2.11 6D buoys

The buoy is treated as a cylindrical rigid body with 6 DOFs, of which 3 are translational and 3 rotational. The equation of motion has the following contributions:

- Weight: The weight force is applied at the centre of mass.
- Buoyancy for spar buoy: Separate buoyancy forces are calculated and applied to each cylinder. The buoyancy force on an individual cylinder is given by:

$$\text{Buoyancy Force} = \rho \times g \times \text{WettedVolume} \quad (2.22)$$

WettedVolume is the volume of the cylinder body below the water surface. This force is applied vertically upwards at the centroid of that wetted volume.

- Hydrodynamic Loads: Generally, the hydrodynamic loads are calculated using Morison's equation

2.3 Power Cables

The cabling infrastructure is a critical component in offshore wind installation. Cable design must consider both electrical and mechanical performance requirements. For offshore wind energy, subsea power cables are utilised to transport energy from the wind turbine to the shore. It can also be used to transmit power to other sea-based facilities, such as for the Hywind Tampen project powering offshore oil and gas facilities. According to Srinil et al. [8] the cable industry is experiencing a huge growth in demand for subsea power cables. More robust power cable configurations are required as technology pushes sites further from shore and into deeper waters in extreme climates. Cable designs must be adjusted based on the system location, technical challenges, and infrastructure for safe and efficient electrical delivery. Subsea power cable design faces several technical and economic challenges, with the water depth being a key factor.

As shown in Figure 2.16, different types of subsea cables are used in different applications to deliver generated electricity from a wind turbine to shore or an offshore facility. This study focuses on the inter-array power cable between two FOWTs.

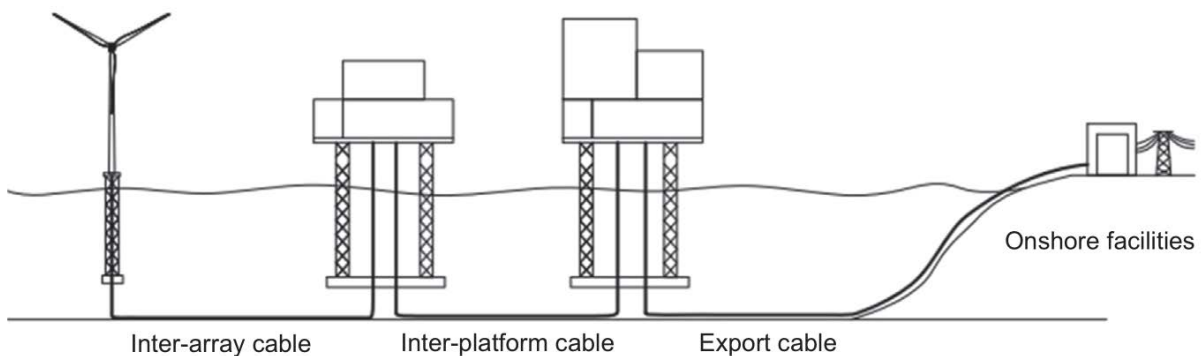


Figure 2.16: Subsea power cables for different applications (taken from [8]).

2.3.1 Dynamic Power Cables

Cables for dynamic applications must have optimal bend stiffness to avoid damage during installation, where greater cable lengths are managed under higher stresses [40]. Increased bending stiffness facilitates handling and provides some kinking resistance. This ensures that the installation window is as large as possible. Additionally, increased cable weight promotes the cable's self-stability and reduces the need for costly stability measures to keep the cable in place along the path.

Greater terminated axial load carrying capacity is also addressed at the HOP. This is due to the elevated stress in dynamic applications produced by waves and currents. Additionally, a long and heavy hanging cable must be managed during installation and operation. Since heavier cables are more likely to experience higher loading during installation, cable axial strength elements must be scaled proportionately. For dynamic cables, typical working load limitations are at least 5:1 compared to 4:1 for static cables [40]. Whereas the study by Rentschler et al. proposed a safety factor of 3:1 [41].

2.3.2 General Design

Subsea power cables come in a variety of forms. According to Beckman et al. [42], each cabling system is custom-designed for a specific application and environment, making repairs and maintenance difficult. Figure 2.17 shows some of the most typical characteristics of a standard subsea power cable [43].

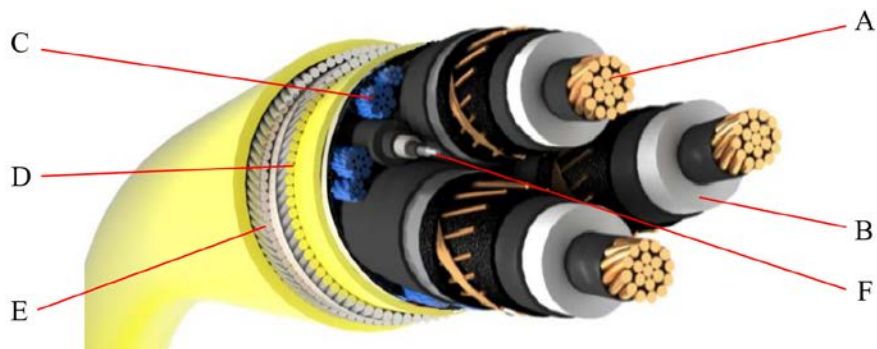


Figure 2.17: Typical cross-section of dynamic subsea cable (taken from [44]).

- A. Conductor core: Transmits the electrical current and is made up of copper or aluminium wires.
- B. Electrical Insulation: Insulates the conductors. Typical materials are cross-linked polyethylene, oiled paper, or ethylene propylene rubber.
- C. Sheath: Acts as a water blockade and shields the cable against fault electrical current.
- D. Armour: Metallic armature usually comprises two layers of galvanised steel wires that protect against impact and provides mechanical strength.
- E. Protective Sheath: External layer that gives abrasion strength, made from propylene.
- F. Fibre optic cables: Allows the transfer of data between turbines and the other end of the cable.

2.3.3 Conductor Materials

The conductor material chosen has a direct impact on the core size of the power cable. Copper or aluminium conductors are commonly used in the power cable for wind farm applications. Copper conductors are small due to their high conductivity. While aluminium conductors are larger than copper conductors due to its low conductivity to meet electrical current carrying requirements and transmit the same amount of power.

Historically, the capital cost of aluminium cores drove industrial preference. This is due to its higher availability in nature and cheaper capital cost (CAPEX). However, given present market pricing for both materials and from a life-cycle-cost perspective (OPEX), there is an insignificant difference between them in terms of price per unit of power transmitted [45]. Aluminium cores need a larger conductor size than a copper cable for the same voltage rating. A larger core requirement increases the cable size, which in turn increases the cost. The increase in size further impacts the cost of installation and transportation to site considerations due to limitations of the installation vessel capacity. More importantly, aluminium cables show a larger power loss throughout the operational life of a wind farm compared to copper cables.

Copper cores are more fatigue resistant than aluminium cores, allowing them to endure higher vibration amplitudes without cracking or breaking for extended periods. Copper also shows less creep and is less prone to failure due to the relative oxide properties compared to aluminium: copper oxide is soft, conductive, and breaks down quickly, whereas aluminium oxide is securely bonded and electrically insulating [46], making cable jointing more difficult. Aluminium is a highly reactive metal, making it more likely to corrode by exposure to seawater. Hence, a further mitigation process with associated costs is required during the manufacturing stage [47]. Table 2.1 summarises the benefits and drawbacks of each cable option.

Table 2.1: *Comparison of copper and aluminium conductor material properties*

Copper cable core	Aluminium cable core
<ul style="list-style-type: none">• Better conductivity• Heavier density• Higher material cost• Easier to process	<ul style="list-style-type: none">• Lesser conductivity (~60% vs copper)• Lower density• Lower tensile strength• More reactive metal

2.3.4 Dynamic Cable Configurations

Dynamic inter-array power cable configurations for floating wind farms were adapted from offshore risers and umbilicals used in the oil and gas sector for transporting fluids from the seabed wells to the platforms [48]. The commonly used configuration for umbilicals and risers are shown in Figure 1.3 (a) and Figure 1.3 (b) as catenary and lazy wave configurations. A fully suspended inter-array power cable configuration presented in this study is shown in Figure 1.3 (c).

For dynamic inter-array power cable configurations, the free-hanging catenary configuration in Figure 1.3 (a) is the simplest of all configurations. The effective tension of the cable in catenary configuration is governed by the unsupported weight of the hanging cable from the HOP to the touch-down point. An example of a free-hanging catenary configuration for dynamic application is the hanging cable during the cable laying operation from an installation vessel.

The lazy wave is configured using several buoyancy modules between the HOP and the touch down point. This type of configuration, as shown in Figure 1.3 (b) and Figure 2.18, is typically installed in shallow and intermediate water depths, such as for the floating wind farms Hywind Tampen [49] and Hywind Scotland [50]. Srinil [8] stated that the buoyancy modules used in lazy wave configurations must be designed carefully to get the optimal shape with the least tension possible and the optimal bend radius. The lazy wave design also helps to minimise the dynamic response of the cable by decoupling the motion of the floating structure from the cable in contact with the seabed. The buoyancy distribution is crucial in this setup. Figure 2.19 shows how a change in buoyancy distribution alters hang-off, arch bend, and touch-down of the lazy wave dynamic cable configuration. Rapha et al. [51] presented an engineering method to obtain static results for free-hanging catenary and lazy wave configurations with buoyancy modules attached between two FOWTs. Thies et al. [52] conducted dynamic simulations of lazy wave configurations to investigate the impact on load and fatigue when the buoyancy modules were added at various points along the cable in moderate water depth. The location and distribution of the buoyancy modules influenced the final shape and depth of the resulting lazy wave configuration. Thies found that lazy wave configuration depth close to the seabed to be the most suitable design that provides a good compromise between hang-off tensions and induced bending stresses. Rentschler et al. [53] discussed the impact of various buoyancy element distributions along dynamic power cables connected to a FOWT at intermediate and shallow water depths on curvature and tension. They proposed a genetic optimisation approach to change the position of the buoyancy elements in the

lazy wave configuration. Rentschler managed to reduce the accumulative length of the buoyancy sections up to 23% of the total cable length using this algorithm. Rentschler et al. [41] also optimised the lazy wave configuration for a power cable connected to a FOWT by utilising a Fitness Factor in static analysis. The Fitness Factor was described as the sum of the normalised minimum breaking load and the normalised minimum bend radius. The cable tension in the lazy wave configuration in water depths up to 200 m could be reduced by half by using this optimisation method. Ikhenicheu et al. [40] presented the existing configurations of offshore dynamic cable system design in their report.

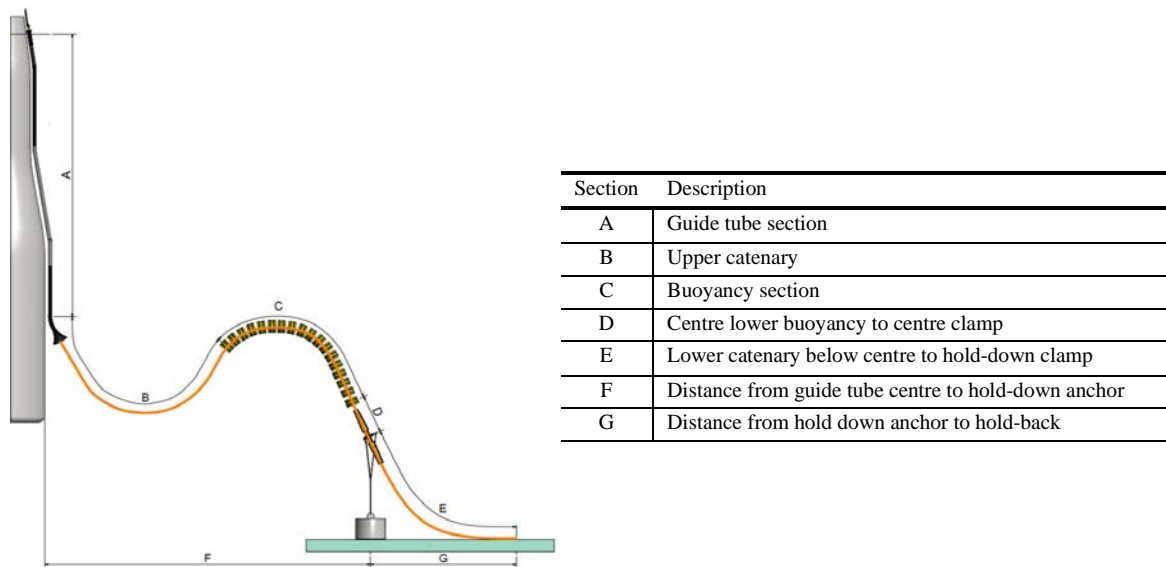


Figure 2.18: Inter-array lazy wave cable configuration for Hywind Scotland (taken from [50]).

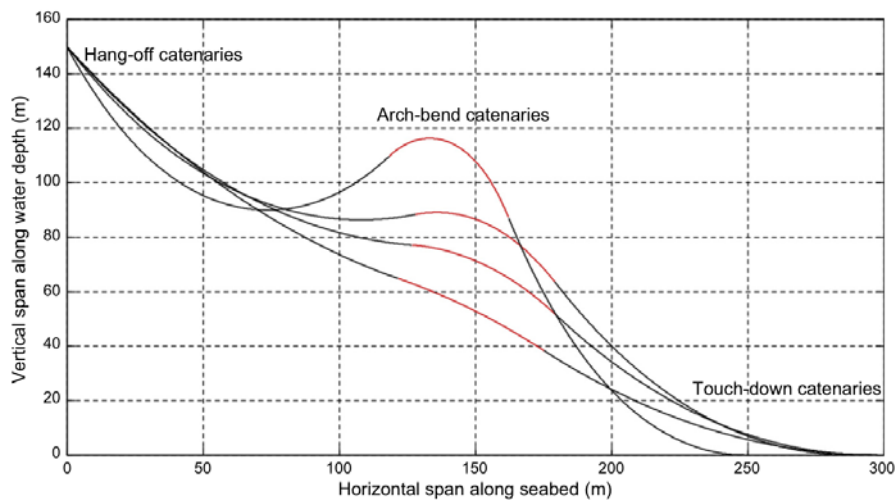


Figure 2.19: Effect of buoyancy distribution (red line) on the shape of a lazy wave dynamic cable (taken from [8]).

To the author's knowledge, Schnepf et al. [54] are the first to propose a buoys setup for the fully suspended inter-array power cable configuration. The proposed buoys setup is shown in Figure 2.20. They examined the distribution of buoys on a fully suspended power cable configuration between a FOWT and a Floating Production Storage and Offloading Unit (FPSO). The evenly distributed buoys over the entire cable length resulted in the lowest tension. Further, they stated that the motions of the floaters in dynamic analysis resulted in a 24% increase in cable tension from the steady-state analysis. Another study was done by Schnepf et al. [9] using the same buoys setup to study the dynamic response of fully suspended inter-array power cables in W-configuration and 2W-configuration between two FOWTs. The research was done using several buoyancy modules and buoys separately. The configuration using 150 buoyancy modules resulted in a much larger maximum effective tension compared to the configuration using 2 or 3 buoys.

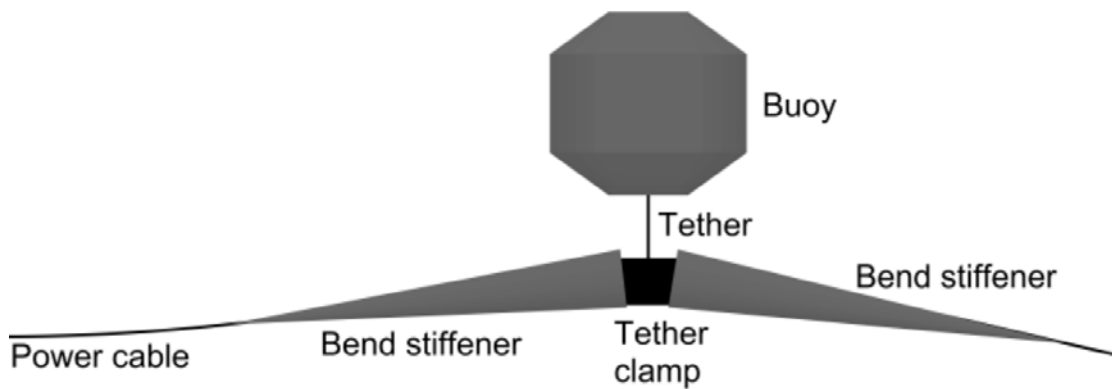


Figure 2.20: *The buoy setup for a fully suspended configuration proposed by Schnepf et al. [9].*

2.3.5 Ancillary Equipment for Cables

For marine cables, there are various kinds of cable ancillaries intended for different purposes. Bend stiffeners and buoyancy devices are the two ancillaries considered for the setup of a fully suspended inter-array power cable configurations in this study.

Bend Stiffeners

Bend stiffeners restrict the curvature of a cable by increasing local stiffness at the connecting region. Increased local stiffness will decrease the bending stresses of the cable and reduce its curvature to a minimum. Bend stiffeners come in a variety of shapes and sizes. An example of a bend stiffener is shown in Figure 2.21. Static bend stiffeners are mostly used for installation protection, while dynamic bend stiffeners are utilised for protection during the service life. Some manufacturers also recommend split bend stiffeners for ease of installation. The design of a bend stiffener mainly considers the following factors:

- Cable diameter
- Operational environment (water)
- Interface requirements with load-bearing steelwork/end termination
- Fatigue cycles and loads. (for the design of a dynamic bend stiffener)
- Tension and angle combination. (for the design of a dynamic bend stiffener)



Figure 2.21: An exemplary bend stiffener (taken from [55]).

Bend stiffeners composed of moulded polyurethane elastomers are commercially available for offshore components. Polyurethane elastomer was chosen because of its low modulus and high elongation at break. This material is lightweight and does not require any corrosion protection. Each bend stiffener is customised to prevent the cable from exceeding the minimum bending radius limit under certain stress and angle combinations. This is to ensure that load situations (tension vs angle) in each application are met. The bend stiffeners should be long enough for this application

to prevent the cable from exceeding its radius of curvature at the end of the bend stiffeners. However, the length should not be too long considering the handling on the deck of the installation vessel.

Buoyancy Devices

Wherever there is a requirement to install a floating offshore facility, such as the lazy wave and the fully suspended cable configurations, it is required for the system to be comprised of one or more buoyancy devices. To avoid damage to the system, these configurations are often required to be designed and held in specific subsea geometries. This design is particularly appealing for deepwater applications. One of the most common methods to construct these geometries is to attach discrete buoyancy devices to the outside of the umbilical. The three main functions of distributed buoyancy devices are to provide upward force, damping stability, and weight to a specific location along with the umbilical. Examples of buoyancy devices such as buoys and buoyancy modules are shown in Figure 2.22.

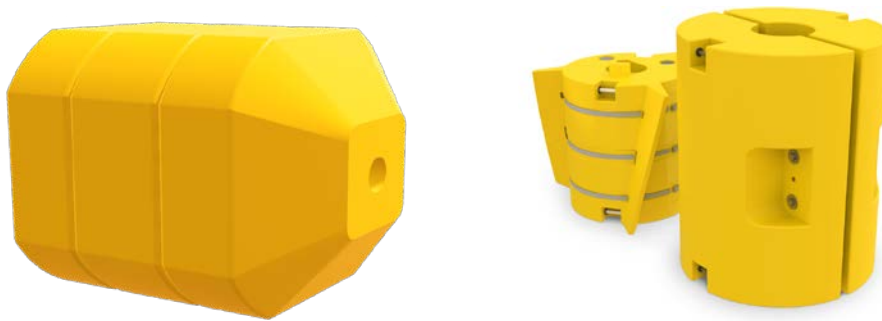


Figure 2.22: *Buoy (left), and buoyancy module (right) (taken from [56]).*

The buoyant forces provided by these buoyancy devices should not migrate or degrade over the design life of the umbilical. The number of these buoyancy devices can be changed, and the location of each buoyancy device can be adjusted to meet a specific buoyancy requirement. The buoy typically consists of a single buoyancy element with a hollow tubular section. While the buoyancy module generally consists of two primary components:

- The buoyancy element, with two halves of polyethylene outer shell filled with a high-performance syntactic foam core, is held together by two corrosion-resistant bolts or securing straps.
- An internal clamp is attached directly to the dynamic cable and therefore designed to the minimum outer diameter of the dynamic cable.

2.4 Environmental Conditions

For FOWTs, environmental loads exerted on the structures include currents, waves, and winds. The design of the cable configurations is significantly influenced by the impact of these loads on the structures.

2.4.1 Current

Currents can cause significant loads on slender structures such as subsea cables, mooring lines, and marine risers. Storm-generated currents, circulation currents (oceanic-scale circulation patterns), tidal currents (astronomical tides), loop, and eddy currents are all examples of currents. However, extreme current events for each of the current components do usually not occur simultaneously. According to DNV [57], the total currents are the vector of these currents:

$$V_c(z) = V_{c,tide}(z) + V_{c,wind}(z) + V_{c,circ}(z) + \dots \quad (2.23)$$

Where,

$V_c(z)$ = Total current velocity at level z (m/s)

$V_{c,tide}(z)$ = Tidal current velocity at level z (m/s)

$V_{c,wind}(z)$ = Wind-induced current velocity at level z (m/s)

$V_{c,circ}(z)$ = Circulational current velocity at level z (m/s)

Tidal currents are predictable, following the harmonic astronomical motions of the planets. The highest and lowest astronomical tides are preceded or followed by the maximum tidal current. Deep ocean tidal currents are normally weak, although coastline patterns amplify them. Inlets and straights in coastal areas have strong tidal currents. Therefore, tidal currents and storm surge currents are of comparatively low importance in deep water. However, the total current may still be very significant in certain geographic areas, such as Norwegian water. This is due to a strong surface current velocity of up to 1 m/s can be observed in the Norwegian water due to a sudden outflow of brackish water from the Baltic Sea into the North Sea [58], as well as the wind-generated current.

When precise field measurements are unavailable, DNV recommended practice [57] suggests that the variation of tidal current with depth can be simulated using a Power Law profile, assuming unidirectional current:

$$V_{c,tide}(z) = V_{c,tide}(0) \left(\frac{d+z}{d} \right)^\alpha \quad \text{for } z \leq 0 \quad (2.24)$$

Where,

- $V_{c,tide}(0)$ = Tidal current at the still water level
- d = Depth to still water level (taken positive)
- α = Exponent, typically taken at $\alpha = \frac{1}{7}$

Wind stress and atmospheric pressure gradients cause wind-generated currents. [57]. Wind-generated current can be represented as a linear profile from $z \leq -d_0$ to still water level:

$$V_{c,wind}(z) = V_{c,wind}(0) \left(\frac{d_0+z}{d_0} \right) \quad \text{for } -d_0 \leq z \leq 0 \quad (2.25)$$

Where,

- $V_{c,wind}(0)$ = Wind-generated current at still water level, $V_{c,wind}(z) = 0$ for $z \leq -d_0$
- d_0 = Wind-generated current depth reference, typically taken at $d_0 = 50m$

If statistical data is not available, wind-generated current at the still water level, $V_{c,wind}(0)$, in deep water along an open coastline can be calculated as:

$$V_{c,wind}(0) = kU_{1hr,10m} \quad \text{for } 0.015 \leq k \leq 0.03 \quad (2.26)$$

Where,

- k = Roughness height
- $U_{1hr,10m}$ = 1 hour sustained wind speed at a height 10 m above sea level

2.4.2 Waves

Current is typically dominant in deeper water applications, while wave motions tend to have a dominant impact in shallow water applications. The statistical description of waves, the load they impose, and the theory of the structural response to these waves will be discussed in this part.

Statistical Description of Sea States

Irregular waves are modelled using sea-surface elevation spectra. These spectra provide information about the energy content of the sea condition as a function of the wave frequencies of the single wave trains. According to Faltinsen's book [59], the results from irregular waves can be derived by adding the data from regular waves. The wave elevation can be described as follows for long-crested irregular seas:

$$\zeta = \sum_{j=1}^N A_j \sin(\omega_j t - k_j x + \epsilon_j) \quad (2.27)$$

Where,

t = Time

ϵ = Phase

ω = Angular frequency

k = Wave number

A = Amplitude.

Additionally, A can be described in terms of its wave spectrum:

$$\frac{1}{2} A_j^2 = S(\omega_j) \Delta\omega \quad (2.28)$$

Where $\Delta\omega$ is the distinction between consecutive frequencies, the elevation of the wave is Gaussian distributed, having a mean of zero and a variance of:

$$\sigma^2 = \int_0^{\infty} S(\omega) d\omega \quad (2.29)$$

The wave spectrum assumes that the sea is a stationary random process, suggesting that it is a brief description of the sea condition. The sea is defined by the peak period T_p , the significant wave

height H_s , where H_s is the mean height of one-third of the highest waves in the sea condition and T_p is the wave spectrum's peak frequency. Commonly, either the Pierson-Moskowitz spectrum (1964) for fully developed sea states or the Joint North Sea Wave Project (JONSWAP) spectrum (1973) for developing sea states is used to model a wave spectrum in the Norwegian Sea. The International Ship and Offshore Structures Congress (ISSC) recommended the modified Pierson-Moskowitz spectrum. It is defined by:

$$\frac{S(\omega)}{H_s T_1} = \frac{0.11}{2\pi} \left(\frac{\omega T_1}{2\pi}\right)^{-5} \exp \left[-0.44 \left(\frac{\omega T_1}{2\pi}\right)^{-4} \right] \quad (2.30)$$

Where,

T_1 = mean wave period defined as $T_1 = (2\pi m_0)/m_1$

$m_k = \int_0^\infty \omega^k S(\omega) d\omega$

H_s is often redefined as $H_s = 4\sqrt{m_0}$.

Hasslemann et al. [60] in the Joint North Sea Wave Project (JONSWAP), came up with a variation of the Pierson–Moskowitz spectrum that considers the effect of fetch limits and resulted in a more sharply peaked spectrum. The variation of the Pierson–Moskowitz spectrum is defined as:

$$S(f) = \frac{\alpha g^2}{(2\pi)^4 f^5} \exp \left[-\frac{5}{4} \left(\frac{f}{f_0}\right)^{-4} \right] \gamma^a \quad (2.31)$$

Equation (2.31) can also be rewritten as:

$$S(\omega) = 155 \frac{H_s^2}{T_1^4 \omega^5} \exp \left(\frac{-944}{T_1^4 \omega^4} \right) 3.3^a \quad (2.32)$$

Where,

$$a = \exp \left[-\left(\frac{0.191\omega T_1 - 1}{\frac{1}{2^{\frac{1}{2}}\sigma}} \right)^2 \right] \quad (2.33)$$

Loads from Waves

The load from the wave acting on the FOWT can be calculated using Morison's equation. As formulated by Faltinsen [59], the general Morison's equation expresses the horizontal force dF on a strip of the length dz of a rigid vertical cylinder as shown in Figure 2.23 as:

$$dF = \rho \frac{\pi D^2}{4} dz C_M a_1 + \frac{\rho}{2} C_D D dz |u|u \quad (2.34)$$

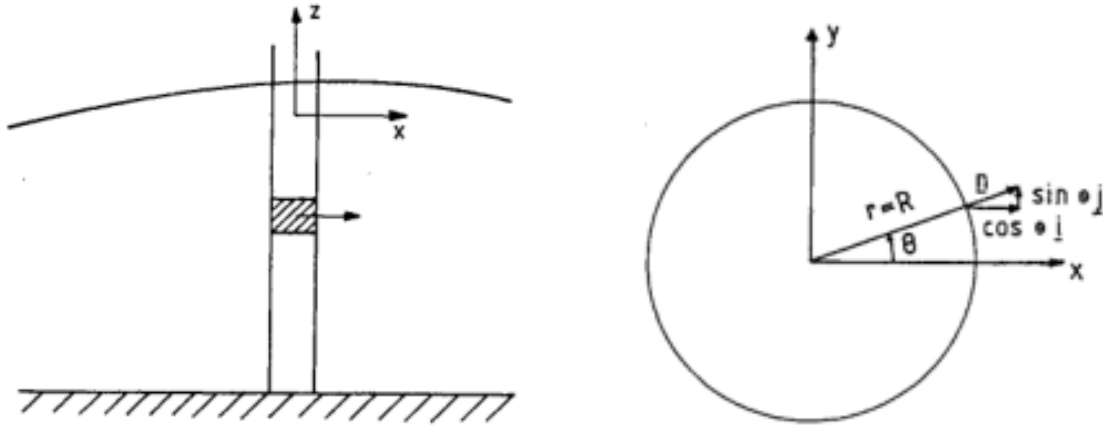


Figure 2.23: Horizontal submerged cross-section of a vertical cylinder (taken from [59]).

Where ρ is the mass density of the water, D is the cylinder diameter, u and a_1 are the horizontal undisturbed fluid velocity and acceleration at the midpoint of the strip, C_M is the mass coefficient, and C_D is the drag coefficient. For a moving cylinder, Morison's equation can be modified as:

$$dF = \frac{\rho}{2} C_D D dz (u - \dot{\eta}_1) |u - \dot{\eta}_1| + \rho C_M \frac{\pi D^2}{4} dz a_1 - \rho (C_M - 1) \frac{\pi D^2}{4} dz \dot{\eta}_1 \quad (2.35)$$

Dots in Equation (2.35) indicate time derivatives, u and a_1 are position dependent [59].

Response

From linear theory, results in irregular waves can be obtained by adding results from regular waves of different amplitudes, wavelengths, and propagation directions. Considering wave elevation for a long-crested irregular sea in Equation (2.28), the steady-state response (i.e., heave or pitch motion) can be written as:

$$A_j |H(\omega)| \sin[\omega_j t - \delta_j(\omega) + \epsilon_j] \quad (2.36)$$

The term $|H(\omega)|$ is the transfer function, which is the response amplitude per unit wave amplitude. The response can be any linear wave-induced motion or load on the structure. Having obtained the response due to one wave component, the response from different wave components can be linearly superposed and written as:

$$\sum_{j=1}^N A_j |H(\omega)| \sin[\omega_j t - \delta_j(\omega) + \epsilon_j] \quad (2.37)$$

Where $|H(\omega)|$ and $\delta_j(\omega)$ are functions of frequency, ω .

2.4.3 Wind

Several theories can be used to describe the profile of the wind speed. The wind speed may vary with the height, and the gradient of the wind speed profile is controlled by the atmospheric stability as well as the terrain conditions. Due to the selection of the Norwegian sea as the location for this study, the Norwegian Petroleum Directorate (NPD) spectrum is used as the wind speed profile [61].

The NPD spectrum is defined as:

$$S(f, z) = 3.2U_{ref}^2 \left(\frac{z}{10}\right)^{0.45} [1 + \tilde{f}^n]^{-5/3n} \quad (2.38)$$

Where,

$$n = 0.468$$

$$U_{ref} = 1 \text{ hour mean speed at an elevation of 10 m above MWL (m/s)}$$

$$z = \text{Elevation above MWL}$$

\tilde{f} is defined as:

$$\tilde{f} = 172f \left(\frac{z}{10}\right)^{2/3} \left(\frac{U_{ref}}{10}\right)^{-3/4} \quad (2.39)$$

The associated 1-hour mean wind speed is:

$$U_z(z) = U_{ref} \left[1 + 0.0573 \sqrt{1 + 0.15U_{ref} \ln\left(\frac{z}{10}\right)} \right] \quad (2.40)$$

2.5 Marine Growth

Marine growth will increase the surface roughness and weight of a subsea structure. More than two decades of research on the consequences of surface roughness by Sarpkaya [62] demonstrated that the roughness alters the boundaries of hydrodynamic regimes from laminar to turbulent and the loading intensity. Through a flowchart of the load computation from the response surface model, Ameryoun et al. [63] modelled the effect of mussel roughness growth in the Gulf of Guinea and determined that it could result in a 50 % increase in drag force in one year. Spraul et al. [64] studied the effect of marine growth on the dynamic behaviour of a steep wave configuration in shallow water, which is a variation of the lazy wave configuration where the touchdown point is vertical to the seabed. They concluded that the net buoyancies of the cable and the modules combined, which are both heavily reliant on the marine growth thickness and density, were found to be the most critical configuration parameters. Based on experimental campaigns and on-site video footage, Decurey et al. [65] constructed a stochastic spatial model of mussel colonisation on a mooring line of a floating offshore wind turbine. In this research, the effect of marine growth is studied according to Det Norsk Veritas (DNV) standards [57,66,67] and Norsk Søkkel Konkurransesepisjon (NORSOK) standard [68].

2.5.1 Increased Diameter and Weight

The marine growth affects the effective hydrodynamic diameter of a tubular member. According to DNV [57], the hydrodynamic diameter to be considered for predicting the effects of increased mass and drag on tubular members is:

$$D_{mg} = D + 2t \quad (2.41)$$

Where,

D_{mg} = Effective diameter with marine growth

t = Thickness of marine growth layer, referring to Table 2.2

The mass of marine growth to be added to structural mass in the dynamic analysis is given by the volume and density ρ_{mg} of marine growth. The density and thickness of marine growth vary with the water depth depending on the location. For the Norwegian continental shelf (59° to 72° N), values adapted from NORSOK [68] can be referred to in Table 2.2.

Table 2.2: Thickness and density of marine growth and biofouling.

Depth (m)	56° to 59° N		59° to 72° N	
	Thickness t (mm)	Density ρ_{mg} (kg/m ³)	Thickness t (mm)	Density ρ_{mg} (kg/m ³)
Above +2	0	-	0	-
-15 to +2	100	1300	60	1325
-30 to -15	100	1300	50	1325
-40 to -30	100	1300	40	1325
-60 to -40	50	1300	30	1100
-100 to -60	50	1300	20	1100
Below -100	50	1300	10	1100

The additional weight of marine growth is given by:

$$W_{mg} = (\rho_{mg} - \rho_w)g \quad (2.42)$$

Where,

ρ_{mg} = Marine growth density

ρ_w = Density of seawater

g = Acceleration of gravity

The thickness of marine growth is assumed to increase linearly to the given values over 2 years after the structure has been placed in the sea.

2.5.2 Change in Drag Coefficient

According to DNV [57], the surface roughness, k , can be taken between 5×10^{-3} m to 5×10^{-2} m to determine the drag coefficient due to marine growth. However, NORSOK [68] precisely suggested the roughness to be taken as 2×10^{-2} m for depth 2 m below SWL.

The drag coefficient's dependency on roughness $\Delta = k/D_{mg}$ was stated as follows for both irregular and regular waves:

$$C_{DS}(\Delta) = \begin{cases} 0.65 & ; \Delta < 10^{-4} \text{ (smooth)} \\ (29 + 4 \log_{10} \Delta) / 20 & ; 10^{-4} < \Delta < 10^{-2} \\ 1.05 & ; \Delta > 10^{-2} \text{ (rough)} \end{cases} \quad (2.43)$$

For smooth and marine growth covered, i.e. rough, circular cylinders, the variation of the drag coefficient as a function of the Keulegan-Carpenter number, K_C , can be approximated by:

$$C_D = C_{DS}(\Delta) \cdot \Psi(K_C) \quad (2.44)$$

Where the wake amplification factor, $\Psi(K_C)$, in low K_C number ($K_C < 12$) can be taken as:

$$\Psi(K_C) = \begin{cases} C_\pi + 0.10(K_C - 12) & ; 2 \leq K_C \leq 12 \\ C_\pi - 1.00 & ; 0.75 \leq K_C \leq 2 \\ C_\pi - 1.00 - 2.00(K_C - 0.75) & ; K_C \leq 0.75 \end{cases} \quad (2.45)$$

Where $C_\pi = 1.50 - 0.024 \cdot (12/C_{DS} - 10)$. Alternatively, the wake amplification factor, $\Psi(K_C)$, can be taken from Figure 2.24.

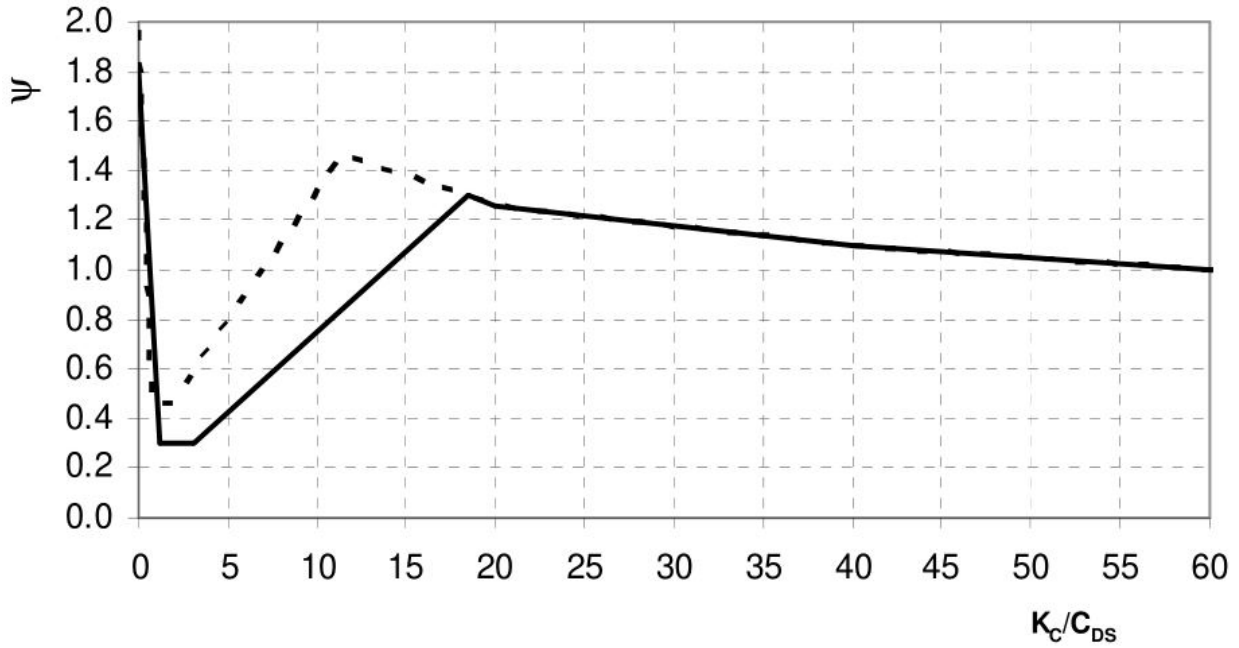


Figure 2.24: Wake amplification factor for smooth ($C_{DS}=0.65$ - solid line) and rough ($C_{DS}=1.05$ dotted line) (taken from [57]).

The asymptotic value for indefinitely large K_C is equal to the drag coefficient for steady current. The rise in K_C caused by the current may be considered for combined wave and in-line current action.

$$K_C^* = (v_m + v_c) \frac{T}{D} \quad (2.46)$$

Where,

v_m = Maximum wave velocity (m/s)

v_c = Current velocity (m/s)

T = Wave period (s)

D = Diameter or typical cross-sectional dimension (m)

As a result, adding a steady in-line current to the oscillatory wave motion has the effect of pushing C_D towards the steady value of C_{DS} . C_D should be equal to C_{DS} if current velocity, $v_c > 0.4v_m$.

3 METHODOLOGY AND NUMERICAL SETUP

The methodology of the study as well as the numerical setup of the model used are presented in this chapter. First, the rated and extreme environmental loading conditions are presented. Second, the construction of the OC3-Hywind model and its properties are described in detail. Then, the case study variables, constants, and the relevant ancillaries required for the suspended inter-array power cable configuration are defined. Following, the cable properties with the inclusion of marine growth effects are described. The workflow of the steady-state and dynamic simulation process is finally explained in an illustration. The whole model construction and simulation in this study is conducted using the numerical software OrcaFlex version 11.2c by Orcina Ltd. [37]. The software is coupled with Python version 3.8 to implement external scripts and functions.

3.1 Environmental Conditions

Two environmental loading conditions (LC) are defined in this study, which are a rated LC and an extreme LC. The environmental parameters for the rated LC is obtained from the OC3 report [69]. The environmental parameters for the extreme LC are taken from the Visund field [70] in the Norwegian Sea, which is close to the Hywind Tampen wind farm, and has a similar water depth of 320 m as used in this study. The location of Hywind Tampen and the neighbouring oil fields are shown in Figure 3.1. Table 3.1 summarises all the environmental LC parameters used in this study.

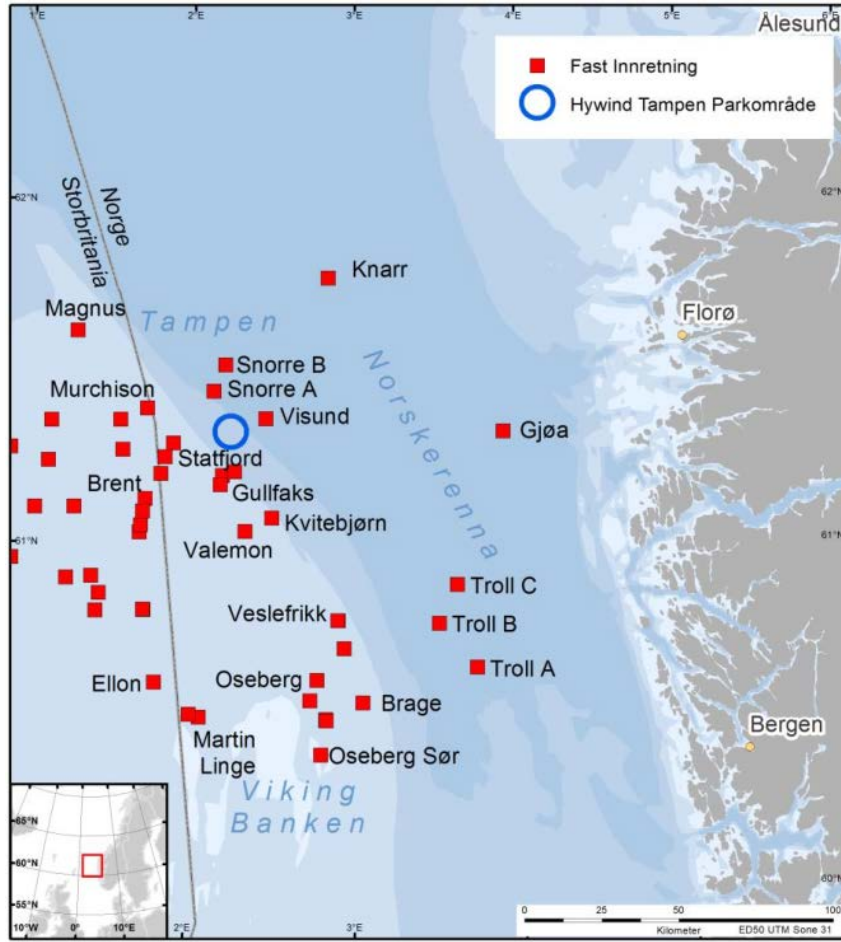


Figure 3.1: Location of the Hywind Tampen offshore wind farm in the Norwegian Sea (taken from [49]).

Table 3.1: Summary of the environmental loading conditions.

Loading Type	Rated LC	Extreme LC
Wind	V_{hub} : 11.40 m/s Type : NPD Spectrum v_{air} : $15 \times 10^{-6} m^2/s$ ρ_{air} : $1.225 kg/m^3$	V_{hub} : 37.45 m/s Type : NPD Spectrum v_{air} : $15 \times 10^{-6} m^2/s$ ρ_{air} : $1.225 kg/m^3$
Wave	Irregular waves: $H_s = 6$ m, $T_p = 10$ s, $\gamma = 2.872$ Type : JONSWAP	Irregular waves: $H_s = 13.2$ m, $T_p = 15.1$ s, $\gamma = 2.639$ Type : JONSWAP
Current	At the surface: 0.486 m/s	At the surface: 1.070 m/s

Note.

v_{air} : Air kinematic viscosity (m^2/s)

ρ_{air} : Air density (kg/m^3)

H_s : Significant wave height (m)

T_p : Peak wave period (s)

γ : Peak enhancement factor

3.1.1 Wind

The wind environmental data is specified as the Norwegian Petroleum Directorate (NPD) spectrum. Wind speed at hub height in the rated LC is 11.4 m/s based on the NREL report [69]. The wind spectrum of the rated LC is shown in Figure 3.2. For the extreme LC, reference is made to the study conducted by Kvitrud and Løland [70], in which a maximum wind speed of 29 m/s was reported during the storm “Tor” in January 2016. However, their study does not mention the height of which the reading was taken. Therefore, it is assumed that the reading was taken at 10 m height above SWL. Thus, the wind speed at hub height is recalculated based on this value as 37.45 m/s using the NPD profile [61]. The wind spectrum of the extreme LC is shown in Figure 3.3.

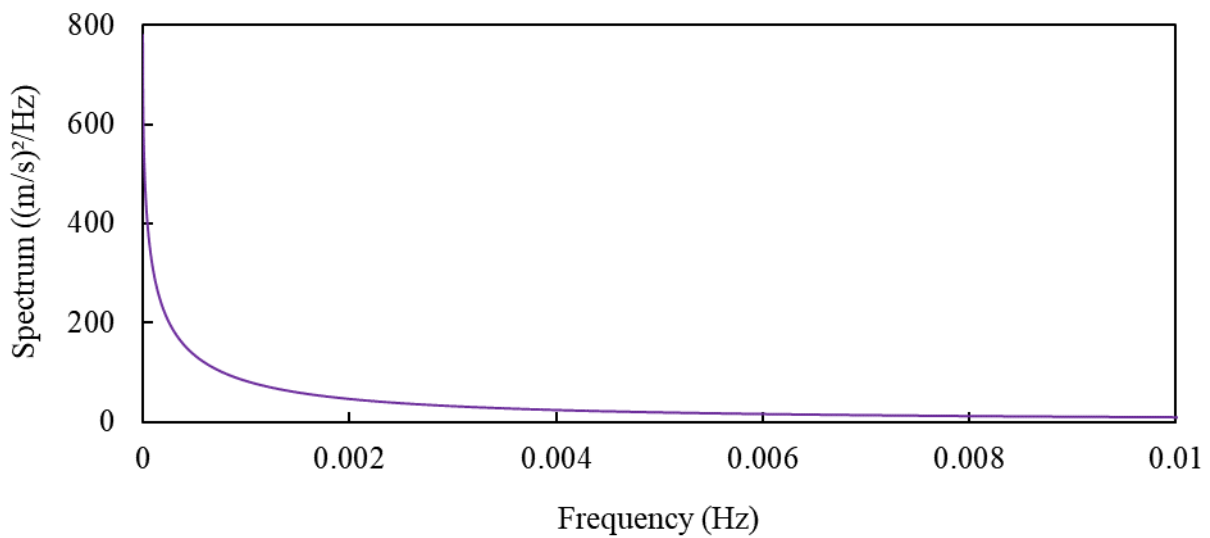


Figure 3.2: *Wind Spectrum of the rated LC.*

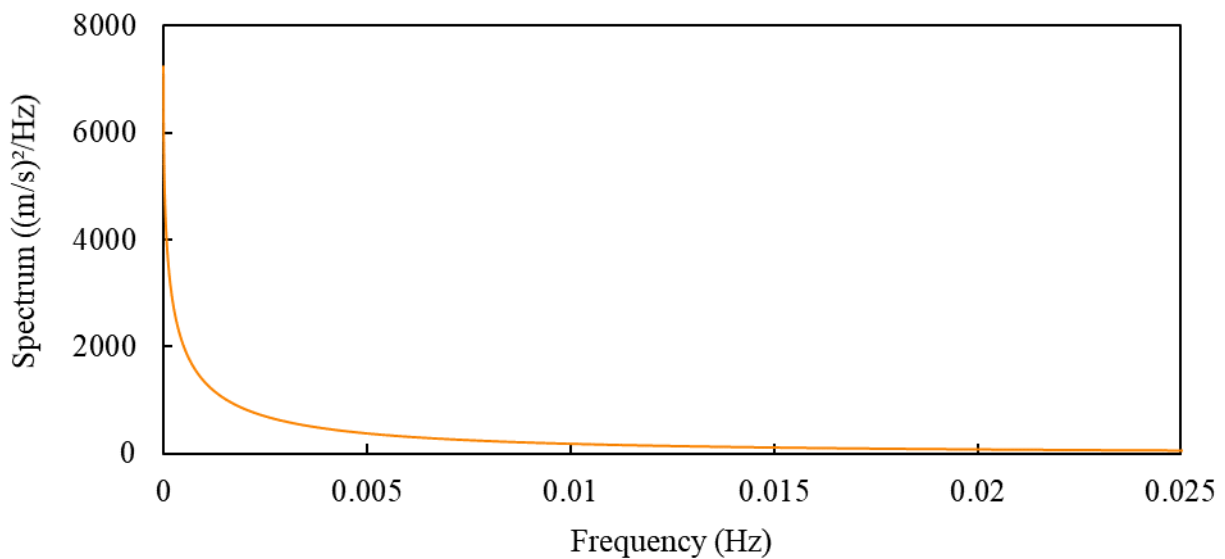


Figure 3.3: *Wind spectrum of the extreme LC.*

3.1.2 Current

The current velocity profiles for both LCs are calculated based on a combination of the wind-generated current and tidal current recommended by DNV [57]. Using a conservative approach, both current components are assumed to be in the same direction. For both LCs, the surface tidal current of 0.2 m/s is taken from the NORSOK standard [68]. The current velocity to depth variation is calculated based on the Power Law profile by the DNV standard [66]. The wind-generated current profiles down to -50 m still water reference depth are calculated based on the wind speed at 10 m height above SWL as recommended by DNV [57]. For the rated LC, the wind speed at the hub height of 106 m is scaled down to the wind speed at 10 m height based on the NPD spectrum. For the extreme LC, the wind speed at 10 m height is directly taken from Kvitrud and Løland [70]. For the rated LC and extreme LC, the calculated current profile at -5 m depth coincides with the mean and maximum value reported by Equinor for the Hywind Tampen location [49]. The totalled current profiles for both LCs are presented in Figure 3.4.

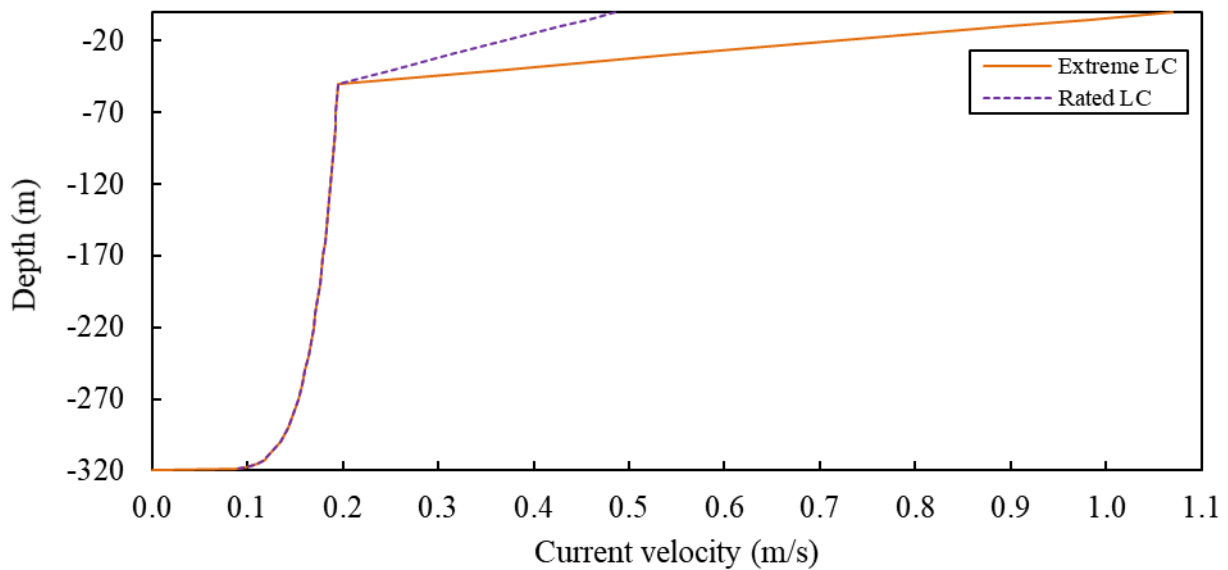


Figure 3.4: *Current profile in extreme LC and rated LC.*

3.1.3 Waves

The wave environmental data is specified by the JONSWAP spectrum. The rated wave condition is taken from the NREL report [69], and the respective wave frequency spectrum is shown in Figure 3.5. The wave data for the extreme LC are taken from the Visund field [70], and the corresponding wave frequency spectrum is shown in Figure 3.6. The peak enhancement factor γ for both cases is calculated based on DNV [67].

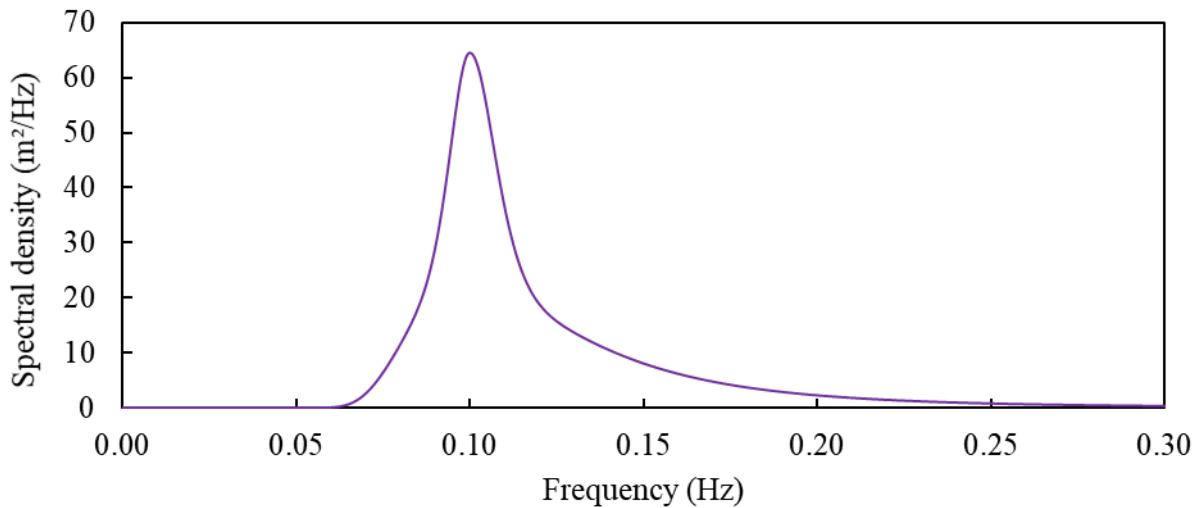


Figure 3.5: *Wave frequency spectrum for the rated LC.*

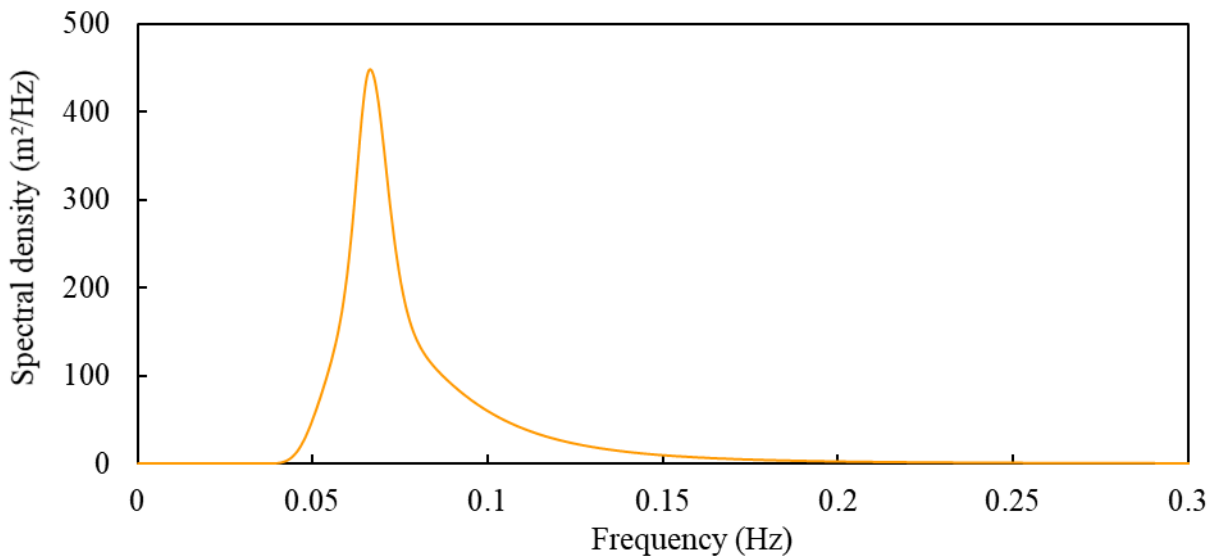


Figure 3.6: *Wave frequency spectrum for the extreme LC.*

3.1.4 Load Implementation in Analysis

The load directions are separately applied in three different directions, as summarised in Table 3.2 and Figure 3.7. The load angles are measured anti-clockwise from the global x-axis. The 0° angle indicates the load in the transverse direction to the cable. The 90° angle represents the load in line to the cable.

Table 3.2: Summary of the load directions.

Load angle	Description
0°	Wind, current, and wave direction are in transverse direction, i.e., perpendicular, to the cable. Nacelle and turbine face the direction of the wind.
45°	Wind, current, and wave direction are at 45° to the direction of the cable. Nacelle and turbine face the direction of the wind.
90°	Wind, current, and wave direction are inline and parallel with the direction of the cable. The nacelle and turbine face the direction of the wind.

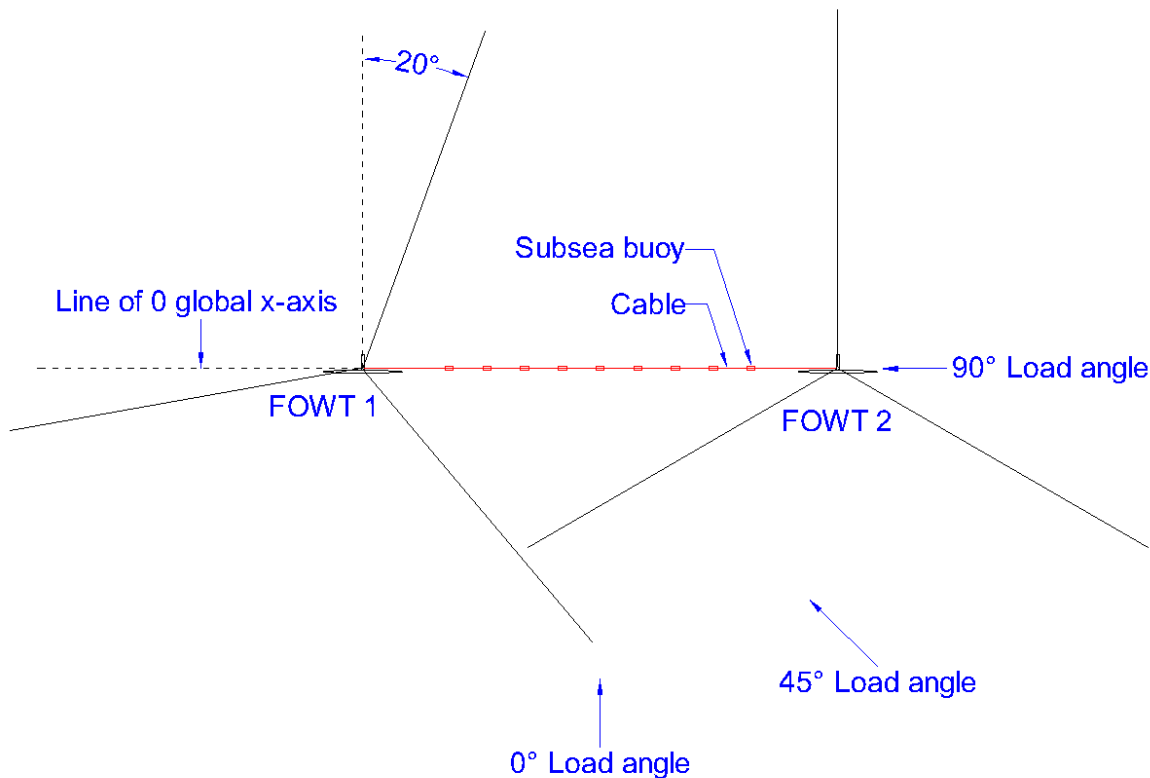


Figure 3.7: Plan view of the turbine mooring lines orientation and load angles.

3.2 Modelling of the OC3-Hywind FOWT in OrcaFlex

The spar-buoy type FOWT model used is the OC3-Hywind from the Offshore Code Comparison Collaborative (OC3) Phase IV Project [10,69]. This FOWT uses the 5 MW baseline wind turbine [11]. Both, OC3-Hywind and the turbine, are developed by the National Renewable Energy Laboratory (NREL). This FOWT is used here due to the extensive research in recent years, with sufficient data for comparison and validation [9,54,69,71]. The baseline OC3-Hywind geometry is shown in Figure 3.8. The top of the platform extends 10 m above SWL. The distance from SWL to COG is about 89.9 m when only platform and ballast are considered. The OC3-Hywind model for this study is built in the simulation software as described by Ross et al. [72], with refined modification as by Schnepf et al. [54]. The model considers drag loads at the turbine blades and the spar. Table 3.3 summarises the platform tower properties, and Table 3.5 describes the hydrodynamic and mooring system properties. Table 3.6 describes the details of the 5 MW turbine.

Table 3.3: *Floating platform structural properties [10].*

Depth to platform base below SWL (total draft)	120 m
Elevation to platform top (tower base) Above SWL	10 m
Depth to top of taper below SWL	4 m
Depth to bottom of taper below SWL	12 m
Platform diameter above taper	6.5 m
Platform diameter below taper	9.4 m
Platform mass, including ballast	7,466,330 kg
CM Location below SWL along platform centreline	89.9155 m
Platform roll inertia about CM	4,229,230,000 kg·m ²
Platform pitch inertia about CM	4,229,230,000 kg·m ²
Platform yaw inertia about platform centreline	164,230,000 kg·m ²

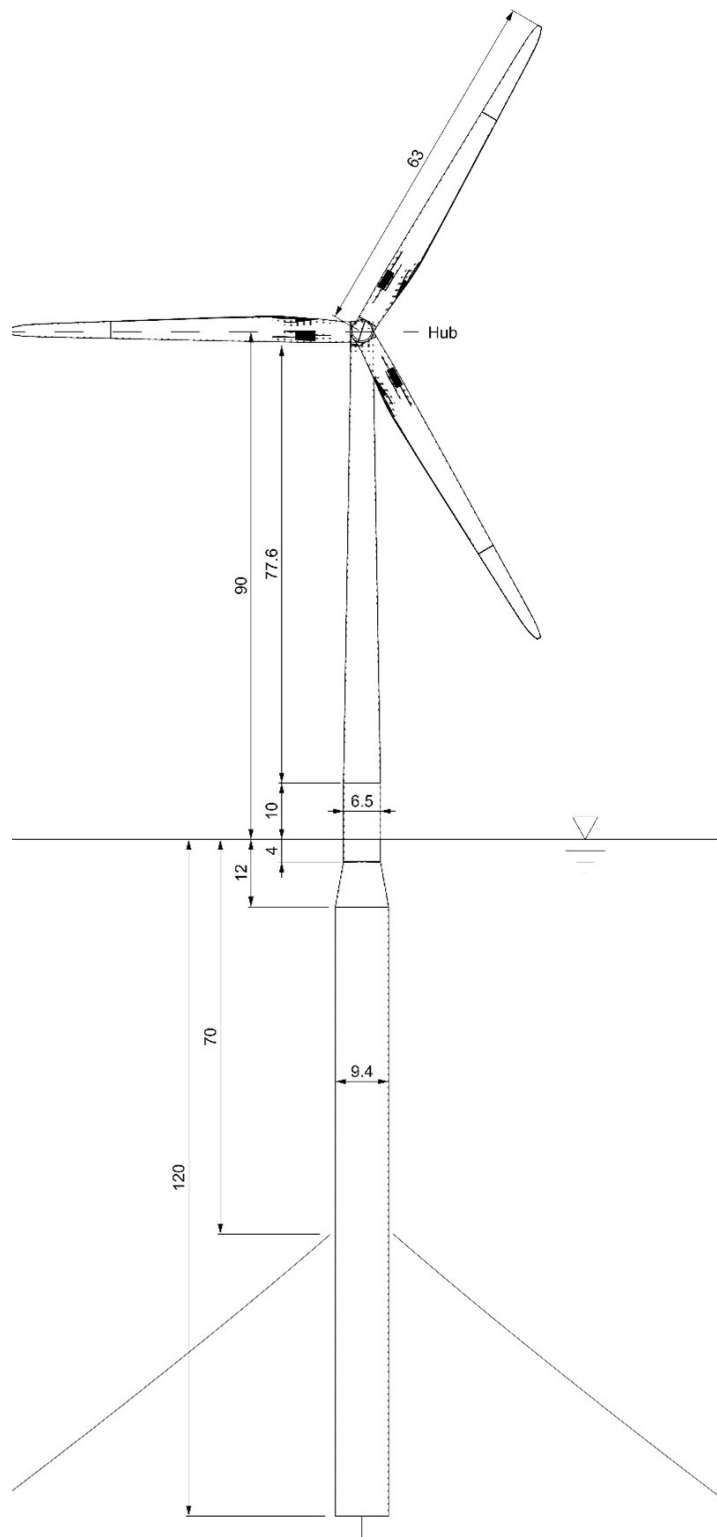


Figure 3.8: *Geometry of the OC3-Hywind FOWT (taken from [71]).*

3.2.1 Mooring Chains

Table 3.5 describes the hydrodynamic and mooring system properties. Line element object representation for the mooring chains is set to the analytic catenary type. This methodology is based on NREL approach [10] in their Fatigue Aerodynamics Structures & Turbulence (FAST) simulator, which considers a force-displacement relationship for each mooring chain. The same results are obtained in OrcaFlex using this approach [9]. This simplification disregards complex aspects such as bend stiffness, drag, and added mass. Nevertheless, simpler properties of a line element such as its weight, buoyancy, axial stiffness, and axial seabed friction are calculated. Therefore, the only calculated degrees of freedom in the system are those of the spar platform and the objects connected to it. This simplification means that a lookup table is calculated at the beginning of the simulation that relates mooring chain tension to the offset of the spar platform.

Table 3.4: *Mooring system properties [10].*

Number of mooring lines	3
Angle between adjacent lines	120 deg
Depth to anchors below SWL (water depth)	320 m
Depth to fairleads below SWL	70 m
Radius to anchors from platform centreline	853.87 m
Radius to fairleads from platform centreline	5.2 m
Unstretched mooring line length	902.2 kg
Mooring line diameter	0.09 m
Equivalent mooring line mass density	77.7066 kg/m
Equivalent mooring line weight in water	698.094 N/m
Equivalent mooring line extensional stiffness	384,243,000 N
Additional yaw spring stiffness	98,340,000 N·m/rad

3.2.2 Mooring Yaw Spring Stiffness

All existing spar FOWTs used the delta connection of the mooring line to the spar, as shown in Figure 3.9 (left). The purpose of the delta connection is to provide an element of mooring yaw stiffness to the system. The delta connection is eliminated to simplify the analysis of the mooring system within the OC3 project. This is shown in Figure 3.9 (right). The nominal mooring yaw spring stiffness is then introduced to the spar by connecting the spar to a pair of constraint objects in the simulation software. Using the individual DOFs, the necessary yaw spring rotational stiffness of 98,340 kN·m/rad, as shown in Table 3.5, is assigned to the constraint object named the “yaw_constraint”. This equates to 1,716.36 kN·m/deg. The connections between the 6D buoy object of the spar to the “yaw_constraint” and “fixed_constraint” objects are then configured to allow the yaw spring stiffness to be transferred to the floating system as shown in Figure 3.10.

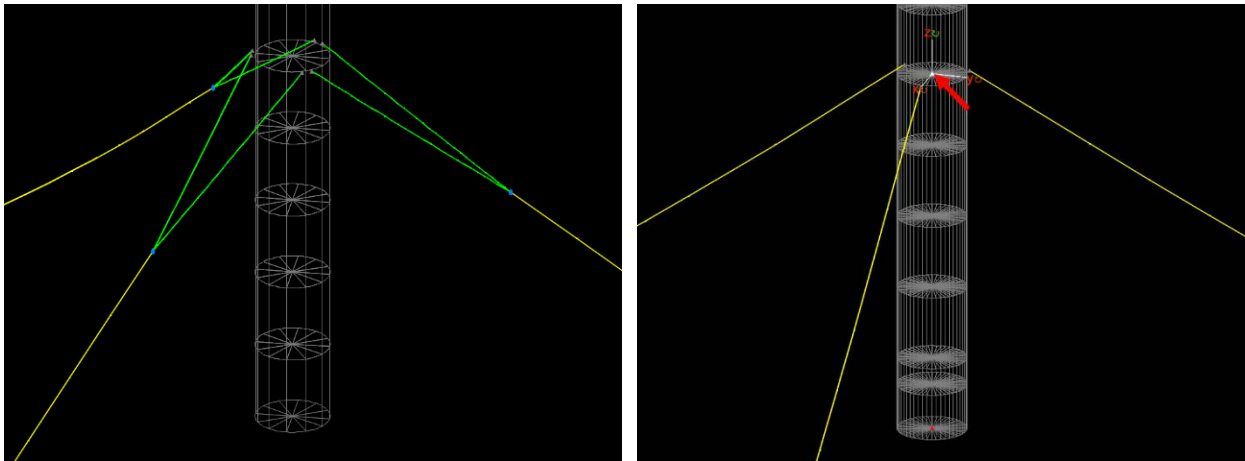


Figure 3.9: Delta connection (left) and location of “yaw_constraint” and “fixed_constraint” (right, red arrow) for mooring chains represented as an analytic catenary system.

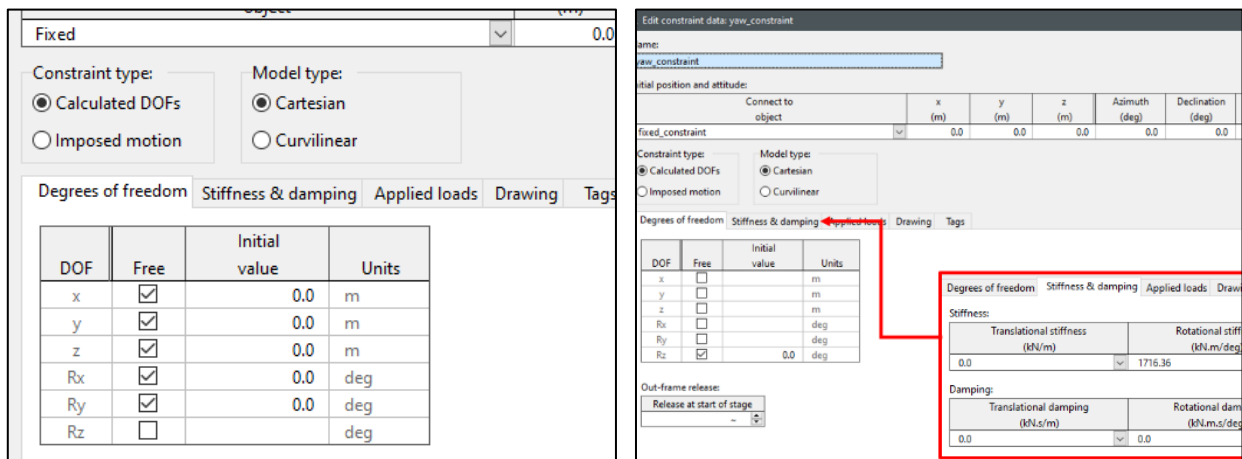


Figure 3.10: “fixed_constraint” (left) and “yaw_constraint” (right) in the simulation software.

3.2.3 Spar

The spar buoy is constructed using several cylinders of 6D buoys objects with outer diameters ranging from 6.5 m at 10 m height above SWL down to 4 m below SWL. The diameters of the tapered section increase linearly from 6.5 m at depths of 4 m below SWL to 9.4 m diameter at the 16 m depth. Then the 9.4 m outer diameter section continues until a depth of 120 m. The diameter variation at the tapered section is shown in Figure 3.11 (left).

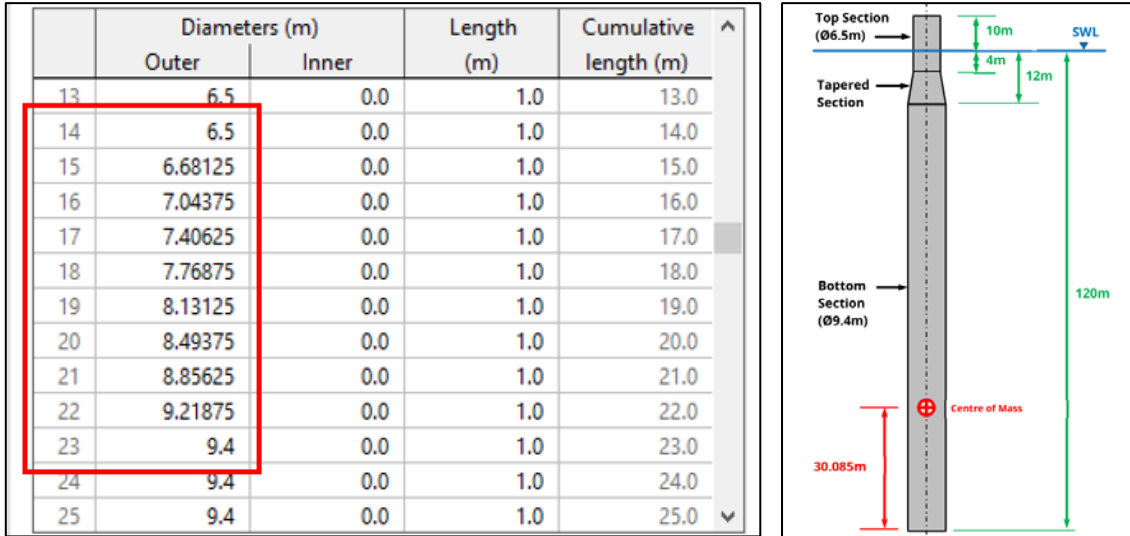


Figure 3.11: Variation in diameter at the tapered section (left) and the reference depth on the spar (right).

Instead of 40 discrete cylinders as done by Ross et al. [72], 41 stacked cylinders are used while retaining the same spar length. This is done by dividing the bottom-most cylinder object into 2 sections as shown in Figure 3.12 (left). Since OrcaFlex uses Morison's equation to calculate the hydrodynamic loads on the spar buoy [73], the latter cylindrical section is incorporated with the calculated added mass coefficient, C_a in the axial direction for three-dimensional bodies of a circular disc in infinite fluid based on the DNV recommended practice [57]. This is done to adjust the hydrodynamic heave forces damping by the spar platform due to wave excitation [10]. Added mass coefficients in the normal direction are applied based on the report by NREL [10]. Furthermore, another OrcaFlex vessel object named “damping_platform” is added and connected to the yaw_constraint. Figure 3.13 (left) shows the damping_platform is assigned with vessel type as “platform_type” where the additional linear damping in the surge, sway, heave, and yaw are accounted according to the values in Table 3.4. These values are added on top of the hydrodynamic loads to match the free-decay responses from the experimental test on Hywind Demo provided by Statoil [10].

Cylinders:	Diameters (m)		Length (m)	Added mass force coefficients (Ca)		f
	Outer	Inner		Normal	Axial	
	30	9.4		0.0	1.0	
31	9.4	0.0	10.0	0.96995	0.0	
32	9.4	0.0	10.0	0.96995	0.0	
33	9.4	0.0	10.0	0.96995	0.0	
34	9.4	0.0	10.0	0.96995	0.0	
35	9.4	0.0	10.0	0.96995	0.0	
36	9.4	0.0	10.0	0.96995	0.0	
37	9.4	0.0	10.0	0.96995	0.0	
38	9.4	0.0	10.0	0.96995	0.0	
39	9.4	0.0	10.0	0.96995	0.0	
40	9.4	0.0	3.73333	0.96995	0.0	
41	9.4	0.0	6.26667	0.96995	0.63662	

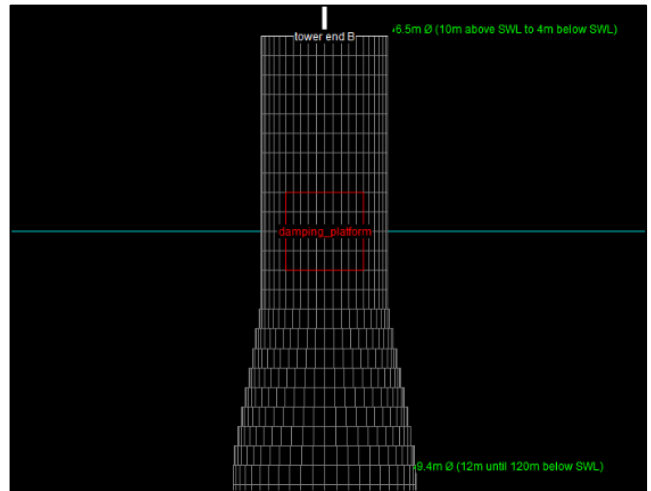


Figure 3.12: Added axial mass coefficient (left) and the location of the “damping_platform” object (right).

Surge	Sway	Heave	Roll	Pitch	Yaw
kN/(m/s)	kN/(m/s)	kN/(m/s)	(kN.m)/(rad/s)	(kN.m)/(rad/s)	(kN.m)/(rad/s)
100.0	100.0	130.0	0.0	0.0	13e3

Figure 3.13: Properties of “damping_platform” (left) and the assigned additional linear damping (right).

Table 3.5: Floating platform hydrodynamic properties [10].

Water density (ρ)	1,025 kg/m ³
Water depth (h)	320 m
Added-mass coefficient (C_A in Morison’s equation)	0.969954
Viscous-drag coefficient (C_D in Morison’s equation)	0.6
Additional linear damping in surge	100,000 N/(m/s)
Additional linear damping in sway	100,000 N/(m/s)
Additional linear damping in heave	130,000 N/(m/s)
Additional linear damping in yaw	13,000,000 Nm/(rad/s)

3.2.4 Nacelle

The nacelle is constructed using a 6D buoy object that is free. This means that the nacelle can move independently of other objects in response to the loads and the connection coordinates are the same as global coordinates. Drag loads are not considered on the nacelle. The center of mass of the nacelle is adjusted according to the global values given by Jonkman et al. [11].

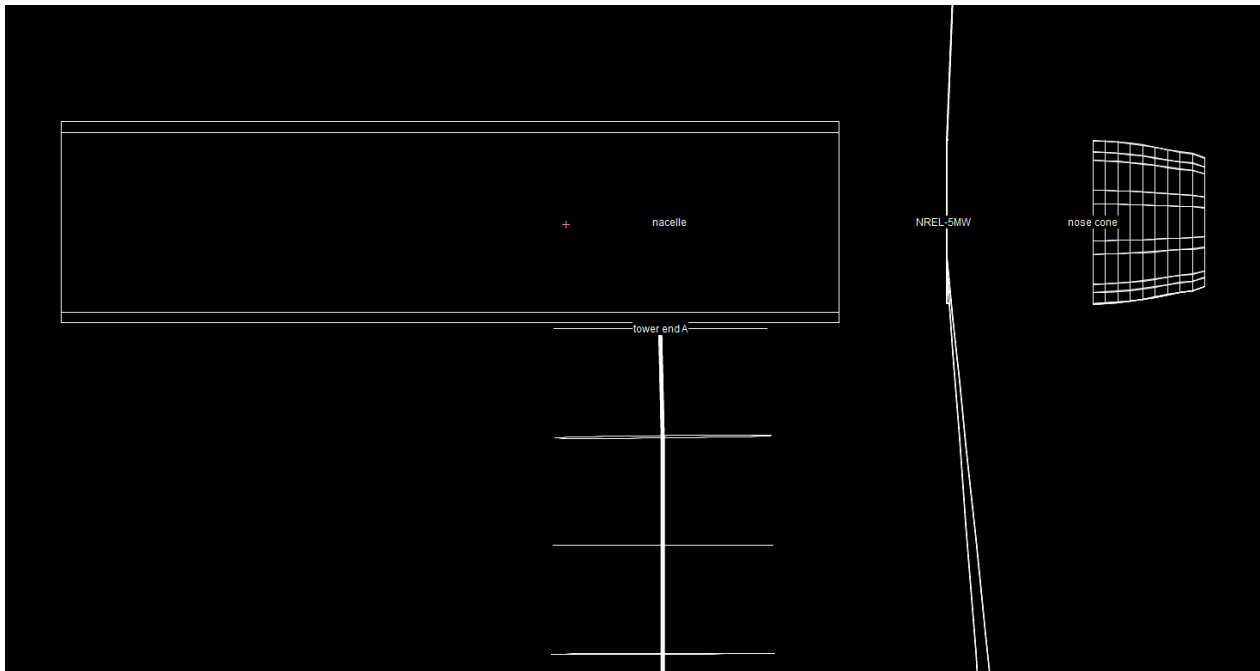


Figure 3.14: *Nacelle center of mass (CM).*

3.2.5 Turbine

The “NREL-5MW” turbine object is connected to the nacelle. Table 3.6 describes the details of the turbine. Three blades consisting of several sections are connected to the turbine as shown in Figure 3.15. The NREL FAST simulation approach only accounts for the bending stiffness of the turbine blades, whereas the torsion and axial stiffness DOFs of the turbine blades are neglected. However, these parameters are considered in the OrcaFlex model. The turbine object for OC3-Hywind used in study are taken directly from Ross et al. [72] and Schnepf et al. [9]. Ross et al. and Schnepf et al. have validated the turbine in their study. Figure 3.15 (left) is where the *PythonController.py* script obtained from Orcina [74] is attached to control the blade pitch during simulation. The turbine responses in OrcaFlex are validated by Schnepf et al. [9] to match the response in NREL FAST simulation.

Table 3.6: *Properties of NREL 5-MW baseline wind turbine [11].*

Rating	5 MW
Rotor orientation, Configuration	Upwind, 3 blades
Control	Variable speed, Collective pitch
Drivetrain	High speed, Multiple-stage gearbox
Rotor, Hub diameter	126 m, 3 m
Hub height	90 m
Cut-in, Rated, Cut-out wind speed	3 m/s, 11.4 m/s, 25 m/s
Cut-in, Rated Rotor speed	6.9 rpm, 12.1 rpm
Rated tip speed	80 m/s
Overhang, Shaft tilt, Precone	5 m, 5°, 2.5°
Rotor mass	110,000 kg
Nacelle mass	240,000 kg
Tower mass	347,460 kg
Coordinate location of overall CM	(-0.2 m, 0.0 m, 64.0 m)
Elevation to tower top (Yaw bearing) Above SWL	87.6 m

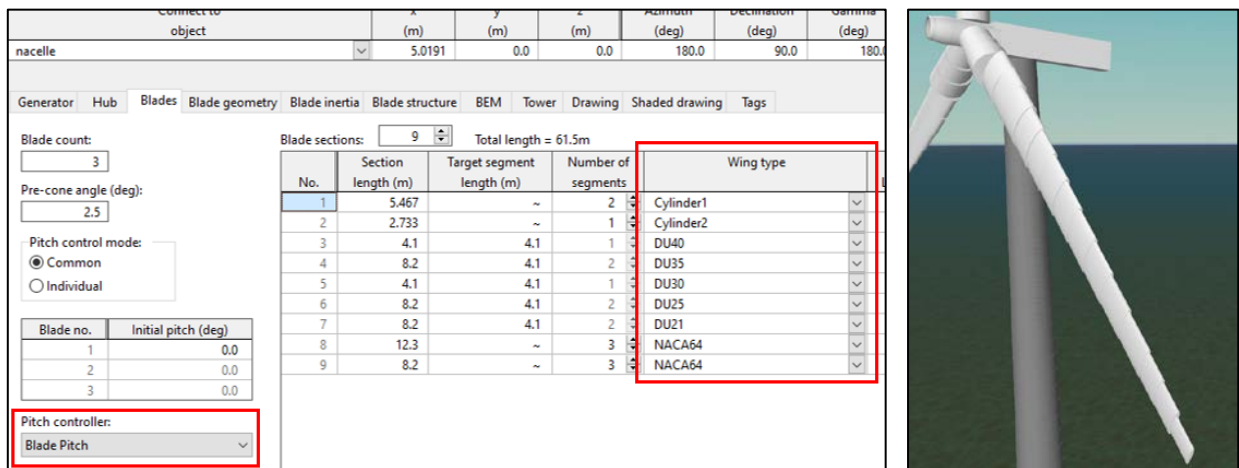


Figure 3.15: *Wing type and blade pitch controller.*

3.3 Suspended Inter-Array Power Cable Configuration

The general setup of a suspended cable configuration between the two FOWTs is shown in Figure 3.16. The buoy sizes, number of buoys, buoy spacings, and cable lengths of the configurations are varied. This section discusses the assigned properties and sensitivity analysis.

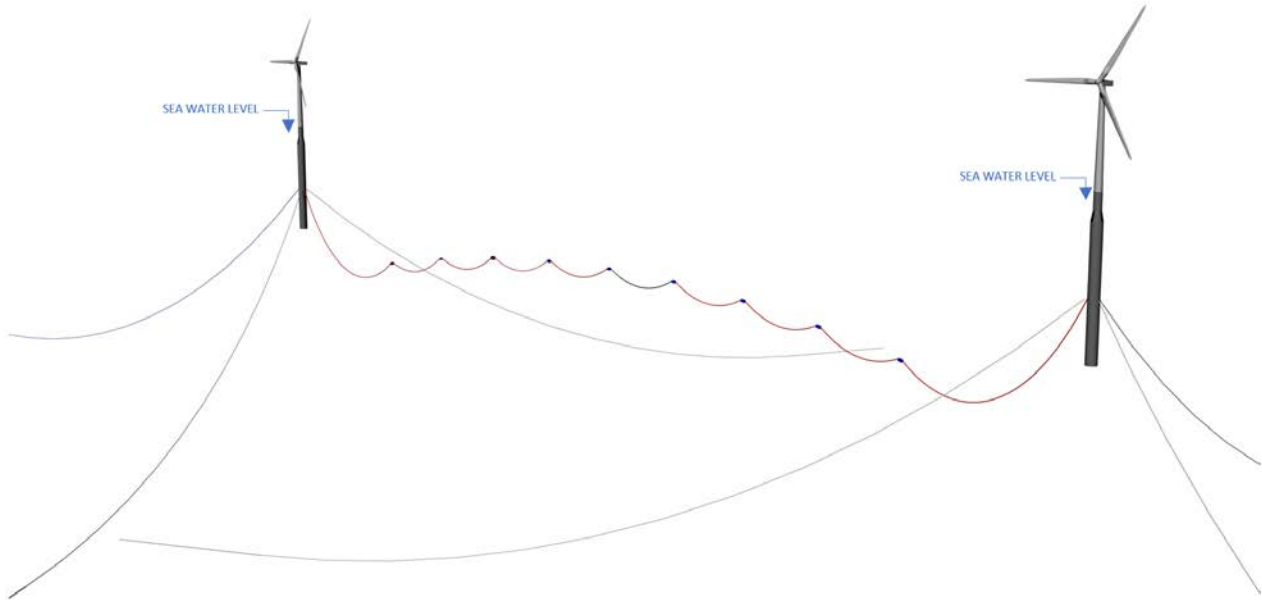


Figure 3.16: Example of a suspended inter-array cable configuration.

3.3.1 Distance Between Wind Turbines in a Wind Farm

The length of the inter-array power cable depends on the distance between the two FOWTs in the wind farm. The wake effect generally requires $4D$ to $9D$ for turbines in a row perpendicular to the prevailing wind and $6D$ to $12D$ to the back of the upstream turbine in a wind farm [23]. The distance between wind turbines in this study is adopted from the spacing used for Hywind Tampen [49] and Hywind Scotland [50], which is a distance of $9D$. This is equivalent to 1134 m for this 126 m rotor diameter OC3-Hywind turbine.

As for line clashing, the possibility of mooring chains and cable clashing can be observed in the plan view of the setup as shown in Figure 3.7. Table 3.5 describes the radius of the mooring chain anchor from the vertical centre on the FOWT as 853.87 m. Therefore, the minimum distance between the turbines without changing the orientation of the mooring chain is 1521.61 m. To avoid clashing of the mooring chain, 1134 m spacing is achieved by rotating the mooring chain of the second turbine to 20° clockwise.

3.3.2 Dynamic Power Cable

Subsea cables are designed to endure dynamic loadings in extreme offshore environments. Offshore wind farm inter-array cable systems are usually based on three-phase alternating current (AC) technology. Data on wind farm subsea cables are not commonly available, as the subsea cables are customised for a specific project. Therefore, the properties of the cables employed in this study are derived from several previous studies [40,41,75], as presented in Table 3.7.

Table 3.7: *Properties of the copper cable and the aluminium cable.*

Cable type		Aluminium cable	Copper cable
Outer diameter	m	0.179	0.150
Mass per unit length	kg/m	41.850	48.100
Bending stiffness	$kN \cdot m^2$	15.000	20.000
Axial stiffness	kN	300,000.000	700,000.000
Torsional stiffness	$kN \cdot m^2$	14.000	14.000
Drag coefficient (normal)	–	1.200	1.200
Added mass coefficient	–	1.000	1.000

The cable HOP is located 70 m below the SWL and at a 5.2 m radius from the platform centreline. Both types of cable have the same voltage rating at 66 kV. According to Grivas et al. [75], the copper cable is expected to be heavier than aluminium cable despite having a smaller diameter for the same voltage rating. This is due to the lower transmission capability of the aluminium cable. To transmit the same power as the copper cable, the aluminium cable has a larger diameter, leading to a larger cross-sectional area. Since this study will include the effect of marine growth (MG), cable properties stated in Table 3.7 are taken as the cable properties during start-of-life (SOL) in which marine growth is absent.

3.3.3 Cable Ancillaries

This section describes the ancillaries used for the suspended power cable configurations. Buoys provide buoyant force to lift the cable from the seabed. A similar exterior shape of a generic buoy which has common values available by the manufacturer [76] is taken from Schnepf et al. [54]. Two buoy sizes are used, buoy B1 and buoy B2. The detailed properties are presented in Table 3.8.

Table 3.8: *Properties of buoys without cable insertion.*

Buoy type		Buoy 1 (B1)	Buoy 2 (B2)
Length	m	2.940	2.170
Volume	m^3	12.471	8.615
Weight	t	4.600	2.700
Equivalent buoy outer diameter (cylinder shape)	m	2.324	2.248
Mass per unit length (without cable)	t/m	1.565	1.198
Mass per unit length (with aluminium cable)	t/m	1.606	1.240
Mass per unit length (with copper cable)	t/m	1.613	1.246
Drag coefficient (normal)	–	0.209	0.209
Drag coefficient (axial)	–	1.000	1.000
Added mass coefficient (normal)	–	0.459	0.459
Added mass coefficient (axial)	–	0.600	0.600

In this study, the buoy is proposed to be positioned horizontally for the power cable to run through the hollow tubular section of the buoy. Bend stiffeners are attached to both ends of the buoy, as seen in Figure 3.17.

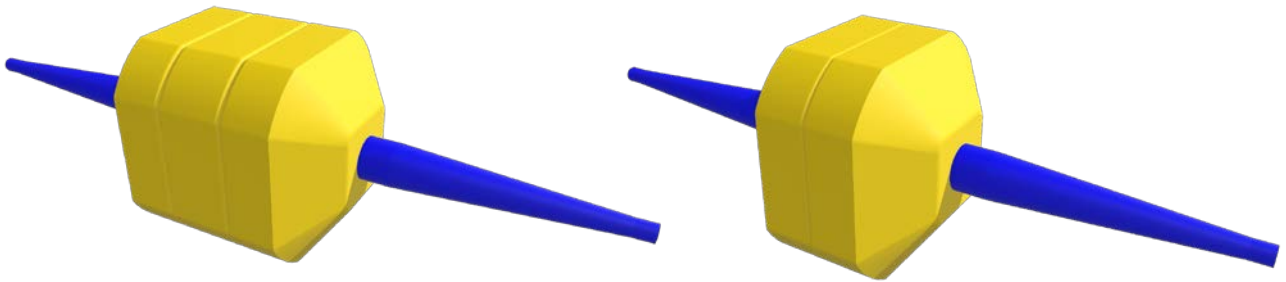


Figure 3.17: *Buoy B1 (left) and buoy B2 (right) with attached bend stiffeners.*

The shape of the buoys is assumed to be cylindrical during the simulation setup. By keeping the original volumes and lengths, equivalent diameters of the buoys are recalculated. Drag coefficient of the buoys obtained from the CFD simulation in Schnepf’s study [9] is used to simulate the unique

prism-like shape. High bending stiffness is assigned to the buoy to simulate a stiff buoy without any bending. The kinks on the buoy's body are also neglected and assumed to be smooth surfaces.

Since the buoy is inserted like a ring around the cable, respective mass per unit length of the buoy section configured for aluminium and copper cable are recalculated due to dissimilarity in mass per unit length of each cable type. The added mass and drag coefficient for the buoy remains the same for both cable types.

Manufacturers designed their cable to be able to bend down until a certain amount of bending radius limit. Therefore, less cable bending during operation is preferred. Bend stiffeners are used to prevent excessive bending of the cable. The properties of the bend stiffener are chosen based on Schnepf's study [9,54]. Detailed dimensions of the bend stiffener are described in Figure 3.18. The Young's modulus of the bend stiffener is defined by the stress-strain relationship, as shown in Figure 3.19.

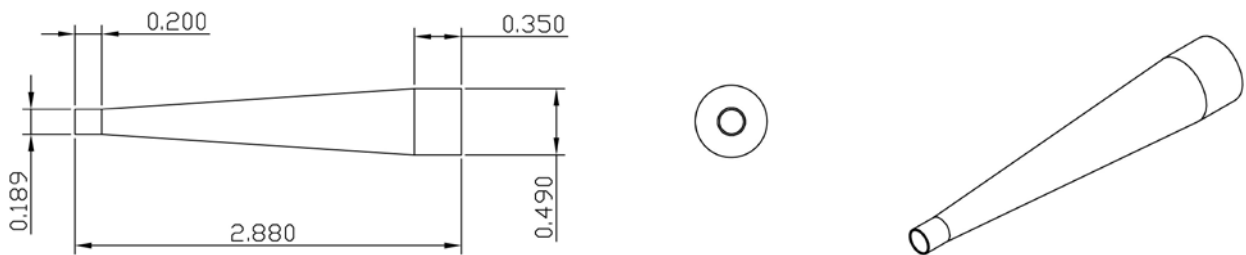


Figure 3.18: Bend stiffener dimension details (m).

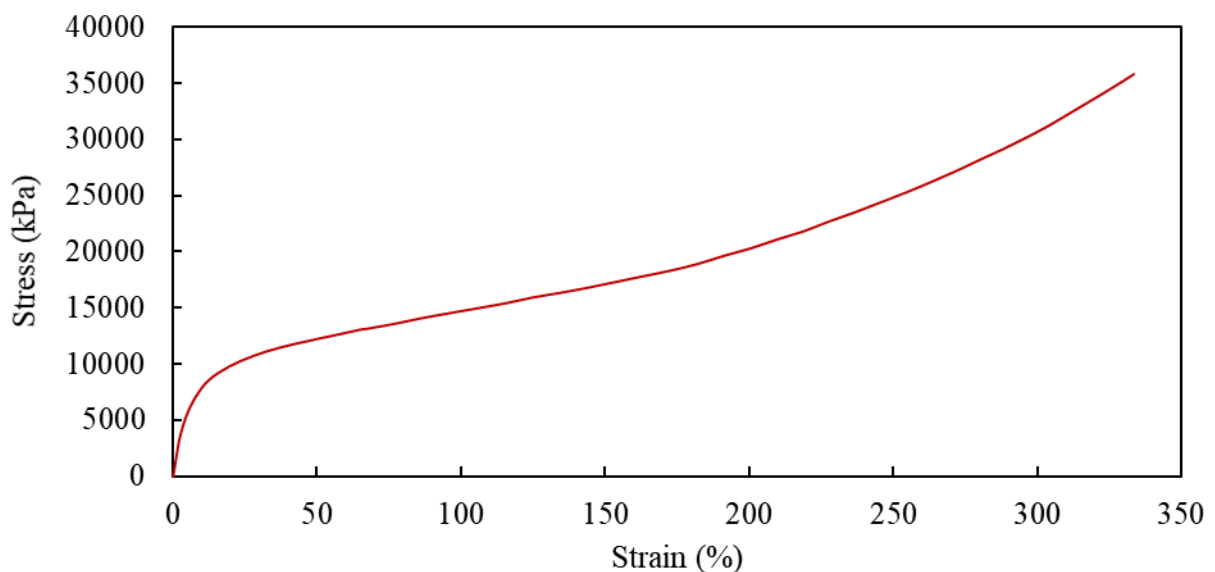


Figure 3.19: Stress-strain relationship of the bend stiffener.

3.3.4 Sensitivity Analysis

The cable is modelled using a line object represented by a finite element type. Therefore, sensitivity analysis for the discretisation lengths of the line segments and timestep of the simulation time is performed to increase the result accuracy and optimise the simulation runtime. The sensitivity analysis is done by checking the simulation runtime and the maximum effective tension for each discretisation length. The adequate accuracy for discretisation lengths is measured by checking the difference between the maximum effective tension of each discretisation length against the maximum effective tension of the smallest discretisation length. The difference should be smaller than 10^{-3} . For the time-step sensitivity analysis, it is found that 0.1 s of timestep is adequate.

There are four cable sections, and each cable section has different discretisation lengths. The four cable sections are HOP location, bend stiffener, buoy, and free-hanging section. Both HOP and bend stiffener are the critical cable sections to be modelled due to an extreme movement around these sections. Therefore, small discretisation lengths are used. For the HOP location, 0.05 m to 1.0 m of discretisation length are tested with 0.05 m stepwise. It was found that 0.3 m discretisation length is adequate to study the cable at the HOP location. At the bend stiffener, 0.06 m to 0.36 m lengths are tested with 0.06 m stepwise. It was found that 0.12 m is adequate.

The buoys sections are expected to be stiff. Therefore, this section can be modelled using large discretisation. However, it is advised not to differ the discretisation length to the neighbouring section significantly. Discretisation lengths of 0.21 m are used for buoy B1, and 0.31 m discretisation are used for buoy B2.

Free-hanging section is the least critical part. Similar to the buoy section, it is advised not to differ the discretisation length from the neighbouring section significantly. Therefore, the discretisation length of the free-hanging sections of the cable is taken at 1 m.

3.4 Effect of Marine Growth

The change in cable weight, diameter, and drag coefficient due to marine growth are called End-of-Life (EOL) state, and the cable properties without the marine growth effect are called Start-of-Life (SOL) state. The cases in the EOL state are generated using the Python script in Appendix A. The added weight and change of drag coefficient around the buoy and bend stiffener are not considered throughout the design life by assuming that each buoy and bend stiffener are coated with an anti-marine growth coating.

Due to the W-shape of the suspended cable configuration, different parts of the cable section will settle at different depths for which the marine growth develops with different thicknesses and densities as stated in Table 3.9. Only cables that are below -50 m depths are referred from NORSOK [68]. The NORSOK standard also stated that cold-water coral is assumed not to occur at depths below -100 m in the Norwegian Sea. The cable sections that settle below the -100 m are assigned with SOL line element properties.

The summarised values of surface roughness k , thickness t , and density of the marine growth ρ_{mg} in Table 3.9 are used to recalculate the EOL properties of each cable type in each loading condition and depth range according to NORSOK [68].

Table 3.9: *Depth range and calculation parameters for marine growth effect.*

Depth (m)	EOL Level	Roughness, k	t (mm)	ρ_{mg} (kg/m^3)
-60 to -50	EOL1	2×10^{-2}	30	1100
-100 to -60	EOL2	2×10^{-2}	20	1100
Below -100	SOL	2×10^{-2}	10	1100

The calculated EOL properties for the aluminium cable are summarised in Table 3.10, and the EOL properties for the copper cable are summarised in Table 3.11. The EOL model for both cable types is constructed based on the steady-state result of the SOL model by assigning the specific EOL line element properties depending on the depth of each node on the cable.

Table 3.10: *EOL properties of the aluminium cable.*

EOL level	Outer diameter (m)	Mass per unit length (kg/m)	Drag coefficient			
			Rated LC		Extreme LC	
			Axial	Normal	Axial	Normal
EOL1	0.239	63.52	0.883	0.548	1.365	1.171
EOL2	0.219	55.60	0.938	0.572	1.344	1.252
SOL	0.179	41.85	1.200	0.008	1.200	0.008

Table 3.11: *EOL properties of the copper cable.*

EOL level	Outer diameter (m)	Mass per unit length (kg/m)	Drag coefficient			
			Rated LC		Extreme LC	
			Axial	Normal	Axial	Normal
EOL1	0.210	66.76	0.967	0.585	1.355	1.294
EOL2	0.190	59.85	1.039	0.617	1.281	1.401
SOL	0.150	48.10	1.200	0.008	1.200	0.008

3.5 Case Study Procedure

A base case for each buoy type is build manually for both cable types. The rest of the cases are automatically build using Python scripts. The overall process of this study is shown in Figure 3.20, and the “End” in the green circle is the main goal.

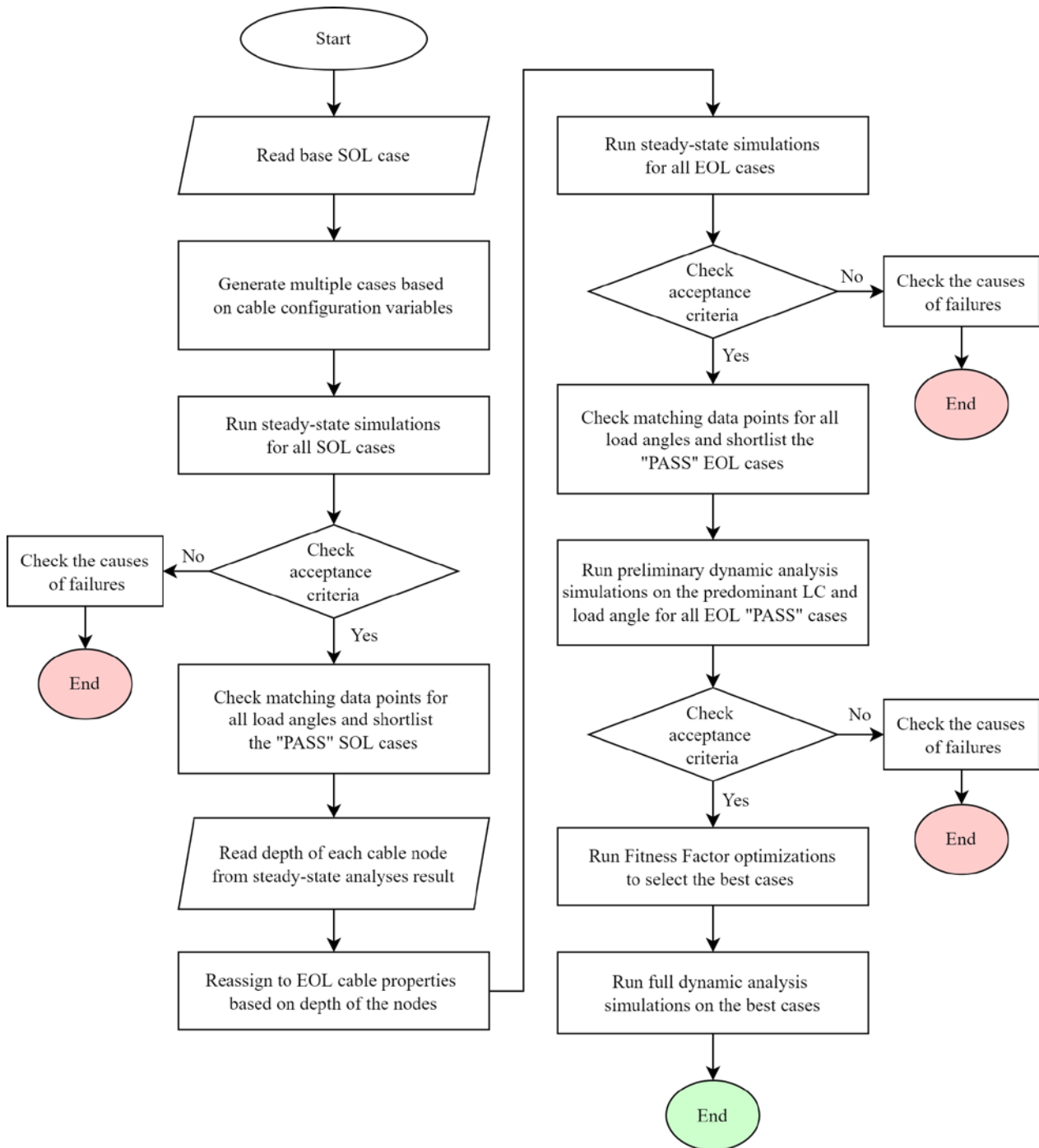


Figure 3.20: Overview of the flow diagram in the analysis process.

3.5.1 Case Study Variables

Different variables are tested for aluminium and copper cables due to the difference in mass per unit length of each cable type and the difference in the buoyancy of buoy B1 and buoy B2. The variables are the cable lengths, the number of buoys, and the spacings between the buoys. According to these variables, multiple cases are generated from the base case using a Python script in Appendix B. The minimum cable length is taken at 1200 m. More buoys are tested in copper cable than in aluminium cable due to the heavier mass per unit length of the copper cable. The spacings between the buoys for the copper cable are also taken at a smaller range compared to the aluminium cable for the same reason. Figure 3.21 explains the naming convention of the case used in the proceeding sections. The full cable configuration variables for buoys B1 and B2 are presented in Table 3.12 and Table 3.13 respectively.

Table 3.12: Cable configuration variables tested for buoy B1.

Cable type		Aluminium cable	Copper cable
Total cable length	m	1200 – 1400	1200 – 1400
Cable length step significance	m	20	20
Number of buoys		2, 3, 4, 5	4, 5, 6, 7
Spacing between buoy	m	220 – 400	100 – 300
Spacing length step significance	m	20	20

Table 3.13: Cable configuration variables tested for buoy B2.

Cable type		Aluminium cable	Copper cable
Total cable length	m	1200 – 1400	1200 – 1400
Cable length step significance	m	20	20
Number of buoys		3, 4, 5, 6	7, 8, 9, 10
Spacing between buoy	m	120 – 300	20 – 200
Spacing length step significance	m	20	20

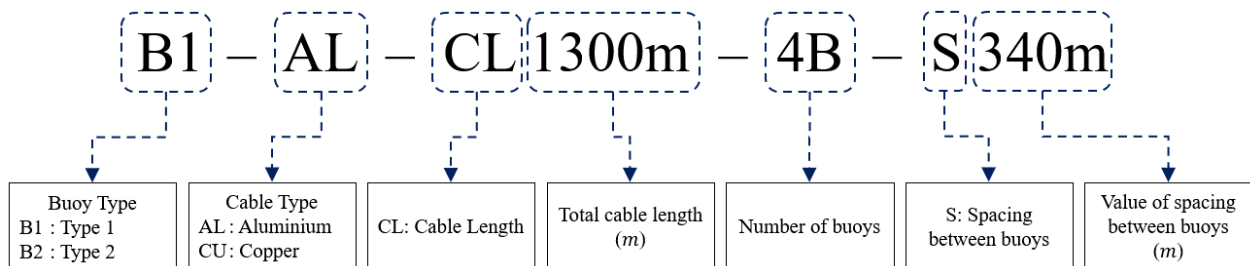


Figure 3.21: Case naming convention.

3.5.2 Acceptance Criteria

The acceptance criteria for copper cable and aluminium cable analyses are described in Table 3.14. Referring to the study done by Schnepf et al. [54], the maximum effective tension of the cable in dynamic analysis increased up to 24% from the steady-state analysis. Therefore, to increase the efficiency of this study, stricter minimum breaking load (MBL) criteria are implemented in the steady-state analysis, and the acceptance criteria in the dynamic analysis are increased by 24% from the steady-state. The 50 m clearance distance to the sea surface is taken to avoid collisions, disturbance to ship movement, maintenance activity, and minimises the influence of wind-generated current on the cable. A 10 m minimum gap to the seabed is taken to prevent the effects of near-wall proximity [77]. It is also to avoid damage when in contact with the seabed and consequently prevents more marine growth.

Table 3.14: *Acceptance criteria for steady-state and dynamic analysis of the cable configuration.*

Cable type	Aluminium	Copper
Minimum bend radius (MBR)		2.6 m
Minimum breaking load (MBL) in dynamic analysis	69 kN	96 kN
Minimum breaking load (MBL) in steady-state analysis	52 kN	72 kN
Minimum sea surface clearance		50 m
Minimum seabed clearance		10 m

3.5.3 Dynamic Simulation Evaluation and Optimisation Method

The maximum effective tensions and MBRs of the cable configurations that undergoes dynamic analysis study are assessed. Both criteria are normalised by their maximum permissible value as shown in Table 3.14 and merged into an optimisation criterion called "Fitness Factor". The Fitness Factor is adapted from a study by Rentschler et al. [41], which was used to evaluate lazy wave configurations. The "Normalised MBR" for both cable types are described by Equation (3.1). For the aluminium cable, the "Normalised MBL" is described by Equation (3.2). Whereas for the copper cable, the Normalised MBL is described by Equation (3.3). The combined normalised value of MBR and MBL are described as the Fitness Factor in Equation (3.4).

$$\text{Normalised MBR} = \frac{2.6 \text{ m}}{\text{MBR}} \quad (3.1)$$

$$\text{Normalised MBL} = \frac{\text{Maximum Effective Tension}}{69 \text{ kN}} \quad (3.2)$$

$$\text{Normalised MBL} = \frac{\text{Maximum Effective Tension}}{96 \text{ kN}} \quad (3.3)$$

$$\text{Fitness Factor} = \text{Normalised MBL} + \text{Normalised MBR} \quad (3.4)$$

The maximum acceptable value for both Normalised MBL and Normalised MBR is equal to 1 each. Thus, the maximum tolerable value for the Fitness Factor is 2. The ideal case would have the Fitness Factor closest to zero.

4 RESULTS AND DISCUSSION

This chapter presents the findings of the steady-state and dynamic analysis carried out in this study. The results are presented in the same flow as the case study procedure in Section 3.5. The steady-state analysis is done in two marine growth stages: SOL state, and EOL state. As per the case study procedure, dynamic analysis is done in two stages to select the most optimized configurations. Preliminary dynamic analysis is done first, followed by full dynamic analysis.

4.1 Steady-State Analysis

Steady-state analysis is carried out to obtain the power cable behaviour when a constant wind and current velocity profile are applied to the system. The steady-state simulations are run at three different load angles. A total of 4725 case in the SOL state are generated from the base case file according to the variables in Table 3.12 and Table 3.13 in Section 3.5.1 above. Steady-state analysis is performed for 618 cases in the EOL state. The results are checked against the acceptance criteria in Table 3.14. The cases that meet all four acceptance criteria will be called “PASS” cases. Matching configuration case refers to the cases of the same configuration variables but tested in three different load angles. The matching configuration case of the PASS SOL cases are extracted and then re-analysed in the EOL state. The causes of failure are determined for both, SOL and EOL, states. Table 4.1 and Table 4.2 summarise the results for the aluminium cable configurations using buoy B1 and buoy B2. Table 4.3 and Table 4.4 summarise the results for the copper cable configurations using buoy B1 and buoy B2 respectively.

Table 4.1: *Steady-state analysis summary for aluminium cable configurations with buoy B1.*

Marine growth state	Load angle (deg)	Total tested case	Number of PASS case	Causes of failure			
				MBL (> 52 kN)	MBR (< 2.6 m)	Surface clearance (> -50 m)	Seabed clearance (< 10 m)
SOL	0°	427	34	133	144	231	10
	45°	427	30	134	147	232	10
	90°	427	30	135	160	232	10
EOL	0°	30	29	1	0	0	0
	45°	30	29	1	0	0	0
	90°	30	29	1	0	0	0

Table 4.2: *Steady-state analysis summary for aluminium cable configurations with buoy B2.*

Marine growth state	Load angle (deg)	Total tested case	Number of PASS case	Causes of failure			
				MBL (> 52 kN)	MBR (< 2.6 m)	Surface clearance (> -50 m)	Seabed clearance (< 10 m)
SOL	0°	404	102	131	42	114	83
	45°	404	101	131	47	114	83
	90°	404	100	138	59	114	83
EOL	0°	100	100	0	0	0	0
	45°	100	99	1	0	0	0
	90°	100	96	3	1	0	0

Table 4.3: *Steady-state analysis summary for copper cable configurations with buoy B1.*

Marine growth state	Load angle (deg)	Total tested case	Number of PASS case	Causes of failure			
				MBL (> 52 kN)	MBR (< 2.6 m)	Surface clearance (> -50 m)	Seabed clearance (< 10 m)
SOL	0°	392	46	249	10	119	102
	45°	392	44	254	14	119	102
	90°	392	43	257	20	120	102
EOL	0°	43	43	0	0	0	0
	45°	43	43	0	0	0	0
	90°	43	43	0	0	0	0

Table 4.4: *Steady-state analysis summary for copper cable on buoy B2.*

Marine growth state	Load angle (deg)	Total tested case	Number of PASS case	Causes of failure			
				MBL (> 52 kN)	MBR (< 2.6 m)	Surface clearance (> -50 m)	Seabed clearance (< 10 m)
SOL	0°	352	33	273	0	138	92
	45°	352	33	273	0	138	93
	90°	352	33	273	0	138	93
EOL	0°	33	33	0	0	0	0
	45°	33	33	0	0	0	0
	90°	33	33	0	0	0	0

The aluminium cable configurations in the SOL state have lesser PASS cases with buoy B1 than buoy B2. Less PASS cases in the buoy B1 configuration are caused by the high buoyant force of the large buoy, coupled with the lightweight aluminium cable making it difficult to balance the ratio between the buoyant force of the buoys and the weight of the cable. Most cases failed when using buoy B1 due to exceeding the sea surface clearance limit in the 4 buoys and 5 buoys configuration. Configurations with only 2 buoys of type buoy B1 seem insufficient, resulting in a large spacing between the buoys. The large spacing leads to a long unsupported hanging cable

between the buoys, causing MBL criterion exceedance. More number of PASS cases in aluminium cable configurations using buoy B2 is due to the smaller size of buoy B2. The small buoy B2 size allows the ratio of the total buoy's buoyant force and the total weight of the cable to be adjusted while keeping smaller buoy spacings. Configurations with 4 buoys of type B2 resulted in the most SOL PASS cases. As the number of buoys in the setup increases, the number of PASS cases decreases.

The critical failure driver for copper cable configurations in the SOL state is MBL exceedance. This can be attributed to the heavier weight of the copper cable, which causes a larger downward resultant force of the cable. Copper cable configurations are least likely to fail by MBR exceedance. This is expected as more buoys are required to keep the heavy copper cable afloat, resulting in shorter buoy spacings and flatter sagging shapes than aluminium cable configuration. For copper cable configurations using buoy B1 in the SOL state, 4 buoys are too few to keep the cable afloat above the seabed clearance limit. On the other hand, 7 buoys are too much and cause the cable to float to the sea surface. The best configurations have 5 or 6 buoys. For copper cable configurations using buoy B2 in the SOL state, 7 buoys are too few to keep the cable afloat above the seabed clearance limit. The best configurations have 9 buoys.

The spacing between buoys and the total cable length need to be optimised once the optimal number of buoys are selected. The spacing between buoys determines the cable behaviour in the middle section, while the total cable length determines the cable behaviour between the HOPs and the first buoys. The most optimum spacing and cable length must be selected to lower the maximum effective tension and increase the MBR while keeping the lowest possible maximum horizontal excursion. It is also to keep the cable steady at a certain depth in the current. Figure 4.1, Figure 4.2, and Figure 4.3 show the maximum effective tension, MBR, and maximum horizontal excursion variations with cable lengths and spacings for the configurations with buoy B1. Figure 4.4, Figure 4.5, and Figure 4.6 show the maximum effective tension, MBR, and maximum horizontal excursion variations with cable lengths and spacings for configurations with buoy B2. The optimum spacing for copper cable configurations using buoy B1 is around 180 m, while the optimal spacing for buoy B2 is approximately 100 m. The optimal spacing for buoy B1 on aluminium cable configurations is about 320 m, and the optimal spacing for buoy B2 on aluminium cable configurations is approximately 200 m.

CL (m)	S (m)										
	200	220	240	260	280	300	320	340	360	380	400
1200	57.4	54.9	52.8	51.0	49.6	46.8	43.7	44.0	46.7	50.1	54.0
1220	54.0	51.7	49.7	47.9	46.4	43.8	40.6	41.0	43.7	46.9	50.6
1240	51.9	49.6	47.7	45.9	44.4	41.5	38.4	38.9	41.6	44.8	48.3
1260	50.4	48.2	46.3	44.5	43.0	39.9	36.8	37.4	40.2	43.2	46.7
1280	49.3	47.2	45.3	43.6	42.0	38.5	35.6	36.3	39.0	42.1	45.4
1300	48.9	46.5	44.6	42.9	41.1	37.5	34.7	35.4	38.2	41.2	44.5
1320	48.8	46.1	44.2	42.4	40.1	36.7	35.1	35.1	37.5	40.5	43.8
1340	48.8	45.9	43.9	42.1	39.3	36.1	35.7	35.8	37.0	40.0	43.2
1360	49.0	46.0	43.7	41.9	38.7	36.7	36.6	36.6	36.8	39.5	42.7
1380	49.2	46.3	43.6	41.8	38.2	37.6	37.5	37.6	37.7	39.1	42.3
1400	49.6	46.6	43.7	41.3	38.9	38.7	38.6	38.6	38.7	39.0	41.9

CL (m)	S (m)										
	100	120	140	160	180	200	220	240	260	280	300
1200	105.6	91.9	74.1	67.8	66.6	70.2	81.0	99.9	119.0	138.3	
1220	100.1	87.3	72.0	67.0	66.0	68.9	76.9	94.7	112.6	130.5	
1240	96.7	84.4	71.3	67.3	66.5	68.9	74.1	91.3	108.3	125.2	
1260	94.5	82.6	71.6	68.3	67.6	69.6	74.0	88.8	105.2	121.3	137.4
1280	93.0	81.0	72.5	69.7	69.1	70.9	74.6	87.0	99.6	112.6	126.8
1300	92.1	79.5	73.9	71.4	71.0	72.5	75.7	78.9	89.5	101.2	113.8
1320	91.6	79.5	75.6	73.4	73.0	74.3	74.5	73.4	83.8	94.9	106.5
1340	91.3	80.8	77.5	75.5	75.2	76.4	73.7	71.1	80.0	90.8	101.8
1360	91.3	82.5	79.5	77.8	77.5	78.5	73.9	71.1	77.1	87.7	98.5
1380	91.2	84.4	81.7	80.2	79.9	79.3	74.6	71.7	74.9	85.4	95.9
1400	90.4	86.4	84.0	82.6	82.4	80.4	75.7	72.7	73.0	83.4	93.9

Figure 4.1: Maximum effective tensions for aluminium cable configurations using 3 buoys of type B1 (left) and copper cable configurations with 5 buoy of type B1 (right) at 90° load angle in the SOL state.

CL (m)	S (m)										
	200	220	240	260	280	300	320	340	360	380	400
1200	4.4	4.2	4.1	4.0	3.9	3.9	3.9	3.9	3.8	4.0	4.2
1220	3.9	3.7	3.6	3.5	3.5	3.4	3.5	3.5	3.4	3.5	3.7
1240	3.5	3.4	3.2	3.2	3.1	3.1	3.3	3.2	3.1	3.2	3.3
1260	3.2	3.1	3.0	2.9	2.9	2.9	3.1	3.0	2.9	2.9	3.0
1280	3.0	2.9	2.8	2.8	2.7	2.8	2.9	2.8	2.8	2.8	2.8
1300	2.9	2.8	2.7	2.6	2.6	2.7	2.8	2.7	2.6	2.6	2.7
1320	2.8	2.6	2.6	2.5	2.5	2.6	2.7	2.6	2.5	2.5	2.6
1340	2.7	2.6	2.5	2.4	2.4	2.5	2.6	2.6	2.4	2.4	2.5
1360	2.6	2.5	2.4	2.3	2.3	2.4	2.6	2.5	2.4	2.3	2.4
1380	2.5	2.4	2.3	2.3	2.3	2.4	2.5	2.4	2.3	2.3	2.3
1400	2.5	2.4	2.3	2.2	2.2	2.3	2.5	2.4	2.3	2.2	2.3

CL (m)	S (m)										
	100	120	140	160	180	200	220	240	260	280	300
1200	8.5	7.5	6.3	5.5	5.2	5.7	6.8	8.1	8.5	8.9	
1220	7.8	6.8	5.7	5.0	4.8	5.2	6.2	7.4	8.1	8.5	
1240	7.2	6.4	5.3	4.6	4.4	4.8	5.7	6.9	7.8	8.1	
1260	6.8	6.0	4.9	4.4	4.2	4.5	5.4	6.5	7.4	7.8	8.2
1280	6.5	5.6	4.7	4.2	4.0	4.3	5.1	6.1	6.8	7.3	7.7
1300	6.2	5.3	4.4	4.0	3.9	4.1	4.9	5.0	5.2	5.6	6.3
1320	6.0	5.1	4.3	3.9	3.8	4.0	4.3	4.2	4.3	4.6	5.0
1340	5.8	4.9	4.1	3.8	3.7	3.9	3.8	3.7	3.8	3.9	4.2
1360	5.6	4.8	4.0	3.7	3.6	3.7	3.5	3.4	3.5	3.6	3.8
1380	5.3	4.6	3.9	3.6	3.5	3.4	3.2	3.3	3.3	3.4	3.5
1400	5.2	4.5	3.8	3.5	3.4	3.2	3.0	3.1	3.2	3.2	3.3

Figure 4.2: MBR for aluminium cable configurations using 3 buoys of type B1 (left) and copper cable configurations with 5 buoys of type B1 (right) at 90° load angle in the SOL state.

CL (m)	S (m)										
	200	220	240	260	280	300	320	340	360	380	400
1200	41.1	41.5	41.0	39.8	37.8	29.0	22.5	20.8	19.8	18.4	16.8
1220	44.5	44.7	43.9	42.4	40.5	31.9	25.0	23.5	22.3	20.8	19.0
1240	47.0	46.9	45.8	44.1	43.0	33.5	27.1	26.0	24.6	22.9	20.9
1260	48.7	48.3	47.0	45.7	45.1	34.3	29.0	28.1	26.6	24.8	22.6
1280	49.8	49.2	47.7	47.2	47.0	34.7	31.1	30.1	28.4	26.4	24.0
1300	50.5	49.6	48.7	48.6	46.3	35.2	32.9	31.7	30.0	27.8	25.2
1320	50.9	49.8	49.6	49.9	44.6	35.9	34.5	33.2	31.3	28.9	26.2
1340	51.0	50.3	50.6	51.1	43.1	36.7	35.9	34.5	32.4	29.9	26.8
1360	51.0	50.9	51.6	52.4	42.2	37.9	37.1	35.5	33.3	30.5	27.3
1380	51.1	51.7	52.7	52.7	41.6	39.1	38.1	36.5	34.1	31.0	27.3
1400	51.6	52.6	53.9	50.0	41.3	40.1	39.0	37.2	34.6	31.2	27.0

CL (m)	S (m)										
	100	120	140	160	180	200	220	240	260	280	300
1200	20.1	22.1	15.2	13.1	12.7	10.8	8.7	7.1	5.9	5.1	
1220	21.7	23.8	15.4	14.3	13.8	11.6	9.3	7.5	6.3	5.4	
1240	23.0	25.2	15.3	15.3	14.6	12.2	9.6	7.8	6.5	5.6	
1260	24.0	26.2	15.6	16.1	15.3	12.6	9.8	7.8	6.4	5.5	4.8
1280	24.9	25.8	16.0	16.9	15.9	12.8	9.7	7.3	10.7	14.8	15.4
1300	25.5	24.3	16.5	17.5	16.3	12.9	9.1	24.1	36.7	42.7	44.4
1320	26.0	22.4	17.1	18.0	16.5	12.7	20.2	43.7	58.6	66.5	69.5
1340	26.5	20.4	17.6	18.4	16.7	12.3	34.8	61.0	77.8	87.2	91.5
1360	26.8	18.5	18.0	18.7	16.7	11.0	48.3	76.6	95.1	105.8	111.2
1380	26.3	17.8	18.4	18.9	16.6	20.9	60.8	91.1	111.0	122.7	129.1
1400	23.8	17.5	18.7	19.1	16.4	30.5	72.6	104.6	125.8	138.5	145.7

Figure 4.3: Maximum horizontal excursions for aluminium cable configurations using 3 buoys of type B1 (left) and copper cable configurations with 5 buoys of type B1 (right) at 90° load angle in the SOL state.

CL (m)	S (m)									
	120	140	160	180	200	220	240	260	280	300
1200	61.7	53.4	45.9	43.7	42.6	43.0	44.6	48.5	56.3	64.1
1220	58.6	50.8	44.5	42.7	41.9	42.1	43.5	46.0	53.5	61.0
1240	56.5	48.9	44.0	42.5	41.8	42.0	43.1	45.0	51.7	58.9
1260	55.0	47.6	44.0	42.7	42.1	42.3	43.3	44.8	50.5	57.5
1280	53.9	46.6	44.4	43.3	42.8	42.9	43.7	45.1	49.5	54.7
1300	53.0	46.4	45.0	44.0	43.6	43.7	44.4	45.6	46.0	49.7
1320	52.3	47.1	45.8	44.9	44.6	44.7	45.3	45.4	44.4	47.1
1340	51.7	47.9	46.7	46.0	45.6	45.7	46.3	45.1	44.0	45.1
1360	51.3	48.8	47.8	47.1	46.8	46.9	46.9	45.2	44.0	43.5
1380	51.0	49.8	48.9	48.3	48.0	48.1	47.3	45.6	44.2	43.3
1400	52.0	50.9	50.1	49.5	49.2	49.3	47.8	46.1	44.6	43.6

CL (m)	S (m)									
	20	40	60	80	100	120	140	160	180	200
1200	150.6	123.0	96.2	70.2	49.8	57.2	93.0			
1220	142.1	116.4	91.3	66.9	50.6	56.5	87.9			
1240	136.4	112.0	88.3	64.8	52.1	57.0	84.5			
1260	132.5	109.1	86.3	64.4	53.9	58.1	82.1			
1280	129.8	107.1	85.0	65.1	56.0	59.6	74.7			
1300	127.9	105.8	84.2	66.2	58.3	61.4	68.8			
1320	126.6	105.0	83.7	67.5	60.7	61.4	65.1			
1340	125.7	104.5	83.5	69.0	63.2	62.2	62.3	84.2		
1360	125.2	104.2	83.4	70.7	65.7	63.4	60.1	81.4		
1380	125.0	104.2	83.5	72.8	68.4	64.9	60.3	79.1		
1400	124.9	104.3	84.5	74.9	71.0	66.5	61.4	77.2		

Figure 4.4: Maximum effective tension for aluminium cable configurations using 4 buoys of type B2 (left) and copper cable configurations with 9 buoys of type B2 (right) at 90° load angle in the SOL state.

CL (m)	S (m)									
	120	140	160	180	200	220	240	260	280	300
1200	7.3	6.3	5.6	5.1	4.9	4.8	5.2	6.0	6.9	7.9
1220	6.4	5.6	5.0	4.6	4.5	4.3	4.6	5.4	6.1	7.0
1240	5.7	5.1	4.6	4.2	4.2	4.0	4.3	4.9	5.6	6.3
1260	5.3	4.7	4.2	4.0	4.0	3.8	4.0	4.6	5.2	5.8
1280	4.9	4.4	4.0	3.8	3.8	3.6	3.8	4.3	4.9	5.2
1300	4.7	4.2	3.8	3.6	3.6	3.5	3.6	4.2	4.3	4.3
1320	4.4	4.0	3.7	3.5	3.5	3.4	3.5	3.8	3.8	3.8
1340	4.3	3.9	3.6	3.4	3.4	3.3	3.4	3.4	3.5	3.5
1360	4.1	3.7	3.5	3.3	3.4	3.2	3.2	3.1	3.2	3.3
1380	4.0	3.6	3.4	3.2	3.3	3.1	3.0	2.9	2.9	3.0
1400	3.8	3.5	3.3	3.1	3.2	3.1	2.9	2.7	2.6	2.7

CL (m)	S (m)									
	20	40	60	80	100	120	140	160	180	200
1200	15.2	14.3	13.2	9.4	5.9	7.9	12.2			
1220	14.8	13.9	12.3	8.5	5.4	7.2	11.6			
1240	14.5	13.7	11.6	7.9	5.0	6.7	10.8			
1260	14.4	13.5	11.0	7.5	4.8	6.3	10.1			
1280	14.3	13.2	10.4	7.2	4.6	6.0	8.1			
1300	14.2	12.8	9.7	6.9	4.4	5.8	6.6			
1320	14.2	12.5	9.2	6.6	4.3	5.0	5.5			
1340	14.2	12.3	8.8	6.4	4.2	4.5	4.7	5.8		
1360	14.3	11.6	8.4	6.1	4.1	4.1	4.2	4.9		
1380	14.2	10.9	8.2	5.9	4.0	3.8	3.9	4.4		
1400	13.5	10.4	8.0	5.8	3.9	3.5	3.7	4.1		

Figure 4.5: MBR for aluminium cable configurations using 4 buoys of type B2 (left) and copper cable configurations with 9 buoys of type B2 (right) at 90° load angle in the SOL state.

CL (m)	S (m)									
	120	140	160	180	200	220	240	260	280	300
1200	32.2	25.6	22.3	23.5	23.7	22.4	20.4	18.0	15.9	14.2
1220	34.3	26.8	24.5	25.6	25.7	24.2	21.9	19.2	16.9	15.0
1240	35.1	27.1	26.3	27.4	27.3	25.6	22.9	20.1	17.5	15.5
1260	34.8	27.1	27.9	28.9	28.6	26.7	23.7	20.5	17.7	15.5
1280	33.8	27.6	29.3	30.2	29.7	27.5	24.2	20.6	17.3	19.9
1300	32.5	28.8	30.5	31.3	30.6	28.1	24.3	20.0	17.7	38.3
1320	31.0	29.8	31.4	32.1	31.3	28.4	24.0	26.4	42.5	54.4
1340	29.7	30.8	32.3	32.8	31.7	28.4	23.2	38.4	55.9	68.9
1360	29.8	31.6	33.0	33.4	32.0	28.2	26.6	49.6	68.2	82.1
1380	30.5	32.2	33.5	33.8	32.0	27.6	35.8	60.0	80.4	98.0
1400	31.1	32.7	33.9	34.0	31.9	26.6	44.6	70.2	94.2	113.1

CL (m)	S (m)									
	20	40	60	80	100	120	140	160	180	200
1200	15.7	20.8	28.0	37.7	22.0	14.3	9.1			
1220	17.1	22.6	30.4	40.5	23.8	15.1	9.5			
1240	18.3	24.2	32.4	42.5	25.2	15.4	9.6			
1260	19.4	25.4	34.0	43.8	26.4	15.5	9.3			
1280	20.4	26.6	35.3	44.7	27.3	15.2	25.8			
1300	21.3	27.6	36.4	45.3	28.1	14.0	48.9			
1320	22.1	28.5	37.3	45.6	28.7	26.6	68.9			
1340	22.8	29.3	38.1	45.7	29.2	39.6	89.6	101.1		
1360	23.5	30.0	38.5	41.7	29.5	51.2	108.9	123.0		
1380	24.1	30.6	38.6	37.4	29.8	63.1	126.5	143.7		
1400	24.7	31.2	38.7	33.4	29.9	75.2	142.3	162.1		

Figure 4.6: Maximum horizontal excursion for aluminium cable configurations using 4 buoys of type B2 (left) and copper cable configurations with 9 buoys of type B2 (right) at 90° load angle in the SOL state.

A closely spaced buoy centred in the middle section of the cable causes the cable to have a long unsupported hanging section between the HOPs and the first buoys. As a result, the unsupported hanging section will have a high weight leading to high tension at the HOPs or the first buoys from

both ends. Additionally, the buoyant force of the buoys will be concentrated in the middle section, which causes this section to float closer to the surface into the regions with high current velocity. Consequently, the middle section of the cable exceeds the surface clearance limit with a large horizontal excursion. For copper cable configurations using buoy B2, it is observed that only a short cable section will float in the strong current region when the buoys are gathered in the middle section of the cable at the smallest spacings. This is due to the buoyant forces of the buoys being too concentrated only at the middle section of the cable. However, when the buoys are more distributed but spaced at shorter distances than 100 m, a longer middle section of the cable will float in the strong current region, as shown in Figure 4.7. As a result, a larger surface area in the middle section of the cable is exposed to a strong hydrodynamic current load leading to a larger horizontal excursion, as seen in Figure 4.8.

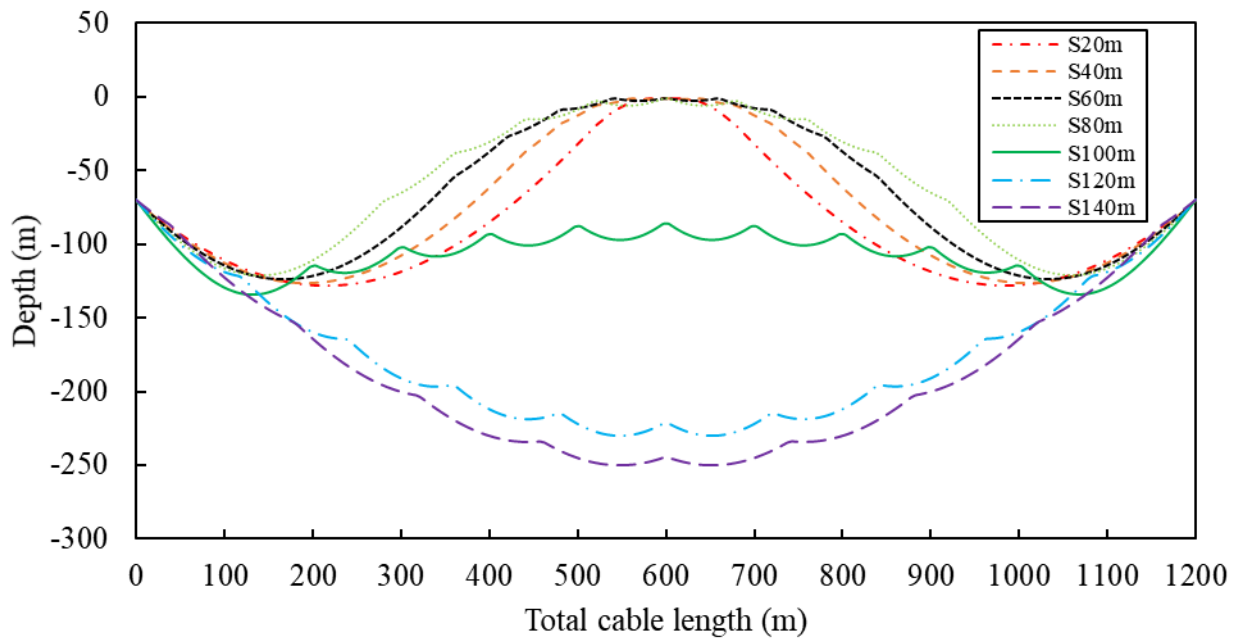


Figure 4.7: Horizontal excursion profile with varying spacings in steady-state under 90° load angle and viewed from the transverse direction for B2-CU-CL1200m-9B.

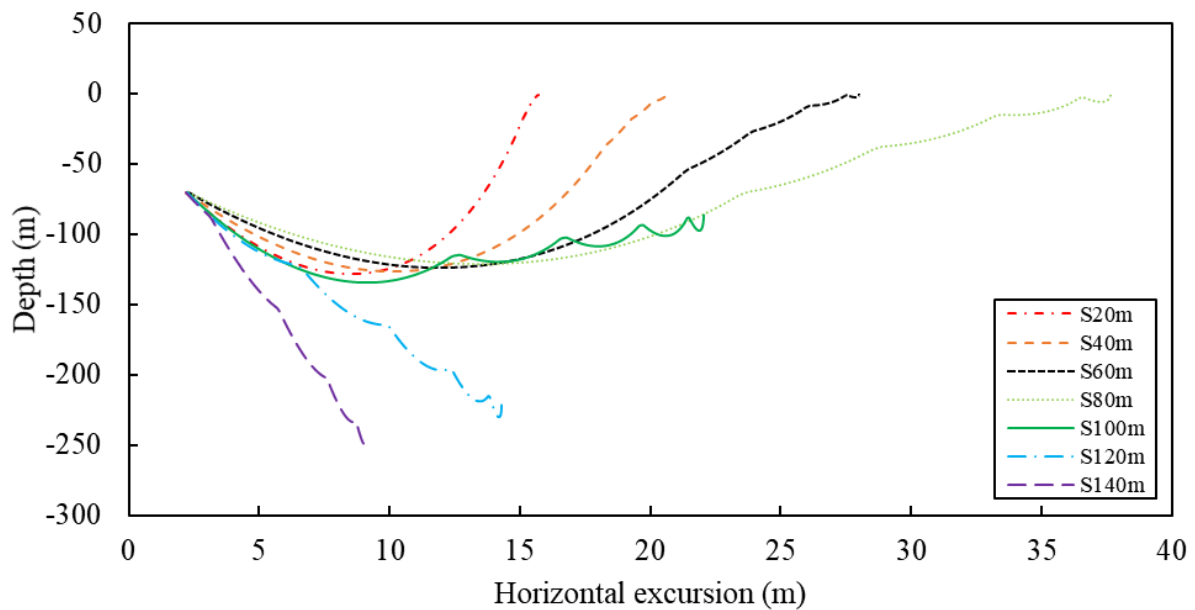


Figure 4.8: *Horizontal excursion profile viewed from 0° for B2-CU-CL1200m-9B with varying spacings.*

Generally, increasing the cable length will shift the location of maximum effective tension from the first buoys to the HOPs. If the depth of the first buoy is already lower than the HOP, increasing the cable length will only increase the cable tension at the HOP. This is due to a smaller buoyant force provided by the first buoy compared to the spar floater. In addition, this will increase the sagging of the unsupported hanging cable section between the HOPs and the first buoys. MBRs decrease as the sagging increase. When the cable length increases in configurations with large buoy spacings, it is observed that the cable touches the seabed. Consequently, the horizontal excursions become extremely large due to the seabed friction not being specified in the simulation. This is shown in Figure 4.3 (right) and Figure 4.6. These cases are omitted because it exceeds the seabed clearance limit. The aluminium cable is lighter than the copper cable. So by increasing the cable length at the optimal spacings, the depths of the first buoys will be reduced. This sequence of events will shift the location of maximum effective tension from the first buoys to the HOPs and simultaneously lower the MBR, as shown in Figure 4.9. These adverse effects can be avoided when the buoys are distributed evenly at the best spacings with the optimal cable lengths, further confirming the study done by Schnepf et al. [54].

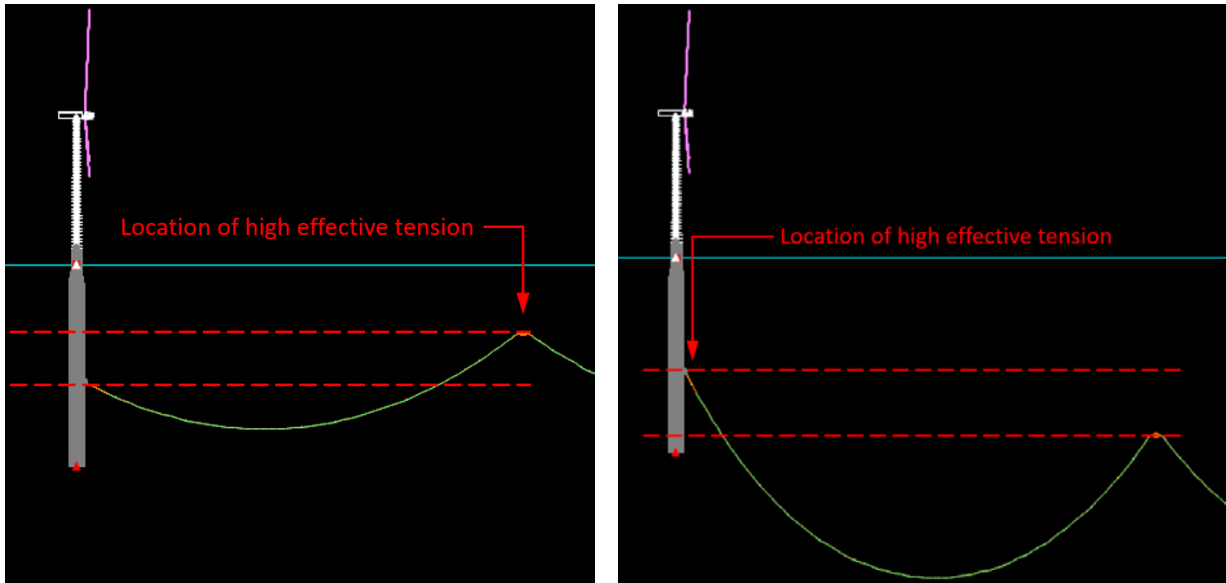


Figure 4.9: Location of highest effective tension for B1-AL-CL1200m-3B-S320m (left) and B1-AL-CL1400m-3B-S320m (right) at 90° load angle in the steady-state analysis.

The PASS SOL cases are extracted and converted to the EOL state. Steady-state analysis of the EOL state for the aluminium cable resulted in 3 fail cases out of 100. This failure is due to MBL exceedance. On the other hand, none of the copper cable cases fails when examining the SOL PASS cases further in the EOL state. The higher MBL limit and smaller diameter of copper cable compared to the aluminium cable are possible reasons. For a fixed and uniform marine growth thickness and density, a smaller diameter cable will result in a lower total weight of the marine growth due to a lesser surface area for it to develop. It is also worth noting that the copper cable exhibits higher axial stiffness than the aluminium cable, which might cause a larger number of PASS cases in the copper cable configuration.

As the load angle shifts from transverse to inline, the number of PASS cases decreases. Therefore, the 90° load angle is the predominant angle. The EOL state of the cable proves to be more critical as it filters additional PASS cases from the SOL state in the predominant load angle.

All in all, it can be seen that cable length, buoy spacing, and buoy size are interrelated factors affecting the MBR, maximum effective tension, and maximum horizontal excursion of a configuration. Moreover, the hydrodynamic load from currents in the steady-state simulation will further amplify the maximum horizontal excursion of the configuration. The first parameter to be determined for both cable types is the optimal number of buoys used in the configuration, followed by the most suitable buoy spacings and cable lengths for a particular buoy and cable type. SOL

analysis should be done prior to the EOL analysis to optimise the design process. The generated configurations from both states can then be analysed only at the 90° load angle.

4.2 Dynamic Analysis

Dynamic analyses are carried out with a constant time step and the implicit solution method. The time domain analyses are performed in two stages: 300 s build-up time and 3600 s actual simulation time. 3600 s are selected because it is the usual time frame of a steady wind condition for wind turbine analysis consideration. Three different seeds are used for the wind and wave loads. Preliminary dynamic analysis help to select the best configurations from the PASS steady-state cases. Based on the findings in the steady-state analyses, each preliminary dynamic analysis in this section is focused on the 90° load angle and the EOL state. The results from the preliminary analyses are filtered by dynamic acceptance criteria and evaluated with the Fitness Factor. The best cases selected from each buoy and cable type are subjected to full dynamic analyses in all load angles, loading conditions, and marine growth states.

4.2.1 Preliminary Dynamic Analysis

Table 4.5 summarises the results of preliminary dynamic analysis on all matching configuration cases of PASS cases from the steady-state analysis. Matching data points refer to the case file with the same configuration but tested in different load angles. The PASS cases in the preliminary dynamic analysis are assessed based on the Fitness Factor optimisation criterion. Fitness Factor, Normalised MBL, and Normalised MBR for aluminium and copper cable using buoy B1 are shown in Figure 4.10 and Figure 4.11, and for aluminium and copper cables using buoy B2 they are shown in Figure 4.12 and Figure 4.13.

Table 4.5: Preliminary dynamic analysis results.

Buoy Type	Cable Type	Total Tested Case	Number of "PASS" Case	MBL	Causes of Failure		
					MBR (< 2.6 m)	Surface Clearance (> -50 m)	Seabed Clearance (< 10 m)
B1	Aluminium	29	0	29	24	2	0
	Copper	43	8	24	16	1	0
B2	Aluminium	96	15	69	25	2	0
	Copper	33	23	9	0	0	1

Note. MBL = 69 kN for aluminium cable. MBL = 96 kN for copper cable

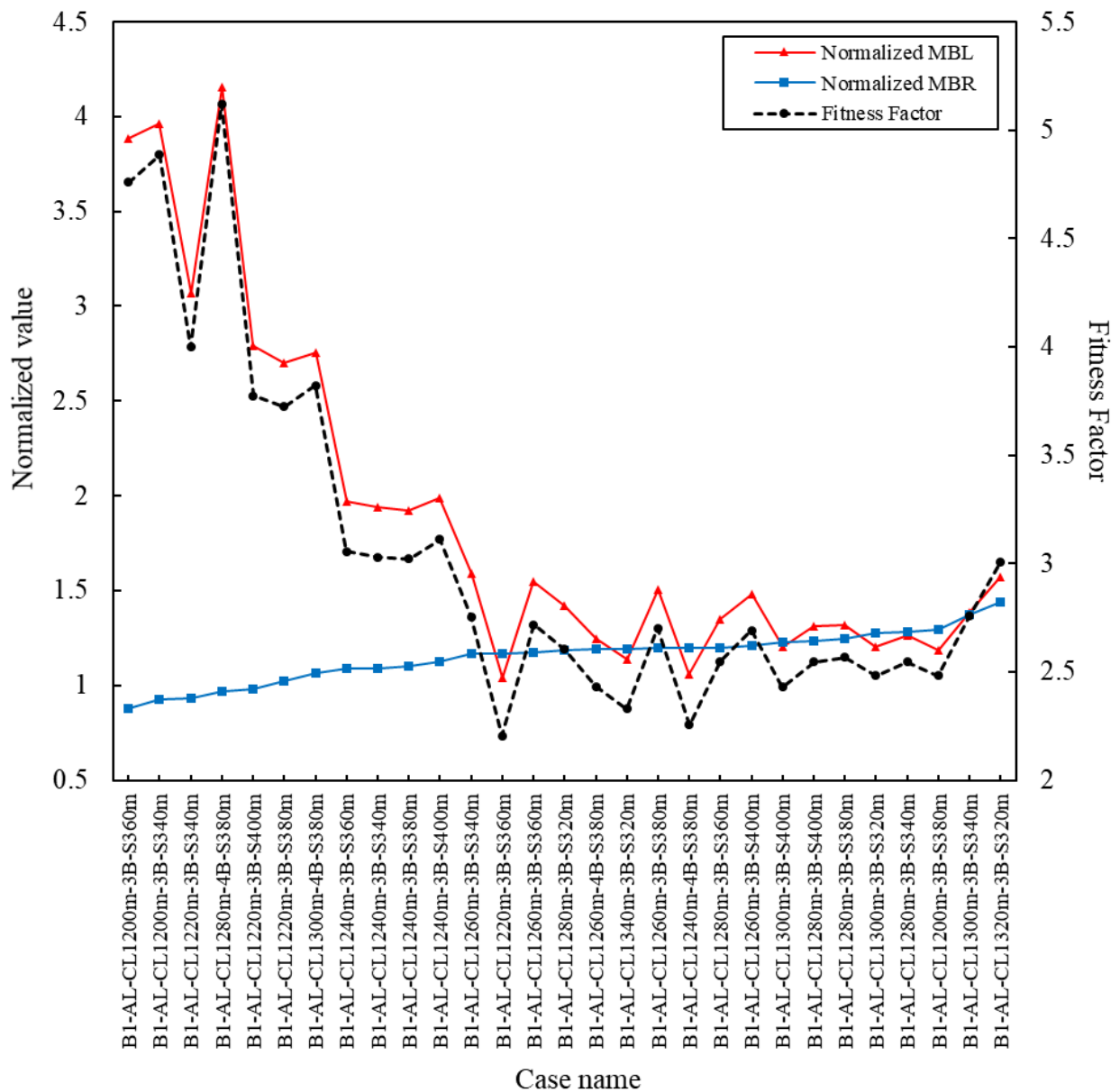


Figure 4.10: Fitness Factor, Normalised MBL and Normalized MBR for aluminium cable configurations using buoy B1.

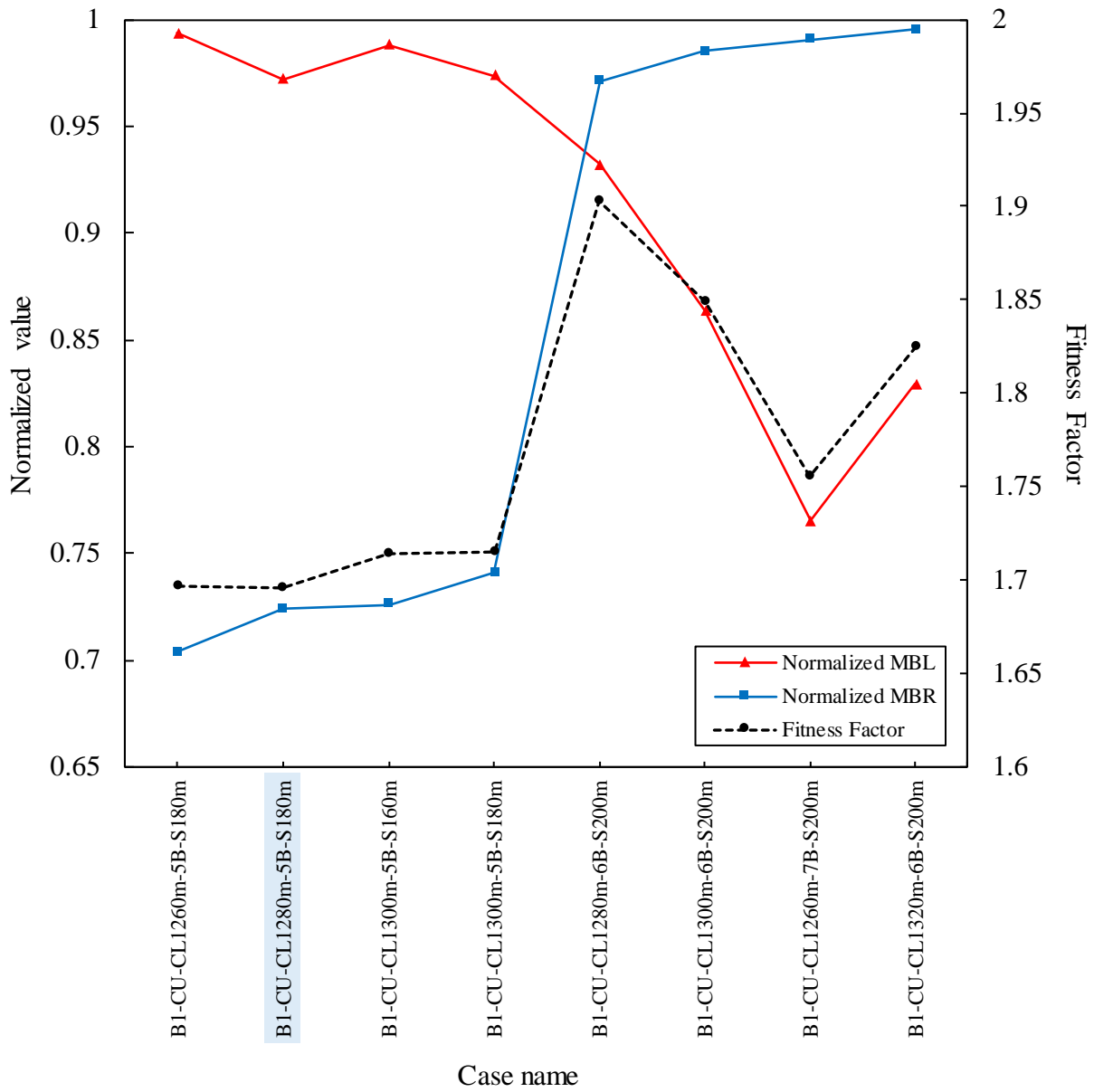


Figure 4.11: *Fitness Factor, Normalised MBL and Normalized MBR for copper cable configurations using buoy B1.*

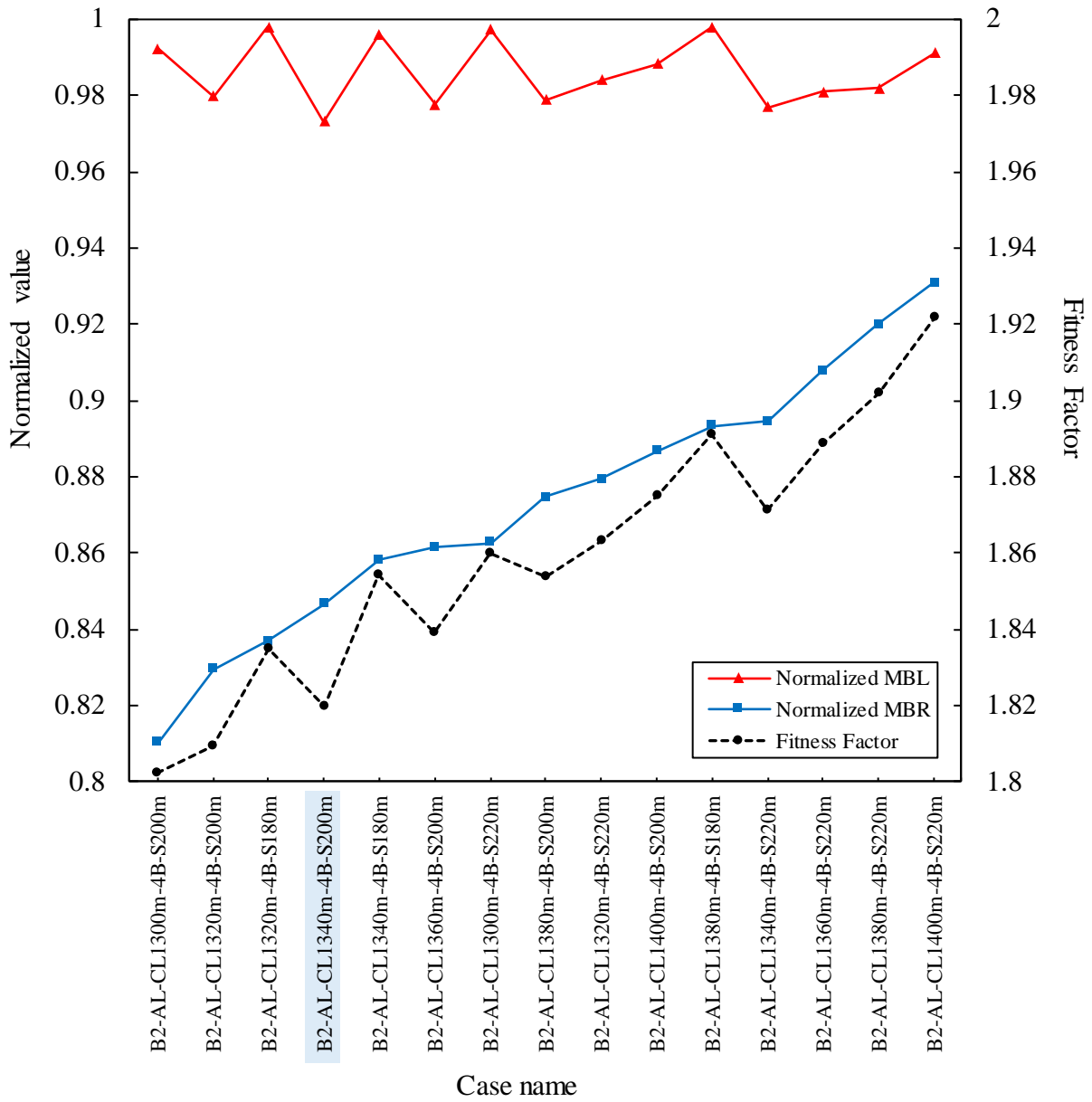


Figure 4.12: *Fitness Factor, Normalised MBL and Normalized MBR for aluminium cable configurations using buoy B2.*

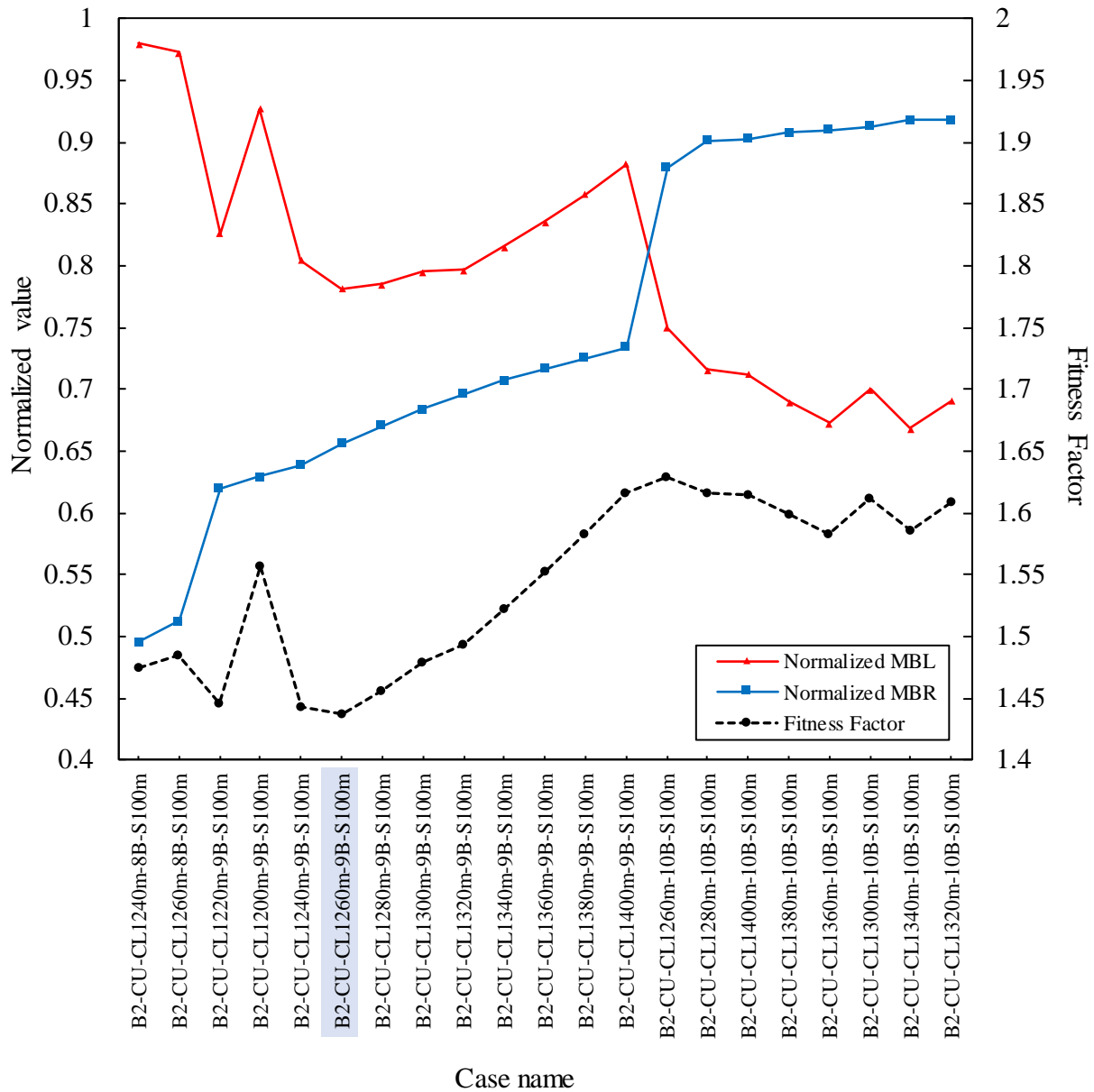


Figure 4.13: *Fitness Factor, Normalised MBL and Normalised MBR for copper cable configurations using buoy B2.*

Table 4.5 shows that none of the cases using buoy B1 passes the acceptance criteria for the aluminium cable configuration. The normalised values in Figure 4.10 show that although some cases satisfy the MBR requirement, all cases still failed due to MBL exceedance with a mean Normalised MBL of 1.89. Therefore, no cases from the aluminium cable configurations with buoy B1 can proceed to full dynamic analysis. For the aluminium cable with buoy B2, several PASS cases are obtained. The MBL is observed to be the major limiting factor with a mean Normalised MBL of 0.99 as opposed to 0.87 for the mean Normalised MBR among the PASS cases. Due to a very low mean Normalised MBL for this category, the best case in this category is selected by the

lowest Normalised MBL with the lowest possible Fitness Factor. The best case for the aluminium cable with buoy B2 is selected as case B2-AL-CL1340m-4B-S200m.

Figure 4.11 and Figure 4.13 show that copper cable configurations are limited by the MBL and MBR criteria. It can be seen that the Normalised MBL and Normalised MBR intersects with one another at one point. The mean Normalised MBL and mean Normalised MBR of the PASS cases in the configurations using buoy B1 are 0.91 and 0.85 respectively, whereas for the setup with buoy B2 they are 0.81 and 0.73 respectively. In general, this shows that the cable tension is more critical to be optimised than the bend radius. Using the lowest Fitness Factor value as the optimisation selection criteria, case B1-CU-CL1280m-5B-S180m is selected as the best case for the copper cable with buoy B1, while case B2-CU-CL1260m-9B-S100m is selected as the best case for the copper cable with buoy B2. Table 4.6 summarises the selected best cases from each buoy type and cable type with the respective Fitness Factor.

Table 4.6: *Best cable configuration cases selected with the Fitness Factor.*

Buoy Type	Cable Type	Case File Name	Fitness Factor	Configuration
B1	Aluminium	No best case was found	-	-
	Copper	B1-CU-CL1280m-5B-S180m	1.696	A
B2	Aluminium	B2-AL-CL1340m-4B-S200m	1.819	B
	Copper	B2-CU-CL1260m-9B-S100m	1.437	C

4.2.2 Full Dynamic Analysis

Full dynamic analyses are done on all cases listed in Table 4.6 to investigate the maximum effective tension, minimum bend radius, and maximum horizontal excursion with the 0° and 45° load angles. The outcomes of these analyses are then compared to determine the best cable type and buoy type for the suspended cable configuration.

Maximum Effective Tension

Table 4.7 summarises the maximum effective tension for all configurations. When comparing the highest maximum effective tension from all three configurations, configuration B resulted in the lowest maximum effective tension at 67.4 kN, whereas the highest effective tension is attained by configuration A with 93.9 kN. At a load angle of 90°, configuration B experienced the highest tension intensification of 21.6% when changing from SOL state to EOL state in the Extreme LC. On the contrary, changing from SOL to EOL state in the rated LC only resulted in a 2% maximum

tension surge. This implies that the marine growth intensifies the cable's effective tension significantly in the extreme LC.

Table 4.7: Cable effective tensions obtained from dynamic analysis.

Load angle	Effective tension (kN)											
	Configuration A				Configuration B				Configuration C			
	SOL		EOL		SOL		EOL		SOL		EOL	
	Max.	Std.	Max.	Std.	Max.	Std.	Max.	Std.	Max.	Std.	Max.	Std.
1. Steady-state												
0° (Transverse)	68.6	-	68.9	-	45.4	-	45.7	-	53.4	-	53.7	-
45°	68.9	-	69.2	-	45.5	-	45.8	-	53.7	-	53.9	-
90° (Inline)	69.1	-	69.4	-	45.6	-	46.0	-	53.9	-	54.2	-
2. Dynamic-rated LC												
0° (Transverse)	70.3	0.5	70.6	0.5	47.3	0.5	47.6	0.5	54.6	0.3	54.9	0.4
45°	71.9	0.9	72.6	0.9	48.4	0.8	49.0	0.9	56.0	0.6	56.7	0.7
90° (Inline)	73.0	1.1	74.1	1.2	49.6	1.0	50.6	1.1	56.9	0.8	57.9	0.9
3. Dynamic-extreme LC												
0° (Transverse)	71.9	1.0	73.9	1.1	49.2	1.2	51.5	1.4	55.9	0.7	58.1	0.9
45°	75.9	2.0	84.7	3.0	52.8	2.1	60.5	3.0	59.0	1.4	67.5	2.4
90° (Inline)	79.7	2.7	93.9	4.5	55.4	2.6	67.4	4.1	62.3	1.9	75.6	3.6

Note.
Max. : Maximum effective tension
Std. : Standard deviation of the maximum effective tension
MBL for aluminium cable = 69 kN. MBL for copper cable = 96 kN
Safety Margin (%) = (MBL – Maximum Effective Tension) / MBL × 100%

The increase in maximum effective tension when changing from the SOL state to the EOL state at 90° load angle for all configurations is compared. Comparing the rated LC to the extreme LC in the EOL state at a load angle of 90°, configuration B experiences the highest increase in tension of 33.2%. It can be observed that the sharp increase of effective tension in the EOL state at around 0.026 arc length per total cable length. This is caused by the marine growth taking effect at depths between -70 m to -100 m. Since there is no marine growth at depths beyond -100 m, the effective tension profile appears to be the same as in the SOL stage for cable length beyond 0.026 arc length per total cable length. It can be deduced that the most critical state for all configurations is the EOL state with the extreme LC at a 90° load angle.

At the most critical state, Configuration B resulted in the lowest effective tension of 67.4kN compared to configuration A and C at 93.9 kN and 75.6 kN. This is due to the lower weight of the aluminium cable compared to the copper cable. When checking the effective tension of these configurations against the limiting MBL of each cable type, configuration C has the biggest safety margin to its MBL limit at 21.2% as opposed to only 2.4% safety margin for configuration B. Meaning that if the environmental loading in the extreme LC is stronger, configuration B is more likely to fail before configuration C. The big gap in the safety margin is due to the Fitness Factor optimisation criteria accounting for both MBL and MBR as a whole instead of individually assessing the regulatory limit.

Maximum effective tension profiles in the rated LC for configurations A, B, and C are plotted in Figure 4.14, Figure 4.16, and Figure 4.18 respectively. The maximum effective tension profiles during the extreme LC for configurations A, B, and C are plotted in Figure 4.15, Figure 4.17, and Figure 4.19 respectively. These figures show that the buoys partially decouple the cable from the FOWTs motion at the middle section of the cable which is supported by the distributed buoys.

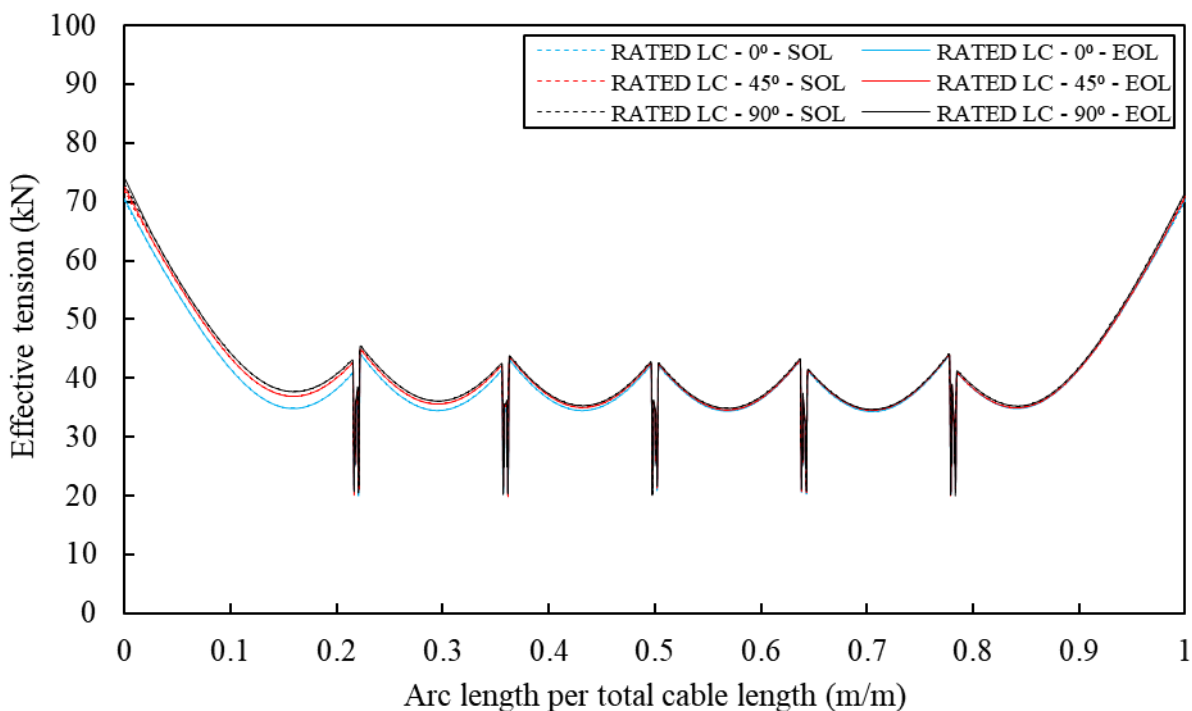


Figure 4.14: Maximum effective tension profiles for configuration A in the rated LC.

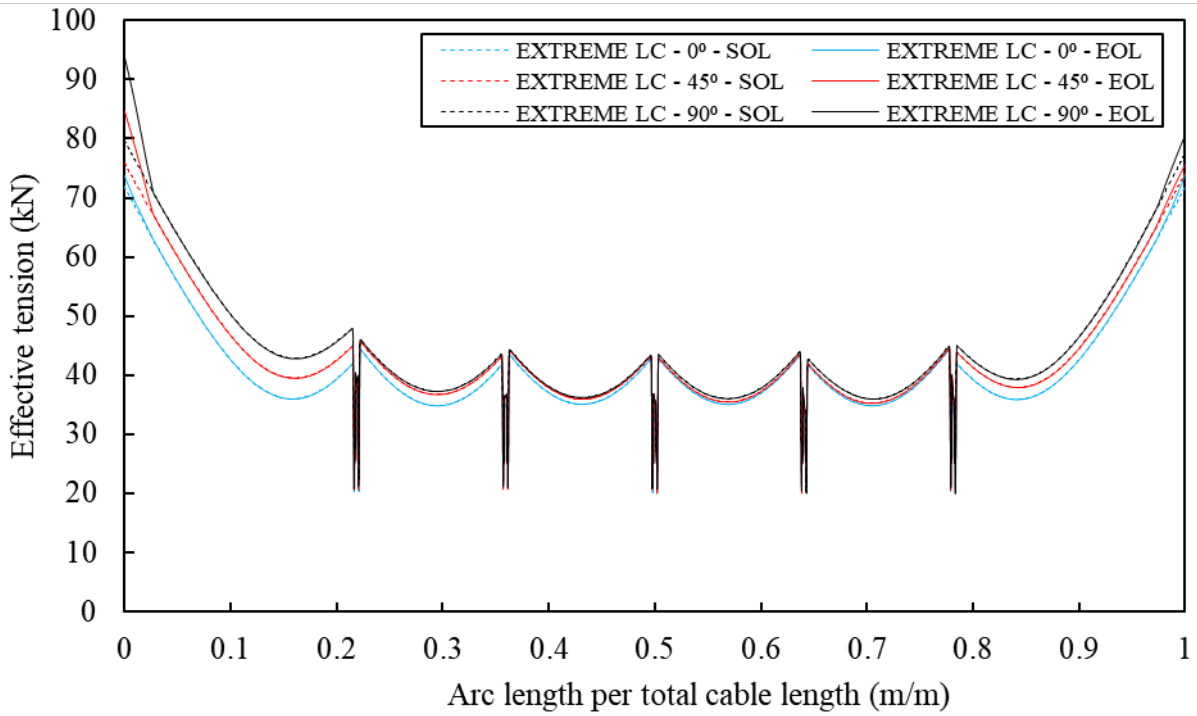


Figure 4.15: Maximum effective tension profiles for configuration A in the extreme LC.

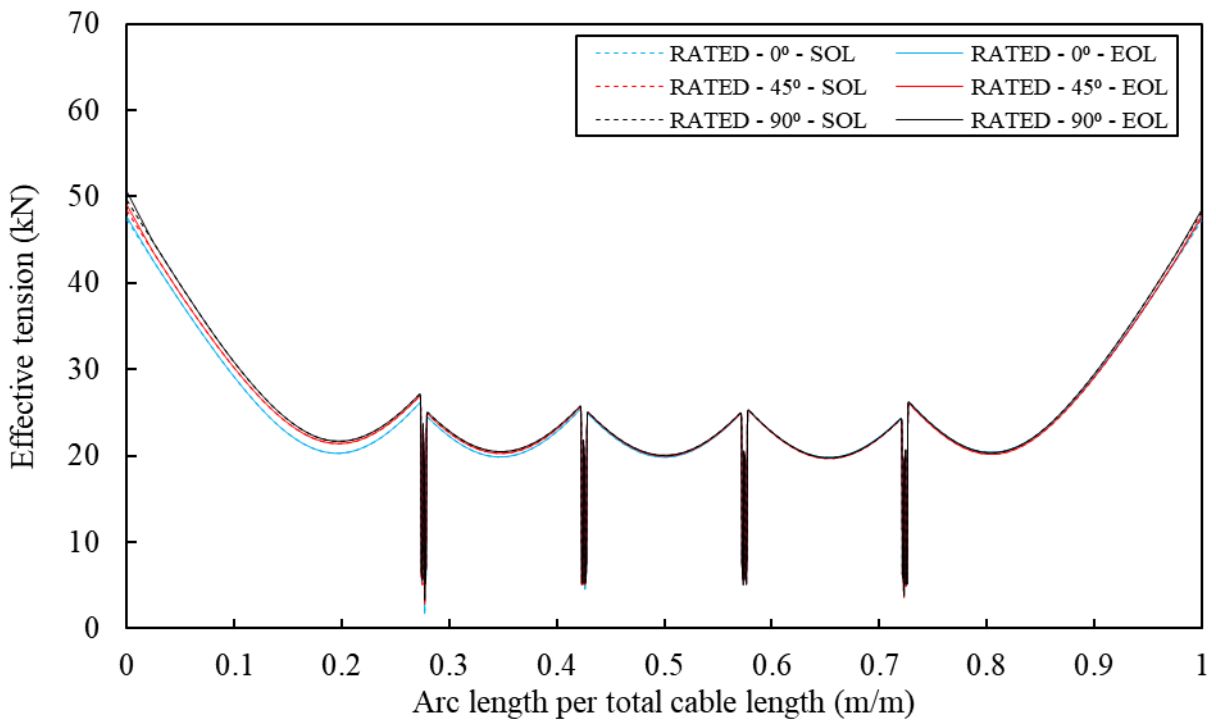


Figure 4.16: Maximum effective tension profiles for configuration B in the rated LC.

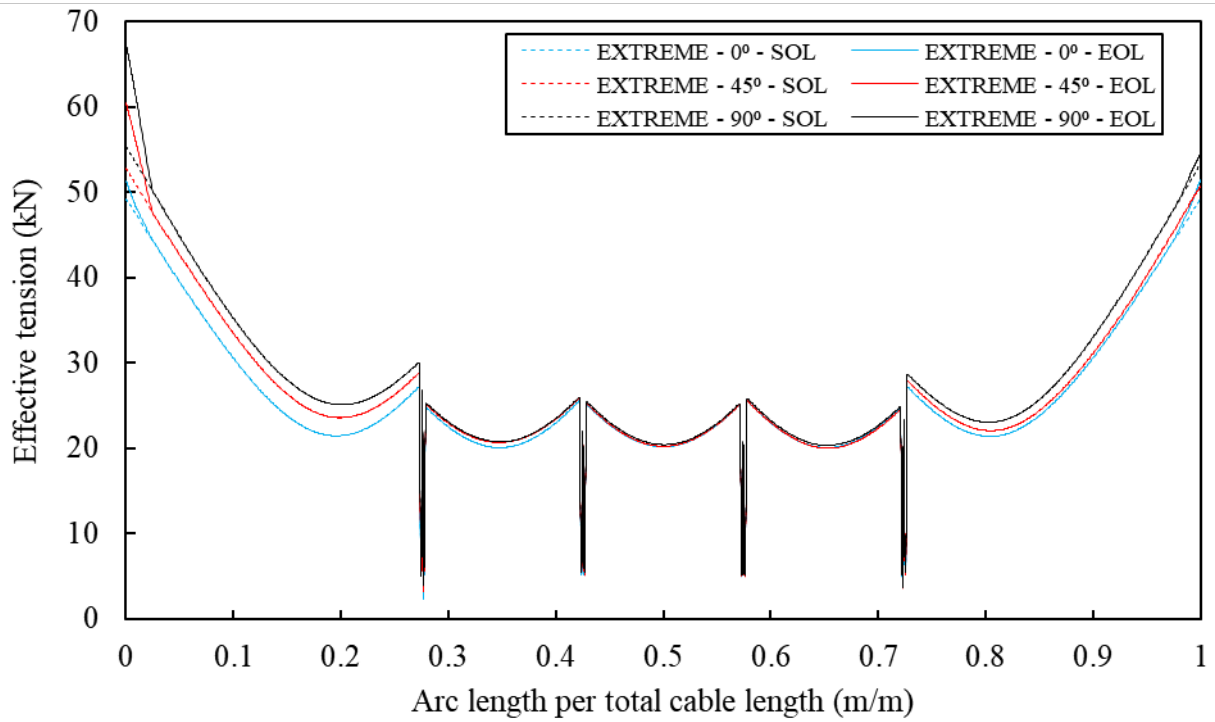


Figure 4.17: Maximum effective tension profiles for configuration B in the extreme LC.

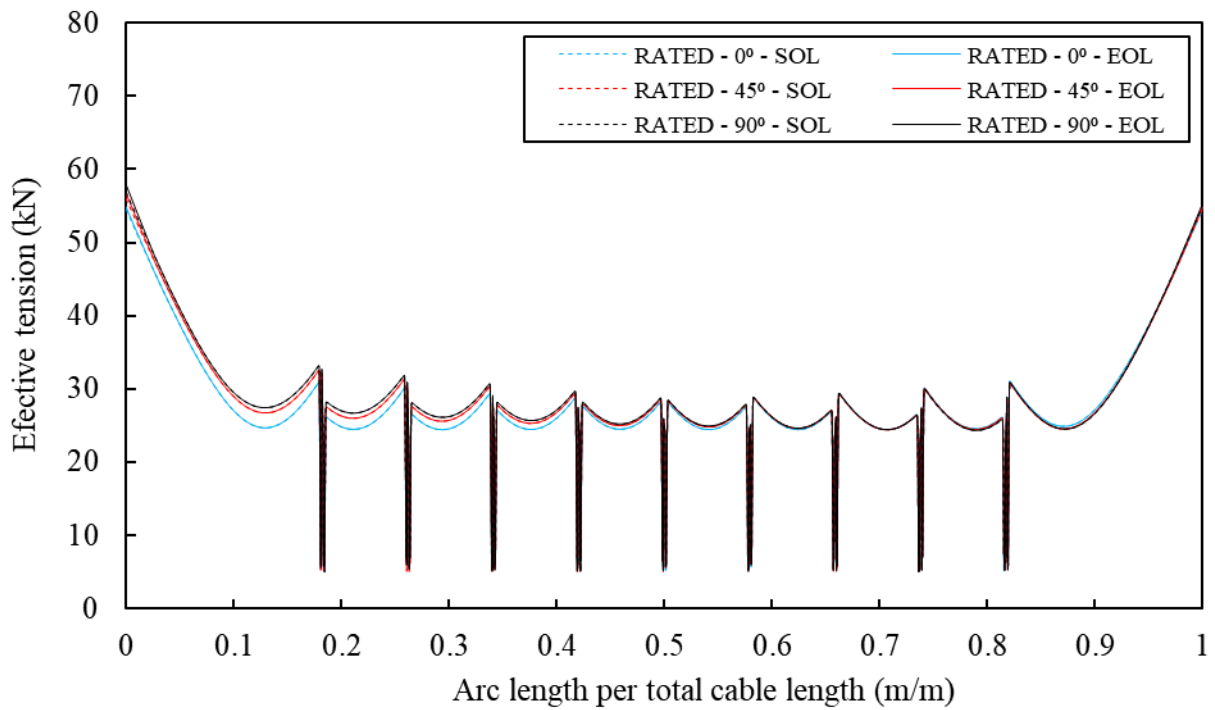


Figure 4.18: Maximum effective tension profiles for configuration C in the rated LC.

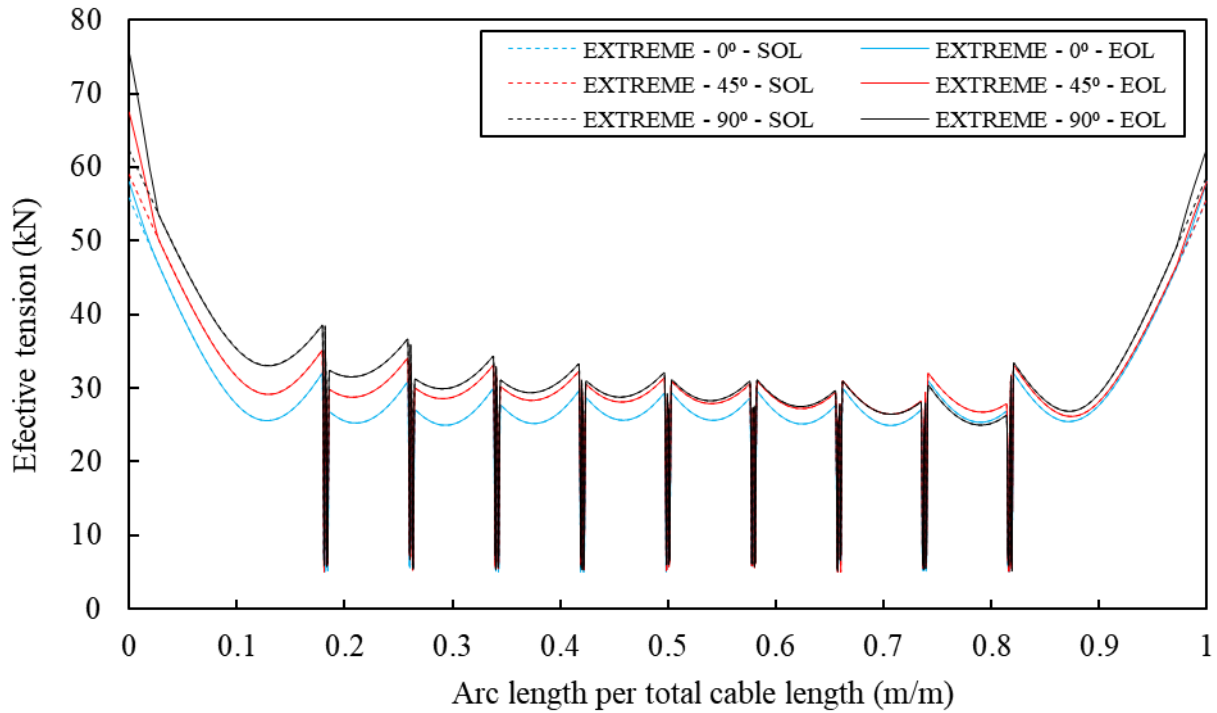


Figure 4.19: Maximum effective tension profiles for configuration C in the rated LC.

Comparing configuration A and configuration C in the most critical state revealed that for the same weight of the copper cable, the smaller buoy B2 in configuration C resulted in a lower tension than configuration A with the bigger buoy B1. Each buoy provides a point of buoyant force and damping when the cable reacts to the FOWT motion. When the buoy size is smaller, more buoys are required to uplift the cable. The higher the number of buoys on the cable, the better the tension can be evenly distributed and dampened along the cable. This will also reduce the tension at the HOP. The tensions at the HOPs can also be explained further by the amount of freely hanging cables between the HOPs and the first buoy from both cable ends. Configuration A has a hanging length of 280 m, while configuration C has a hanging length of 230 m. The longer hanging length in configuration A gives rise to additional inertia, thus causing higher tension at its HOPs than in configuration C.

Minimum Bend Radius

The lowest MBR is at the middle part of the bend stiffener, where the cable enters and exits the stiff buoy. This is expected due to the weight of the unsupported hanging cable between the buoys, causing a sagging shape which bends the cable as it exits the bend stiffeners. The bend stiffener restricts the bending radius of the cable at the buoy-supported section to a radius above 2.6 m, which is the MBR limit used in this study.

MBRs are slightly reduced when the rated LC changes to extreme LC, with the biggest MBR reduction of 16% observed at a 90° load angle in configuration C. Referring to Table 4.8, it is shown for all configurations that the smallest MBRs occurred in the 90° load angle during the extreme LC. In this critical state, it can be observed that configuration B possesses the smallest MBR at 3.0 m, whereas the largest MBR can be observed in configuration C with 3.9 m.

Table 4.8: *MBRs for all configurations obtained from dynamic analysis.*

Load angle	Minimum bend radius, MBR (m)					
	Configuration A		Configuration B		Configuration C	
	SOL	EOL	SOL	EOL	SOL	EOL
1. Steady-state						
0° (Transverse)	4.1	4.1	3.4	3.4	4.7	4.7
45°	4.1	4.1	3.4	3.4	4.7	4.7
90° (Inline)	4.0	4.0	3.4	3.4	4.8	4.8
2. Dynamic-Rated LC						
0° (Transverse)	4.0	4.0	3.3	3.3	4.5	4.5
45°	4.0	4.0	3.3	3.3	4.6	4.6
90° (Inline)	3.9	3.9	3.4	3.4	4.7	4.7
3. Dynamic-Extreme LC						
0° (Transverse)	4.0	4.0	3.3	3.3	4.4	4.4
45°	3.7	3.7	3.1	3.1	4.1	4.1
90° (Inline)	3.6	3.6	3.0	3.0	3.9	3.9

It is also observed that the MBRs barely change when the marine growth state changes from SOL to EOL. This is due to the assumption of the environment where the marine growth is not present in water depths below -100 m. Since all buoys at the middle section of the cable in all three configurations settled at water depths below -100 m, the effects of marine growth development on MBRs cannot be observed.

Three parameters are responsible for the differences in MBRs among the configurations: the weight of the cables, the spacings between the buoys, and the bending stiffnesses. The hanging weight of the cable causes the cable to sag due to gravitational force. The amount of cable sag is also controlled by the spacings between the buoys and the total cable lengths. The bending stiffness is

the cable property that resists the bending caused by the hanging weight. The MBR in configuration B is the smallest because of the lower bending stiffness of the aluminium cable and the long distance between the buoys at 200 m spacing. With a spacing of 200 m, the total weight of the hanging cable between the buoys in configuration B is 8370 kg, while a slight reduction of the buoy spacing to 180 m in configuration A resulted in 8658 kg of hanging cable weight. Despite the heavier hanging weight in configuration A, the MBR is larger due to the higher bending stiffness of the copper cable. Configuration C has the largest MBR due to the smallest spacing between the buoys with 100 m spacing, leading to a smaller accumulated cable weight at only 4810 kg that causes it to sag.

Maximum Horizontal Excursion

Maximum horizontal excursions for all three configurations are observed at 0° and 45° load angles. Table 4.9 summarises the maximum horizontal excursions for all three configurations measured from the 0 global x-axis line. Changes from the SOL state to the EOL state do not significantly impact the change in horizontal excursions. This is due to the marine growth presence only around the HOPs, where the cables settle in water depths above -100 m. Dynamic analysis shows a significant increase in excursion from the steady-state simulation, with the highest excursions observed in the rated LC and at transverse load angle (0°) in configuration A with 95% increment.

Table 4.9: Comparison of maximum horizontal excursion in all configurations.

Marine growth state	Maximum horizontal excursion (m)					
	Steady-state		Dynamic rated LC		Dynamic extreme LC	
	0°	45°	0°	45°	0°	45°
1. Configuration A						
SOL	17.4	9.6	33.9	18.9	22.5	14.9
EOL	17.4	9.6	34.0	18.9	22.5	14.9
2. Configuration B						
SOL	31.7	17.5	47.8	26.6	36.9	23.4
EOL	31.7	17.5	47.8	26.6	36.9	23.4
3. Configuration C						
SOL	26.4	14.2	42.7	23.4	32.3	23.1
EOL	26.4	14.2	42.7	23.5	32.3	23.1

Figure 4.20 shows the shape and depth of the selected cases in steady-state under 0° load angle viewed from a transverse perspective. Figure 4.21 compares the horizontal excursion profiles under dynamic loads in 0° load angle.

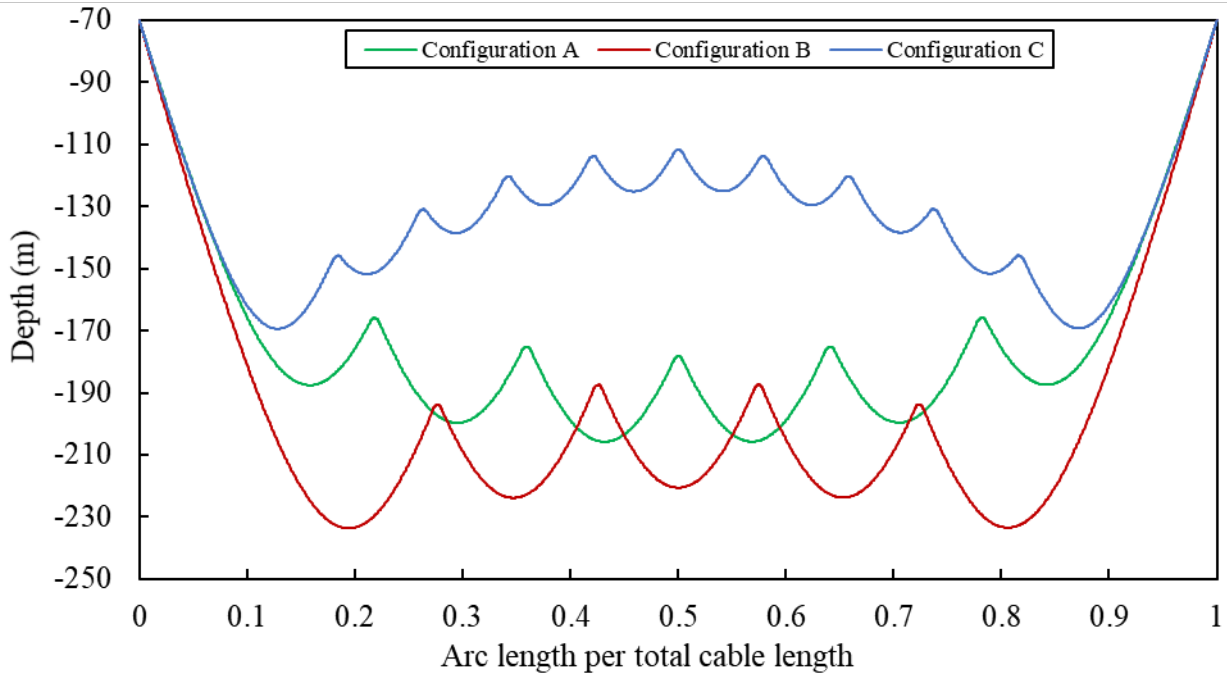


Figure 4.20: Cable shapes of the selected configurations from each category viewed from the transverse direction (0° angle) in steady-state.

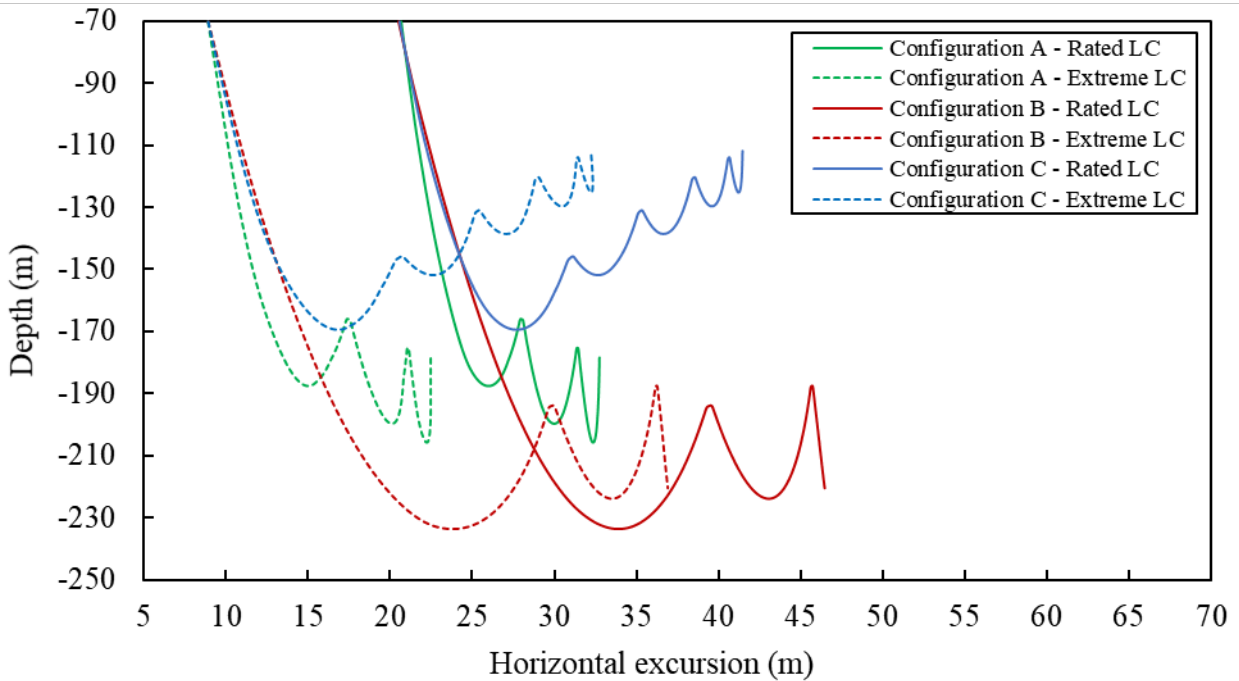


Figure 4.21: Horizontal excursion profile in rated LC and extreme LC from 0° load angle measured in the positive direction of the global x-axis.

The maximum horizontal excursions are affected by the numbers of buoys used, sizes of buoys, drag areas of the cable, cable weight, depths, and currents. Configuration B has more buoys than configuration C. Configuration B also settles at the deepest depth with a weaker current than configuration C, which settles closer to the surface with a stronger current. Despite being exposed to a weaker current, configuration B obtains the highest maximum horizontal excursion with 47.8 m excursion compared to 42.7 m excursion of configuration C. For the same buoy size of buoy B2, configuration B has 4 buoys and a longer cable with a larger diameter. On the other hand, configuration C has 9 buoys and a shorter cable with a smaller diameter. More buoys with larger accumulated drag areas in configuration C are expected to cause the cable to obtain a larger horizontal excursion than in configuration B. Despite more buoys attached, the heavier weight of the copper cable in configuration C caused it to exhibit more stability to resist the current load and thus have a lesser excursion than configuration B.

The FOWT surge during the extreme LC is 8.9 m, and the FOWT surge during the rated LC is around 21.8 m. Referring to Figure 4.21, larger horizontal excursions occurred during the rated LC when measured with respect to the 0 global x-axis. On the contrary, the horizontal excursions in the extreme LC appear to be larger in all configurations when the mean FOWT surge in the respective LC is deducted from the horizontal excursions. The largest horizontal excursion is measured in configuration B at 28 m. This is due to further FOWT sway during rated LC where the turbine is in operation. During operation, the wind force acts on the blades and pushes the turbine in the wind direction. When turbines are not operating during extreme LC, the blades are positioned in a way that will give the least resistance to the wind causing less spar sway. Nonetheless, the currents in the extreme LC are still stronger than the currents in the rated LC, causing the cable to deviate more in the extreme LC.

All in all, the suspended inter-array power cable concept is proven to be feasible using the proposed buoy setup and optimisation methodology. The highest effective tension occurs at the hang-off location of the cable. Configuration with aluminium cable resulted in the lowest effective tension, but the copper cable can withstand higher effective tension with a significantly larger safety margin than the aluminium cable configuration. Copper cable configuration also resulted in a lower horizontal excursion than aluminium cable. The smaller buoys yield the most optimal designs for both cable types compared to the bigger buoys. The largest minimum bend radius occurs when the buoys are closely spaced.

5 CONCLUSIONS

Dynamic responses of fully suspended inter-array power cable configurations between two FOWTs are investigated with regards to the impact on cable effective tension, minimum bend radius, and horizontal excursion. The effect of marine growth on the cables is also considered based on the Norwegian sea's environmental conditions. Different of cable types and the choice of buoy sizings for suspended cable configurations are also taken into account. The feasibility of the suspended inter-array power cable concept is determined. The present study is done in four stages, in a way that every stage filters the most suitable configurations that will be examined in the next stage. The first stage is SOL state analysis in steady-state, where only the suitable cases are shortlisted using the acceptance criteria. Then, the shortlisted cases are reanalysed EOL steady-state analysis of the previously is performed, where the marine growth effects are implemented. The results undergo the same filtration process. The configurations that passed the acceptance criteria in the SOL state and EOL state then proceed for preliminary dynamic analysis in the third stage, where only the best configurations from each buoy and cable type are selected for the final stage. The selection is based on an optimization criterion called Fitness Factor, and only three configurations are selected. These configurations are selected due to the lowest possible Fitness Factor value. Full dynamic analysis is implemented on these configurations. The main conclusions from steady-state analysis are summarised below, and several of these findings coincide with the observations during dynamic analysis:

- The inline load is the predominant load angle, and the extreme LC is the most critical LC to be tested on all configurations in the steady-state analysis and dynamic analysis. This applies to the impact on maximum effective tension, MBR, and horizontal excursion.
- Smaller buoy sizes are more suited to fine-tune the configuration to distribute the tension more evenly along the cable. A larger buoy necessitates fewer buoys, resulting in a large spacing between the buoys when the tension is aimed to be distributed. The greater spacing increases the length of the unsupported hanging cable between the buoys, resulting in increased cable tension and a more sagging cable shape that lowers the MBR.
- MBL is the most critical failure driver for copper cable configurations due to the heavier weight of the copper cable. However, copper cable configurations are less likely to fail due to MBR because of the smaller buoy spacing required to maintain the suspended configuration.
- Aluminium cables are more easily affected by choice of buoy sizes due to their lighter weight.

- Closely spaced buoys will cause the buoyant force to be concentrated at the middle part of the cable. This triggers the middle section of the cable to float closer to the surface into the strong current regions and narrow the sea surface clearance limit. More importantly, the tensions at the HOPs will be high due to the longer lengths of unsupported hanging cable weight between the HOPs and the first buoys from each end.

Based on the result of full dynamic analyses, the suspended inter-array power cable concept is proven to be feasible using the proposed buoy setup and optimisation methodology. Three configurations are tested for the full dynamic analyses. Out of the three, configuration C is the best configuration due to its largest safety margin and biggest MBR while maintaining a moderate amount of horizontal excursion. The main findings from the dynamic analysis are the following:

- The large variations in safety margins of between the cases are due to the Fitness Factor, which considers both MBL and MBR as a whole rather than assessing the regulatory limit individually.
- The buoys decouple the cable from the FOWTs motion at the middle section which is supported by the evenly distributed buoys. Each buoy provides a buoyant force, weight, and damping point when the cable responds to the motions of the FOWTs. The more buoys are positioned on the cable, the more likely the tensions can be distributed evenly and dampened along the cable, thus reducing the tension at the HOPs. Based on this observation, copper cables are deemed to be more suitable for dynamic application in this study due to their higher tolerance to fit more buoys. Additionally, the heavier weight to diameter ratio of the copper cable reduces the amount of horizontal excursion.
- The highest maximum effective tension is at the HOPs. This can be explained by the amount of freely hanging cables between the HOPs and the first buoy from both ends of the cable. A longer hanging length increases the inertia, thus causing higher tension at its HOPs when the floater is in motion.
- While the effect of marine growth on MBR and horizontal excursion are negligible, the same conclusion cannot be made for maximum effective tension. This is due to the HOPs of all configurations located in the water depth affected by marine growth. When changing from SOL state to EOL state, the maximum effective tension increases by 21.6% in the extreme LC while only 2% in the rated LC. The difference in the increase

of maximum effective tension is due to the floater motion responding to a large wave amplitude specified in the extreme LC.

- Configuration B shows the highest horizontal excursion at 233.6 m water depth. However, the water depth alone is not the only determining factor of the maximum horizontal excursion. The maximum horizontal excursions are affected by the numbers of buoys used, sizes of the buoys, drag areas of the cables, cable weights, depths, and currents.
- The lowest MBR is at the bend stiffener closest to the HOPs. This is caused by the amount of freely hanging cable between the HOPs and the first buoy from both ends of the cable.
- Rated LC shows a high horizontal excursion when the mean spar surge is not considered. However, when the mean spar surge is considered, the horizontal excursions in the extreme LC appear to be higher in all configurations with the maximum at 28 m. The currents in extreme LC are still higher than the currents in the rated LC, causing the cable to deviate slightly more in the extreme LC.
- When varying the load angle from 0° to 45° , the horizontal excursions are reduced by around 45% in rated LC and 30% in extreme LC.

In conclusion, this work has proven that the suspended inter-array power cable concept is feasible using the proposed buoy setup and optimisation methodology. Copper cable is more suitable for the dynamic applications of the suspended inter-array power cable configuration. This is due to the heavier weight of the copper cable and higher MBL limit than the aluminium cable. A smaller buoy size is more suitable to distribute the tension evenly along the cable and decrease the tension at the HOPs compared to the bigger buoy. The inline load is the most critical load angle for studying maximum effective tension, and the extreme LC is the most crucial LC to be tested on all configurations. These apply to the study on maximum effective tension, MBR, and horizontal excursion. It can be seen that marine growth noticeably affects the maximum effective tension. The configuration variables for this study can be sorted in the decreasing order of importance as follows: the cable type, the size of the buoy, the number of buoys, the spacings between buoys, and the total cable lengths.

6 RECOMMENDATIONS FOR FUTURE WORKS

This work focuses on the optimization of suspended inter-array power cable configurations for floating offshore wind turbines. There is still more work that can be done to improve this research.

In the following are some of the recommendations for future work using the same numerical setup:

- The case study variable can be refined using a smaller buoy spacing step based on the range of the optimal buoy spacing that has been discovered in this study.
- The effect of marine growth can be expanded by considering the marine growth on the spars and cable ancillaries, as well as on the whole length of the cable regardless of the depth.
- The Fitness Factor can be modified by optimizing the MBL and MBR criteria individually. One of the approaches is to calculate the mean maximum effective tension and mean MBR for all PASS cases in the preliminary dynamic analysis. The MBL and MBR criteria can be selected by choosing the case where both values are closest to the mean or above the 50th percentile.
- Test a new configuration with mooring chains fixed to the first buoys from both HOPs to the seabed and redo the same study. This way, the middle section of the cable will be completely decoupled. The design refinement can be focused on the sections between the HOPs and the first buoys where the free-hanging cable caused the highest maximum effective tension. Additional ancillaries such as smaller-sized buoyancy modules can be utilised in the design refinement.
- Failure scenarios of this suspended inter-array cable configuration can be assessed—for instance, a situation where one of the buoys detached from the cable. Additionally, the most critical position of the failed buoy can also be included as part of the assessment.
- The global model can be expanded by introducing more complex weather conditions for specific locations.
- Further analysis can be done to study cable fatigue in this suspended inter-array cable configuration.

REFERENCES

- [1] UNFCCC. The Paris Agreement 2015. <https://unfccc.int/process-and-meetings/the-paris-agreement/the-paris-agreement> (accessed January 11, 2022).
- [2] Maradin D. Advantages and Disadvantages of Renewable Energy Sources Utilization. *International Journal of Energy Economics and Policy* 2021;11:176–83.
- [3] Ricciardelli F, Maienza C, Vardaroglu M, Avossa AM. Wind energy into the future: The challenge of deep-water wind farms. 1 2021;32:321–40.
- [4] Fawthrop A. Hywind Scotland is “proving potential” of floating offshore wind. *NS ENERGY* 2021. <https://www.nsenergybusiness.com/news/company-news/floating-wind-potential-hywind-scotland/> (accessed January 13, 2022).
- [5] Speht R. Ready-to-float: A permanent cost reduction for offshore wind. *Windpower Engineering & Development* 2021. <https://www.windpowerengineering.com/ready-to-float-a-permanent-cost-reduction-for-offshore-wind/> (accessed January 12, 2022).
- [6] Ministry of Petroleum and Energy. Norway opens offshore areas for wind power. GovernmentNo 2020. <https://www.regjeringen.no/en/historical-archive/solbergs-government/Ministries/oed/press-releases/2020/norway-opens-offshore-areas-for-wind-power/id2705986/> (accessed January 11, 2022).
- [7] Offshore Wind Outlook 2019: World Energy Outlook Special Report. *Offshore Wind* 2019:98.
- [8] Srinil N. 13 - Cabling to connect offshore wind turbines to onshore facilities. In: Ng C, Ran L, editors. *Offshore Wind Farms*, Woodhead Publishing; 2016, p. 419–40. <https://doi.org/10.1016/B978-0-08-100779-2.00013-1>.
- [9] Schnepf A, Pavon CL, Ong MC, Yin G, Johnsen Ø. Suspended Inter-Array Power Cable Configurations Between Two Spar Floating Offshore Wind Turbines [Under review]. 2022.
- [10] Jonkman J. Definition of the Floating System for Phase IV of OC3. 2010. <https://doi.org/10.2172/979456>.
- [11] Jonkman J, Butterfield S, Musial W, Scott G. Definition of a 5-MW Reference Wind Turbine for Offshore System Development. 2009. <https://doi.org/10.2172/947422>.
- [12] Sveen D, Nielsen FG, Hanson TD. Floating wind turbine installation. *US7819073B2*, 2010.
- [13] Merger of Statoil and Hydro’s petroleum operations - Storting proposition no 60 (2006-2007) 2007.
- [14] Equinor. StatoilHydro inaugurates floating wind turbine 2009. <https://www.equinor.com/news/archive/2009/09/08/InnovativePowerPlantOpened> (accessed July 8, 2022).
- [15] Unitech Zephyros (Hywind Demo). METCentre 2019. <https://metcentre.no/project/unitech-zephyros-hywind-demo/> (accessed January 17, 2022).
- [16] Launes M. Testfasilitetar for offshore vind inn i katapult-senter. *NCE Maritime CleanTech* 2019. <https://maritimecleantech.no/2019/01/10/testfasilitetar-for-offshore-vind-inn-i-havkatapulten/> (accessed May 25, 2022).
- [17] Skaare B, Nielsen FG, Hanson TD, Yttervik R, Havmøller O, Rekdal A. Analysis of measurements and simulations from the Hywind Demo floating wind turbine. *Wind Energy* 2015;18:1105–22. <https://doi.org/10.1002/we.1750>.
- [18] Hywind 2017. [http://masdar.ae/en/Masdar Clean Energy/Projects/Hywind Scotland](http://masdar.ae/en/Masdar%20Clean%20Energy/Projects/Hywind%20Scotland) (accessed January 17, 2022).
- [19] Løvik H. Mange har vært villige til å ta på seg farskapet - her er historien om Hywinds trange fødsel. *Tu.no* 2017. <https://www.tu.no/artikler/mange-har-vaert-villige-til-a-ta-pa-seg-farskapet-her-er-historien-om-hywinds-trange-fodsel/410309> (accessed January 17, 2022).
- [20] Equinor. Hywind Tampen - Floating Wind Power Project 2019. <https://www.equinor.com/en/what-we-do/hywind-tampen.html> (accessed January 17, 2022).

- [21] Hau E. Windmills and Windwheels. In: Hau E, editor. Wind Turbines: Fundamentals, Technologies, Application, Economics, Berlin, Heidelberg: Springer; 2013, p. 1–21. https://doi.org/10.1007/978-3-642-27151-9_1.
- [22] Hau E. Physical Principles of Wind Energy Conversion. In: Hau E, editor. Wind Turbines: Fundamentals, Technologies, Application, Economics, Berlin, Heidelberg: Springer; 2013, p. 79–87. https://doi.org/10.1007/978-3-642-27151-9_4.
- [23] Sayigh AAM. Comprehensive Renewable Energy: Volume 2. Elsevier; 2012.
- [24] An Y, Pandey MD. A comparison of methods of extreme wind speed estimation. *Journal of Wind Engineering and Industrial Aerodynamics* 2005;93:535–45. <https://doi.org/10.1016/j.jweia.2005.05.003>.
- [25] Masters GM. Renewable and Efficient Electric Power Systems. Wiley; 2013.
- [26] Archer CL, Jacobson MZ. Evaluation of global wind power. *Journal of Geophysical Research: Atmospheres* 2005;110. <https://doi.org/10.1029/2004JD005462>.
- [27] Frandsen S. On the wind speed reduction in the center of large clusters of wind turbines. *Journal of Wind Engineering and Industrial Aerodynamics* 1992;39:251–65. [https://doi.org/10.1016/0167-6105\(92\)90551-K](https://doi.org/10.1016/0167-6105(92)90551-K).
- [28] Magnusson M, Smedman A-S. Air flow behind wind turbines. *Journal of Wind Engineering and Industrial Aerodynamics* 1999;80:169–89. [https://doi.org/10.1016/S0167-6105\(98\)00126-3](https://doi.org/10.1016/S0167-6105(98)00126-3).
- [29] Crespo A, Hernáandez J. Turbulence characteristics in wind-turbine wakes. *Journal of Wind Engineering and Industrial Aerodynamics* 1996;61:71–85. [https://doi.org/10.1016/0167-6105\(95\)00033-X](https://doi.org/10.1016/0167-6105(95)00033-X).
- [30] Barthelmie RJ, Folkerts L, Larsen GC, Rados K, Pryor SC, Frandsen ST, et al. Comparison of wake model simulations with offshore wind turbine wake profiles measured by sodar. *Journal of Atmospheric and Oceanic Technology* 2006;23:888–901. <https://doi.org/10.1175/JTECH1886.1>.
- [31] Göçmen T, Laan P van der, Réthoré P-E, Diaz AP, Larsen GChr, Ott S. Wind turbine wake models developed at the technical university of Denmark: A review. *Renewable and Sustainable Energy Reviews* 2016;60:752–69. <https://doi.org/10.1016/j.rser.2016.01.113>.
- [32] Jensen NO. A note on wind generator interaction. Roskilde: Risø National Laboratory; 1983.
- [33] Katic I, Højstrup J, Jensen NO. A Simple Model for Cluster Efficiency: European Wind Energy Association Conference and Exhibition. EWEC'86 Proceedings Vol 1 1987:407–10.
- [34] Larsen GC. A simple wake calculation procedure. Risø National Laboratory; 1988.
- [35] Nielsen P, Villadsen J. WindPRO 2.7 User Guide 3rd Ed 2010.
- [36] Ott S, Berg J, Nielsen M. Linearised CFD Models for Wakes. Roskilde: Danmarks Tekniske Universitet, Risø Nationallaboratoriet for Bæredygtig Energi; 2011.
- [37] Orcina Ltd. OrcaFlex User Manual. Orcina 1987. <https://www.orcina.com/webhelp/OrcaFlex/> (accessed January 19, 2022).
- [38] Chung J, Hulbert GM. A Time Integration Algorithm for Structural Dynamics With Improved Numerical Dissipation: The Generalized- α Method. *Journal of Applied Mechanics* 1993;60:371–5. <https://doi.org/10.1115/1.2900803>.
- [39] NREL. AeroDyn 2002. <https://www.nrel.gov/wind/nwtc/aerodyn.html> (accessed July 8, 2022).
- [40] Ikhennicheu M, Lynch M, Doole S, Borisade F, Wendt F, Schwarzkopf MA, et al. Review of the state of the art of dynamic cable system design 2020.
- [41] Rentschler MUT, Adam F, Chainho P, Krügel K, Vicente PC. Parametric study of dynamic inter-array cable systems for floating offshore wind turbines. *Mar Syst Ocean Technol* 2020;15:16–25. <https://doi.org/10.1007/s40868-020-00071-7>.
- [42] Burnett DR, Beckman R, Davenport TM. Submarine Cables : The Handbook of Law and Policy. Leiden, UNITED STATES: BRILL; 2013.

- [43] Thies P, Johanning L, Smith G. Assessing mechanical loading regimes and fatigue life of marine power cables in marine energy applications. Special Issue Proc of the Institution of Mechanical Engineers, Part O, Journal of Risk and Reliability 2011;226:18–32. <https://doi.org/10.1177/1748006X11413533>.
- [44] Cable Manufacturers Worldwide | Subsea & Power Cables Manufacturer. JDR Cables, Providing the Vital Connection 2022. <https://www.jdrcables.com/> (accessed March 24, 2022).
- [45] Leonardo Energy. Copper and Aluminium: A Comparison of Life-Cycle Cost. Leonardo Energy - Knowledge Base 2022. <https://help.leonardo-energy.org/hc/en-us/articles/205305482-Copper-and-Aluminium-A-Comparison-of-Life-Cycle-Cost> (accessed July 7, 2022).
- [46] Why use copper rather than aluminium in power transformers? Leonardo Energy - Knowledge Base 2021. <https://help.leonardo-energy.org/hc/en-us/articles/206843645-Why-use-copper-rather-than-aluminium-in-power-transformers-> (accessed March 26, 2022).
- [47] Copper has high fatigue strength. Leonardo Energy - Knowledge Base 2021. <https://help.leonardo-energy.org/hc/en-us/articles/207900965-Copper-has-high-fatigue-strength> (accessed March 26, 2022).
- [48] Bai Q, Bai Y. 24 - Flexible Pipe. In: Bai Q, Bai Y, editors. Subsea Pipeline Design, Analysis, and Installation, Boston: Gulf Professional Publishing; 2014, p. 559–78. <https://doi.org/10.1016/B978-0-12-386888-6.00024-9>.
- [49] Equinor. Hywind Tampen PUD del II- Konsekvensutredning. Equinor ASA; 2019.
- [50] Eldøy S. Hywind Scotland Pilot Park Project Plan for Construction Activities 2017.
- [51] Rapha JI, Domínguez JL. Suspended cable model for layout optimisation purposes in floating offshore wind farms. J Phys: Conf Ser 2021;2018:012033. <https://doi.org/10.1088/1742-6596/2018/1/012033>.
- [52] Thies P, Harrold M, Johanning L, Grivas K, Georgallis G. Load and fatigue evaluation for 66kV floating offshore wind submarine dynamic power cable, Jicable; 2019.
- [53] Rentschler MUT, Adam F, Chainho P. Design optimization of dynamic inter-array cable systems for floating offshore wind turbines. Renewable and Sustainable Energy Reviews 2019;111:622–35. <https://doi.org/10.1016/j.rser.2019.05.024>.
- [54] Schnepf A, Johnsen Ø, Pavon CL, Devulder A, Ong MC. Suspended Power Cable Configurations for Floating Offshore Wind Turbines in Deep Water Powering an FPSO. Offshore and Arctic Engineering 2022.
- [55] Vos Prodict Innovations. Subsea Cable Bend Stiffener | By Vos Prodict Innovations. Vos Prodict 1950. <https://www.vos-prodict.com/products/cable-bend-stiffener/> (accessed June 27, 2022).
- [56] DeepWater Buoyancy. Umbilical Buoyancy. DeepWater Buoyancy 2022. <https://deepwaterbuoyancy.com/product/umbilical-buoyancy/> (accessed June 27, 2022).
- [57] DNV. DNV-RP-C205: Environmental conditions and environmental loads 2019.
- [58] Barltrop NDP, Centre for Marine and Petroleum Technology. Floating Structures: A Guide for Design and Analysis. CMPT; 1998.
- [59] Faltinsen O. Sea Loads on Ships and Offshore Structures. Cambridge University Press; 1993.
- [60] Hasselmann K, Barnett T, Bouws E, Carlson H, Cartwright D, Enke K, et al. Measurements of wind-wave growth and swell decay during the Joint North Sea Wave Project (JONSWAP). Deut Hydrogr Z 1973;8:1–95.
- [61] Norwegian Petroleum Directorate. Regulations relating to loadbearing structures in the petroleum activities. 1995.
- [62] Sarpkaya T “Sarp,” editor. Waves and Wave–Structure Interactions. Wave Forces on Offshore Structures, Cambridge: Cambridge University Press; 2010, p. 109–71. <https://doi.org/10.1017/CBO9781139195898.005>.

- [63] Ameryoun H, Schoefs F. Probabilistic Modeling of Roughness Effects Caused by Bio-Colonization on Hydrodynamic Coefficients: A Sensitivity Study for Jacket-Platforms in Gulf of Guinea. vol. 1. 2013. <https://doi.org/10.1115/OMAE2013-11101>.
- [64] Spraul C, Arnal V, Cartraud P, Berhault C. Parameter Calibration in Dynamic Simulations of Power Cables in Shallow Water to Improve Fatigue Damage Estimation. Volume 3A: Structures, Safety and Reliability, Trondheim, Norway: American Society of Mechanical Engineers; 2017, p. V03AT02A037. <https://doi.org/10.1115/OMAE2017-61821>.
- [65] Decurey B, Schoefs F, Barillé A-L, Soulard T. Model of Bio-Colonisation on Mooring Lines: Updating Strategy Based on a Static Qualifying Sea State for Floating Wind Turbines. *Journal of Marine Science and Engineering* 2020;8:108. <https://doi.org/10.3390/jmse8020108>.
- [66] DNV. DNV-ST-0437: Loads and site conditions for wind turbines 2016.
- [67] DNV. DNV-RP-F105: Free spanning pipelines 2017.
- [68] NORSOK. NORSOK N-003 2017.
- [69] Jonkman J, Musial W. Offshore Code Comparison Collaboration (OC3) for IEA Wind Task 23 Offshore Wind Technology and Deployment. National Renewable Energy Lab. (NREL), Golden, CO (United States); 2010. <https://doi.org/10.2172/1004009>.
- [70] Kvitrud A, Løland AH. Observed Wave Actions on Norwegian Semi-Submersible and TLP Decks. Volume 1: Offshore Technology, Madrid, Spain: American Society of Mechanical Engineers; 2018, p. V001T01A023. <https://doi.org/10.1115/OMAE2018-77008>.
- [71] El Beshbichi O, Xing Y, Ong M. An object-oriented method for fully coupled analysis of floating offshore wind turbines through mapping of aerodynamic coefficients. *Marine Structures* 2021;78:102979. <https://doi.org/10.1016/j.marstruc.2021.102979>.
- [72] Ross A, McKinnon G. Wind Turbine Validation Report - Orcina Project 1405. 2018.
- [73] Morison's equation 1950. <https://www.orcina.com/webhelp/OrcaFlex/Content/html/Morison%27sequation.htm> (accessed January 20, 2022).
- [74] OrcaFlex K01 5MW spar FOWT example file - Simulation files & guidance documents. Orcina 1986. <https://www.orcina.com/resources/examples/> (accessed January 19, 2022).
- [75] Grivas K, Moraiti A, Georgallis G, Rinaldi G, Thies PR, Johanning L. Dynamic HV cables with AL conductors for floating offshore wind turbines: A cost and behavior comparative study. *Developments in Renewable Energies Offshore*, CRC Press; 2020.
- [76] Subsea Buoy MSB 234/4 – PartnerPlast 1992. <https://partnerplast.com/products/buoyancy/modular-buoys/msb-234-4/> (accessed May 26, 2022).
- [77] Sumer BM, Fredsøe J. *Hydrodynamics Around Cylindrical Structures*. World Scientific Publishing; 2006.

Appendix A

Python code for marine growth model conversion

```
# Original Author IzwanAhmad
# Convert the dat file of a clean cable to marine growth according to NORSOK-N-OO3 (2017)
# Identify line type by defining the target segment length in OrcaFlex
# MG properties (drag, weight, added mass, diameter, etc) must be precalculated and defined in the original dat
file
# This code only assign each segment (element) along the cable to the precalculated MG properties depending on
Z
```

```
import OrcFxAPI as OF
import pandas as pd
import numpy as np
import os
import glob
```

```
my_path = os.getcwd()
file_list = glob.glob('*.dat')
exclude_list = glob.glob('EOL*')
```

```
for files in file_list:
```

```
if files not in exclude_list:
```

```
    model      = OF.Model()          # Create a model object (basically a template)
    model_file = files              # Load the .dat file into the model object
    model.LoadData(model_file)
    model.Reset()                  # Make sure that the model is in a reset state
    model.CalculateStatics()       # calculate the statics
    cableOF    = model['PowerCable'] # Name of cable line element in OrcaFlex
    cableZ     = cableOF.RangeGraph('Z') # Extract water depth data
    Z         = cableZ.Mean.tolist()  # Mean gives the static values (m)
    Arc       = cableZ.X.tolist()    # X return the CL of each segment to list in "Arc"
    model.Reset()                  # Reset the model
```

```
df = pd.DataFrame(np.column_stack([Arc, Z]), columns=['CumulativeLength', 'Depth'])
df['LineType'] = ""
df['TargetSegmentLength'] = ""
```

```
for i in range(len(df['CumulativeLength'])):
```

```
    if df['CumulativeLength'][i] != 0:
```

```
        df['TargetSegmentLength'][i] = round(df['CumulativeLength'][i]-df['CumulativeLength'][i-1],7)
```

```
##### Marine Growth Conversion Start #####
```

```
for i in range(len(df['Depth'])):
```

```
    if df['TargetSegmentLength'][i] == 0.3: # Assumes cable hangoff point always at -70m
```

```
        df['LineType'][i] = 'InterarrayCable_EOL2'
```

```
    elif df['TargetSegmentLength'][i] == 0.12: # No MG around the BendStiffener
```

```
        df['LineType'][i] = 'InterarrayCable_SOL'
```

```
    elif df['TargetSegmentLength'][i] == 0.31: # Subsea Buoy with Anti MG coating
```

```
        df['LineType'][i] = 'SubseaBuoy_SOL'
```

```
    else: # Change Interarray Cable LineType (diameter, weight,
```

```
drag)
```

```
        if df['Depth'][i] >= -50:
```

```
            df['LineType'][i] = 'InterarrayCable_EOL3'
```

```
        elif -60 <= df['Depth'][i] <= -50:
```

```
            df['LineType'][i] = 'InterarrayCable_EOL1'
```

```
        elif -100 <= df['Depth'][i] <= -60:
```

```
            df['LineType'][i] = 'InterarrayCable_EOL2'
```

```
        else:
```

```
            df['LineType'][i] = 'InterarrayCable_SOL'
```

```

df["TargetSegmentLength"][0] = 0
df["LineType"][0] = 'InterarrayCable_EOL2'
df1 = df[["CumulativeLength", 'LineType', 'TargetSegmentLength']]
##### Marine Growth Conversion End #####

# Shrink DF
df1["SectionLength"] = ""
df1["SectionLength"][0]=df1["TargetSegmentLength"][0]

for i in range(1,len(df1)):
    if (df1["LineType"][i] is df1["LineType"][i-1]) and (round(df1["TargetSegmentLength"][i],7) ==
round(df1["TargetSegmentLength"][i-1],7)):
        df1["SectionLength"][i] = df1["SectionLength"][i-1]+ df1["TargetSegmentLength"][i]
    else:
        df1["SectionLength"][i] = df1["TargetSegmentLength"][i]

# 1. Remove row or similar LineType
df2 = df1[df1["LineType"].ne(df1["LineType"].shift(-1))]

# 2. Remove row or similar SectionLength
df3 = df1
df3 = df3[df3["LineType"].ne(df3["LineType"].drop_duplicates()) &
df3["TargetSegmentLength"].ne(df3["TargetSegmentLength"].shift(-1))]

# 3. Combine df2 and df3 that satisfy removal criteria #1 and #2
df4 = pd.concat([df2,df3]).drop_duplicates(subset=['CumulativeLength']).reset_index(drop=True).sort_values(by='CumulativeLength')
df4 = df4.reset_index()

# 4. Feed the compressed dataframe to OF
cableOF.NumberOfSections = df4.shape[0]
for i in range(df4.shape[0]):
    cableOF.LineType[i] = df4.loc[i, 'LineType']
    cableOF.TargetSegmentLength[i] = df4.loc[i, 'TargetSegmentLength']
    cableOF.Length[i] = df4.loc[i, 'SectionLength']

model.SaveData('EOL_'+model_file) # Save the file

```

Appendix B

Python code for multiple case generation based on cable configuration variable

```
# Batch processing in OrcaFlex running from Python
# Using the multiprocessing toolbox (install: pip install multiprocessing)
# Need to have the OrcFxAPI installed with OrcaFlex (see manual)
# Optimizes a suspended power cable layout parametrically
# using multiprocessing and OrcaFlex 11.2
# Original Author AnjaSchnepf
# Modified by IzwanAhmad

# - Setup the entire dat file and add the data missing below after 'main'
# - Implement the post-calculation actions in the OrcaFlex model
# - only for statics

import OrcFxAPI as OF
import subprocess
import os
import glob
import pandas as pd
from sys import exit

# Get path of current directory
my_path = os.path.dirname(__file__)

def batchRun(fileNames):

    # This function calls OrcaFlex to process data files via batch form.
    # An OrcaFlex window will open. If the batch is not successful, then it
    # will _not_ close automatically, you have to 'ok' the list of failed cases.
    # Check out https://www.orcina.com/webhelp/OrcaFlex/Redirector.htm?RunningOrcaFlex.htm
    # for the batch process with OrcaFlex and further commands
    # # :param fileNames:
    # - Full path to a txt file that contains all the data file names
    # (preferred option by Orcina to not run into the command line arguments error)

    if type(fileNames) is str:
        # This runs the OrcaFlex data files listed in a txt file
        # fileNames is the path of the txt file listing the cases to be run
        batchProcess = subprocess.run([
            r"C:\Program Files (x86)\Orcina\OrcaFlex\11.2\OrcaFlex64.exe", # !!! check your path to OrcaFlex
            '/batch',
            '/closeAfterBatch',
            '/FileList',
            fileNames
        ])

    return batchProcess

if __name__ == '__main__': #default syntax

##### Input Start #####
FOWTspacing      = 126*9          # 9D spacing
SparRad          = 10.4/2        # hangoff point from vertical center of spar
Lengths          = [1200,1400]  # Parameters for the study
lengths_step     = 20           # make 0 if not to consider range
```

```

BuoyDistances      = [200,400]                # must be greater than L_buoySection
dist_step          = 20                       # make 0 if not to consider range
BuoyCounts         = [2,3,4,5]
BaseFileName       = 'AL_00deg_MG.dat'        # Basic model definitions
CableName          = 'PowerCable'            # Cable name in base OF model
hangoff_distance   = FOWTspacing-2*SparRad    # (m)
y_start            = SparRad                  # (m) where the cable starts on the y-axis
with_current       = True

# Attachments definition
Stiffener1         = 'BendStiffener_PA'
Stiffener2         = 'BendStiffener_PB'
SubseaBuoy        = ['SubseaBuoy_SOL']
##### Input End #####

model = OF.Model()                                # Open OF model
                                                # Create a model object (basically a template)
model_file = os.path.join(my_path,BaseFileName)   # Load the base .dat file into the model object
model.LoadData(model_file)
model.Reset()                                     # Make sure that the model is in a reset state, this removes all simulation cache

# Define overall parameters in OF model
if with_current:
    model.environment.CurrentRamped = 'No'        # Switch on current for steady-state
else:
    model.environment.CurrentRamped = 'Yes'        # static position to be calculated without the effects of
current by scaling it by the ramp factor
    model.general.DynamicsEnabled = 'No'
    model.general.StaticsEnabled = 'Yes'
    model.general.PostCalculationActionSkipSimulationFileSave = 'Yes'

cableOF            = model[CableName]            # Get cable name in the model
cabelOFLinetype   = model[cableOF.LineType[0]]

# Prepare some parameters
if lengths_step != 0 :
    lengths_range   = range(Lengths[0],Lengths[-1]+lengths_step,lengths_step)
else :
    lengths_range   = Lengths
if dist_step != 0 :
    buoydist_range  = range(BuoysDistances[0],BuoysDistances[-1]+dist_step,dist_step)
else:
    buoydist_range  = BuoysDistances

# Loop over different parameters to create new dat-files
for length in lengths_range :
    name1 = BaseFileName[:-4] + '_L' + str(length) + 'm'

# Test
if length < hangoff_distance:
    print('Error: Input cable length is shorter than turbine distance')
    exit()

for buoycount in BuoyCounts :
    name2 = name1 + '_' + str(buoycount) + 'buoy'    # Case name
    for buoydist in buoydist_range :
        name3 = name2 + '_S' + str(buoydist) + 'm'    # Case name

        if os.path.exists(name3+'_stead.csv'):
            break

```



```

if os.path.exists(name3+'.dat'):
    break

# Create new dat-file
# Segment lengths
discr_free      = 1      # (m) define standard segment length here *change to discr_Rest
L_start        = 15     # (m) define hang off section length of the cable
discr_start     = 0.3   # (m) discretization of the cable at the hang-offs
L_buoy         = 2.94   # (m) length of the subsea buoy
discr_buoy     = 0.21   # (m) target segment length must be multiplication of buoy length
L_stiffener    = 2.88
discr_stiffener = 0.12  # (m) target segment length must be multiplication of stiffener length
N_stiffenerDiscr = 30   # excess number segment length upon cable exit at stiffener

# Define the different lengths of the cable segments
L_buoySection = L_buoy+(2*L_stiffener)+(N_stiffenerDiscr*discr_stiffener) # (m) assumed overall
length for the buoyant sections
L_midSection  = length-(2*L_start)
RestLength    = (L_midSection - L_buoySection - buoysdist*(buoyscount-1)) / 2

if RestLength < 0:
    print('Length between buoys in sum larger than cable length')
    break
elif RestLength < discr_free :
    discr_free = min(round(RestLength / 3, 1), round(buoysdist-L_buoySection) / 3, 1)

divisions = int(4*buoyscount + 1) # division of middle part

# Discretize cable in OF
#1 free part
cableOF.NumberOfSections      = 2+divisions
cableOF.Length[1]             = RestLength
cableOF.TargetSegmentLength[1] = discr_free
cableOF.Length[divisions]     = RestLength
cableOF.TargetSegmentLength[divisions] = discr_free

#2 hang-off sections
cableOF.Length[0]             = L_start      # length at hang-off 1
cableOF.TargetSegmentLength[0] = discr_start # discretization at hang-off 1
cableOF.Length[divisions+1]   = L_start     # length at at hang-off 2
cableOF.TargetSegmentLength[divisions+1] = discr_start # discretization at at hang-off 2

#3 part with buoys attached
for midSect in range(2,divisions,4):
    cableOF.Length[midSect]             = (L_buoySection-L_buoy)/2
    cableOF.TargetSegmentLength[midSect] = discr_stiffener
    cableOF.Length[midSect+1]           = L_buoy
    cableOF.LineType[midSect+1]         = SubseaBuoy[0]
    cableOF.TargetSegmentLength[midSect+1] = discr_buoy

# if an error occurs here, check if all data in the OF file is changeable in the segmentation
cableOF.Length[midSect+2]             = (L_buoySection-L_buoy)/2
cableOF.TargetSegmentLength[midSect+2] = discr_stiffener
if not midSect+3 == divisions:
    cableOF.Length[midSect+3]         = buoysdist-L_buoySection
    cableOF.TargetSegmentLength[midSect+3] = discr_free

#4 Stiffeners positions and give to OF
numOfAttachments      = buoyscount*2
cableOF.NumberOfAttachments = numOfAttachments

```

```

Lc = round(L_start + RestLength + (L_buoySection/2),5) # Length counter

for i in range(0,buoyscount*2,2): # Give stiffeners to OF

    cableOF.AttachmentType[i]          = Stiffener1
    cableOF.AttachmentType[i+1]        = Stiffener2
    cableOF.AttachmentzRelativeTo[i]    = 'End A'
    cableOF.AttachmentzRelativeTo[i+1]  = 'End A'
    cableOF.Attachmentz[i]              = Lc - (L_buoy/2)
    cableOF.Attachmentz[i+1]            = Lc + (L_buoy/2)
    Lc                                   = round(Lc+buoysdist,5) # update for next round

# Create a filename for this specific case, save file, attach to DataFrame
filename      = name3 + '.dat'
filename_case = os.path.join(my_path,filename)
model.SaveData(filename_case) # Save the file

##### Batch run files in OF #####
# Names of the OrcaFlex .dat-files (glob: all files on the current path)
dataFileNames = glob.glob('*.*dat') # collect all .dat file and save as list
dataFileNames.remove(BaseFileName)

# Prepare the txt file
txtFileName = 'OrcaFlex_dat_files_list.txt' # create .txt file
txtFilePath = os.path.join(my_path, txtFileName) # assign full path to the .txt file (put location in same folder)

# Write a txt file with all the data file names in it
with open(txtFilePath, 'w') as txtfile: # 'w' is to write
    for item in dataFileNames:
        txtfile.write("%s\n" % item) # "%s" insert item in the list, "\n" is to create new line after insert 1 list, can
be the relative path if same place as txt file
txtfile.close()

# Calculate the batch based on the listed file names in the .txt file
run = batchRun(txtFilePath)

# Delete txt file
os.remove(txtFilePath)

# Compile Static Result
path = os.path.dirname(__file__)

```